Exploring the limits of the Island of Inversion with the Level Mixing and Nuclear Magnetic Resonance techniques.

Stephanie Teughels

november 2001

Contents

Introduction

Close to the β stability line in the nuclear chart, the shell structure can be understood well in terms of a harmonic oscillator potential with a spin-orbit splitting. When studies on exotic nuclei far from the stability line became possible owing to the development of radioactive nuclear beams, several indications for the "collapse of the shell model" appeared. Light, neutron rich nuclei with Z=10-12 and $N \approx 20$ form a region of deformation corresponding to the disappearance of the N=20 shell closure and form the so called "Island of Inversion". Measurements of the masses, of the life times and level densities, and of the static and dynamic moments of the sodium and magnesium isotopes, all pointed out that the ground states of these nuclei are considerably deformed. Different theoretical approaches were undertaken. Due to the large neutron excess, the proton-neutron interaction causes an inversion of the filling of the orbitals. It induces 2 particle - 2 hole excitations of the neutrons from the sd shell into the fp shell, leading to an energetically more favored intruder state.

Although the first indication was obtained in 1975 with the mass measurements of ^{31,32}Na by C.Thibault *et al.*, the region of deformation is still not completely understood. Especially the limits of the region are not established neither by theory nor by experiments. In chapter 1 an overview will be given on the experimental and theoretical studies performed in this region.

The purpose of this work is the measurement of the spin of ^{31}Mg, of the magnetic moments of ^{31}Al and ^{31,29}Mg and of the quadrupole moments of ^{31,29}Mg. All the isotopes are situated at the limits of the region of deformation. The spin and magnetic moment are good probes for the single particle structure of the nu-

clei. It reveals information about the orbitals occupied by the valence nucleons. Quadrupole moments are sensitive to the collective nature of the nucleus. They provide information on the deformation of the isotopes. Therefore, data on the magnetic and quadrupole moment of nuclei situated at the edges of the island are extremely valuable to learn about the structure of the intruder nuclei.

This static moments were measured using the Level Mixing Resonance (LMR) method and Nuclear Magnetic Resonance (NMR) method for β-decaying nuclei. The LMR technique yields the spin and the ratio of the quadrupole moment to the magnetic moment with a very high accuracy since it is a resonant method. When performed at a recoil fragment separator, it also provides the magnetic moment separately. Even though the value for the magnetic moment is obtained with a rather poor accuracy, it reveals at least information of the sign of the dipole moment. The LMR method at a recoil separator will be illustrated in chapter 2 together with the results on ^{31}Mg and ^{29}Mg.

The NMR technique, a well established method, will briefly be elucidated in chapter 3 with the results on a test experiment on ^{27}Na and on the magnetic moment of ^{31}Al and ^{31}Mg.

The new results on the spin and the static moments will be discussed in chapter 4.

Chapter 1

Physics motivation

The so called "Island of Inversion" is the region of the nuclear chart where Z=10-12 and N$\sim$ 20, figure 1.1. These nuclei exhibit typical characteristics of deformed nuclei. It can be understood as the disappearance of the N=20 shell closure. The ordering of the configurations are different from the one dictated by the single particle energies near stability. Configurations that are highly excited near stability may become degenerate with, or even appear at a lower energy than the standard ones, provoking structural changes in the ground and low-lying states of the nucleus. In opposition to the standard configurations these are called intruder configurations.

As will be shown in this chapter it is not clear neither from experimental nor from theoretical point of view where the limits of the region are situated.

In section 1.3 more attention will be paid to the spectroscopic information of ^{31}Mg, since this will be of major importance in the following chapters.

1.1 Mass measurements.

The collapse of the N=20 shell closure was originally deduced from the much stronger than expected binding energies of the ^{31}Na and ^{32}Na sodium nuclei. The masses were measured via direct on-line mass spectrometry after production

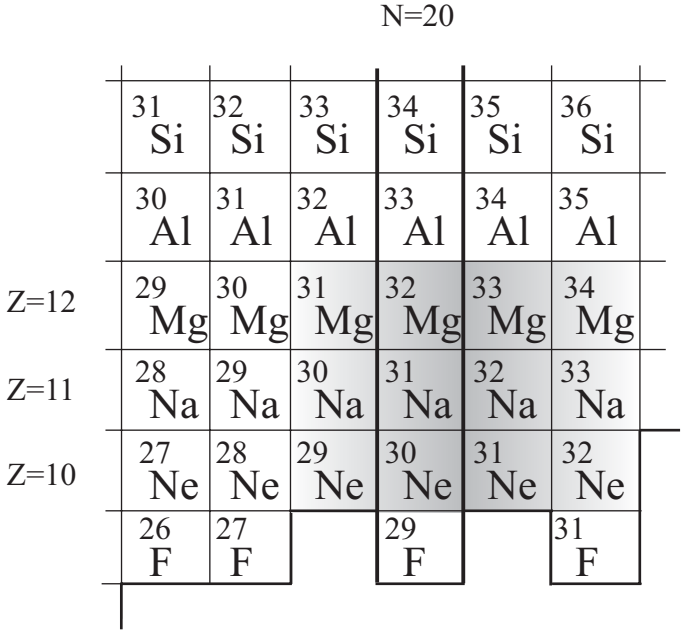

Figure 1.1: *The nuclear chart in the region of the Island of Inversion Z=10-12, N*$\sim$ 20.

of the isotopes in an ion-source at CERN by C.Thibault *et al.* [1] (table 1.1). These measurements have been repeated several times to improve the precision and to investigate the masses of nuclei further from stability, via direct time of flight (TOF) mass measurements, table 1.1. The nuclei were produced by target or projectile fragmentation coupled with a recoil spectrometer by D.J.Vieira *et al.* (TOFI spectrometer at Los Alamos) [2], by A.Gillibert *et al.* (SPEG spectrometer at GANIL) [3], by X.G.Zhou *et al.* (TOFI) [4] and by N.A.Orr et al. (SPEG) [5]. From the experimental mass excess $\Delta = (M - A.M_u)c^2$, the separation energy of the two last neutrons S_{2n}, thereby avoiding the odd-even neutron pairing, can be deduced in terms of binding energy:

$$S_{2n} = M(A-2,Z) + M(2n) - M(A,Z) \quad (1.1)$$

$$= BE(A,Z) - BE(A-2,Z) \quad (1.2)$$

One of the most obvious indications for the existence of a shell structure is obtained by the study of the variation of the neutron separation energy S_{2n} with

increasing atomic number A. A sharp drop instead of a smooth decrease is associated with the crossing of a magic number, and corresponds to the onset of the filling of a new neutron shell of lesser binding energy. The Ca isotopes show the typical behavior of the filling of shells, with the two shell closures at N=20 and 28 being evidenced by the corresponding sharp decrease of S_{2n}, and a slowly decreasing S_{2n} as the $1f_{7/2}$ shell is filled, figure 1.2.

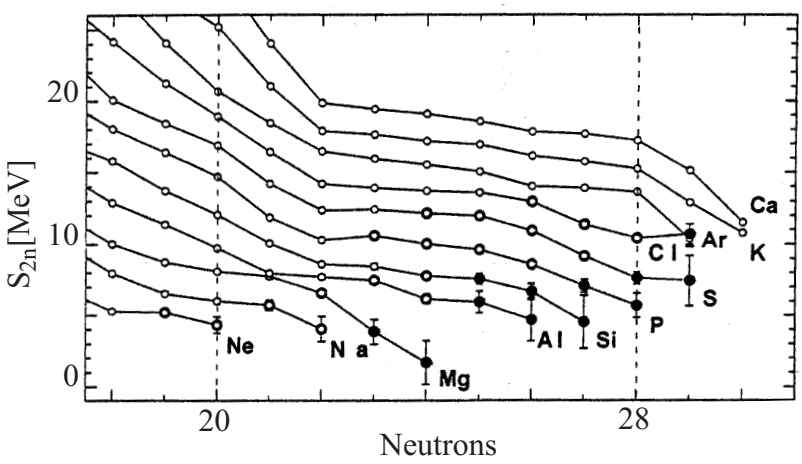

Figure 1.2: *Experimental S_{2n} values in the region of the N=20 and 28 shell closures obtained via direct mass measurements, [6].*

However, the decrease of S_{2n} levels off and even turns upwards for the sodium and magnesium isotopes with $20 \leq N \leq 22$. This reflects that a new structure of stronger binding energy than extrapolated from less exotic nuclei has become available and it is associated with the occurrence of deformation.
The variation of the neutron binding energy has no relation to the spatial properties of the nucleus, and the magnitude of the effect is not directly connected with the magnitude of an eventual shape transition.

In figure 1.3 a comparison is made between the measured binding energies with shell model calculations in the sd space using the WBMB interaction [7]. In the $(d_{5/2},s_{1/2},d_{3/2})$ space, the WBMB interaction consists only of the USD interaction of Wildenthal [9]. This interaction is obtained by fitting the experimental bind-

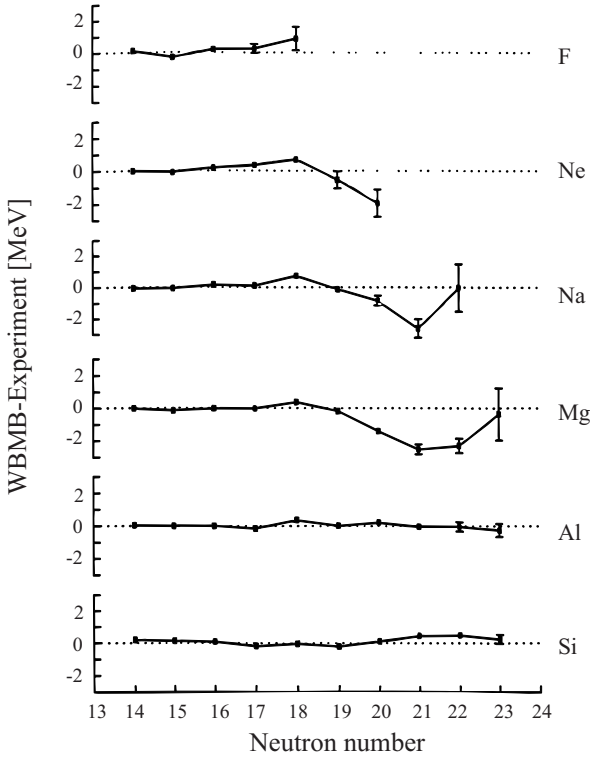

Figure 1.3: *Comparison between the measured binding energies [5] and WBMB calculations which employed the complete* $0\hbar\omega$ *basis [7].*

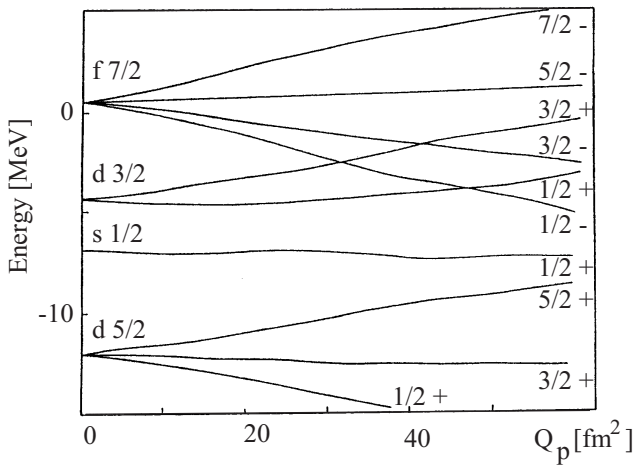

Figure 1.4: *Prolate part of the deformed HF single particle spectrum of* ^{31}Na *[8].*

ing energies and low lying excited states of sd-nuclei close to stability using the single particle energies and the two-body matrix elements as fit parameters. Excellent agreement between experiment and calculations is found for all the silicon and aluminum isotopes and for the magnesium, sodium and neon isotopes up to N=18 or 19. The overbinding of the neutron richer Mg, Na and Ne isotopes can be attributed to a transformation from a spherical shape to a prolate deformation driven by particle-hole excitations across the sd-fp shell gap. This was first proposed by Campi *et al.* [8] showing a much better agreement for the binding energy of ^{31,32}Na with Hartree-Fock (HF) calculations in the deformed Nilsson space. For large prolate deformations the $1/2^-$ and $3/2^-$ levels from the $1f_{7/2}$ orbital cross the $1/2^+$ and the $3/2^+$ levels of the $1d_{3/2}$ orbital, figure 1.4. Later on shell model calculations with different interactions have been performed in an enlarged sd-fp space allowing 2 neutrons to cross the shell gap [10, 11]. Using the WBMB interaction and introducing the weak-coupling approximation and truncation schemes in cases where full basis calculations were unfeasible, the binding energies were calculated with one, two and three neutrons promoted from the sd to the fp shell orbitals, referred to as 1,2 and $3\hbar\omega$ states [7]. These calculations indicate that for the Z=10-12, N=20-22 nuclei the lowest $2\hbar\omega$ state is more bound than the lowest $0\hbar\omega$. The discrepancies between experiment and theory (which does not take mixing into account) are reduced but not entirely eliminated and is probably caused by the repulsion between the 0 and $2\hbar\omega$ ground states. For N=19,21 and 23 the lowest $1\hbar\omega$ is in close competition with $2\hbar\omega$ for the lowest binding energy.

As can be seen in table 1.1, the masses obtained for ^{31,32}Mg by C.Détraz *et al.* [12] show an appreciable difference with the TOF measurements. In this experiment, ^{31}Na and ^{32}Na were produced in an ion-source. From the measured end-point energy of the β-decay of ^{31}Mg and ^{32}Na, and with the known masses of ^{31}Al and ^{32}Na respectively, the masses of ^{31}Mg and ^{32}Mg were deduced. The reference mass of ^{32}Mg was the mass of ^{32}Na from the original measurement of Thibault, almost 2MeV more bound than found with TOF measurement [5]. Since the mass of ^{32}Mg is tied through a Q_β measurement to ^{32}Na, a large part of the mass

Table 1.1: Mass excesses Δ in MeV from direct time of flight measurements at a fragment separator (Ref. [5, 4, 3, 2]), from a direct mass measurement after an ion source (Ref. [1]) and from the Q_β measurement (Ref. [12]).

	Ref [5]	Ref [4]	Ref [3]	Ref [2]	Ref [12]
^{31}Mg	-3.22(0.14)	-3.14(0.11)	-3.28(0.17)	-3.56(0.20)	-5.0(0.7)
^{32}Mg	-0.86(0.20)	-0.76(0.12)	-0.83(0.25)	-0.75(0.24)	-1.9(1.5)
					Ref [1]
^{31}Na	12.63(0.31)	12.68(0.20)	12.52(0.93)		10.60(0.80)
^{32}Na	18.37(0.59)	18.5(1.0)			16.4(1.1)

deviation noted for ^{32}Mg can be attributed back to the ^{32}Na deviation. However, this reasoning can't be made for the measured mass of ^{31}Mg. There, the Q_β was determined by the measured end-point energies of the β in coincidence with the photopeaks associated with the β-feeding of the excited levels of ^{31}Al, figure 1.12. The extraction of the end-point β-energy from the experimental energy spectrum was accomplished by the method of shape fitting. It assumes that all β-energy spectra for allowed transitions are identical within an overall normalization of the number of counts and have a proportionality along the energy axis measured by a stretch factor α. Since this stretch factor varies linearly with the end-point energy, it provides a measurement of this energy, figure 1.5. The ^{31}Al reference mass is determined by direct mass measurements, [13, 14], and in perfect agreement with the β-decay end-point measurement [15].

To obtain the same result for the Q_β measurement (Δ=-5.0(0.7)MeV) as is obtained by the weighted average of the results obtained with the TOF method (Δ=-3.24(0.07)MeV), the end-point energy would have been 1.8(0.7)MeV larger than what was measured. From C.Détraz *et al.* [12] one can deduce that this would come down to a stretch factor $\alpha = 1.3$ or an increase of χ^2 with 240%, figure 1.5.

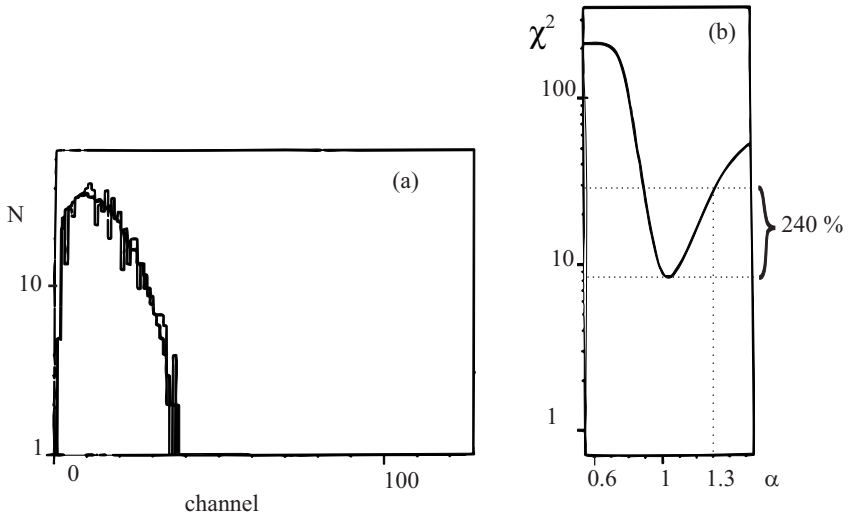

Figure 1.5: ^{31}Mg *β-spectrum coincident with the photopeaks associated with the second excited level of* ^{31}Al *from [12]. (a) Experimental spectrum and stretched reference spectrum (b)* χ^2 *analysis of the stretch factor* α*. When the results are put in accordance with the TOF mass measurements, one obtains* $\alpha = 1.3$*, marked with the dotted line.*

It is important to realize that if the ^{31}Mg, produced by projectile or target fragmentation, is populating an unknown isomeric state surviving long enough to pass through the spectrometer ($\sim 1\mu s$), the time of flight method is not capable to distinguish between the ground or isomeric state masses. Therefore, it is possible that the TOF measurements are mass measurements of a less bound isomeric state and the Q_β measurement determines the mass of the ground state. In that case, ^{31}Mg shows an even larger overbinding than expected from a normal filling of the neutron shells.

1.2 Spin, charge radii and moments of the sodium isotopes.

Atomic beam laser spectroscopy experiments on the neutron rich sodium isotopes $^{21-31}$Na have been performed at CERN by G.Huber *et al.* [16] and F.Touchard *et al.* [17]. A first part of the experiment consisted of determining the hyperfine transitions of the sodium isotopes by laser light in a weak magnetic field. At optical resonance, hyperfine optical pumping occurs and changes the population distribution between the magnetic substates $|m_F>$. When the atoms pass a strong magnetic field, the nuclear spin I is decoupled from the electron spin J. By means of magnetic deflection or focussing of the atoms with a specific electron-spin projection, the hyperfine transitions are determined. In a second part, the laser light was polarized and locked at the frequency of the hyperfine transition. The optically pumped *atoms* were exposed to a radio frequent field in order to mix the population of the different $|m_F>$ states and so to induce a magnetic resonance.

This method differs somewhat with the nuclear magnetic resonance method applied on *nuclei* used in this work where the g-factor of the nucleus is obtained. From a magnetic resonance on atoms, the spin of the nucleus can be determined, since the transition frequency for atoms in a magnetic field B is given by

$$\nu_{RF} = g_F \mu_B B/\hbar \tag{1.3}$$

$$g_F \approx \frac{F(F+1)+J(J+1)-I(I+1)}{2F(F+1)} g_J \tag{1.4}$$

where F and J are known, $g_J = 2$ and taking into account that the nuclear magnetism has a much smaller effect than the atomic magnetism. The obtained spins are given in table 1.2.

For prolate deformations the eleventh proton should occupy the $\Omega = 3/2[211]$ Nilsson orbit leading to the ground state spin $I = \Omega = 3/2$ for the odd isotopes, figure 1.6. In the spherical limit the unpaired proton occupies the $d_{5/2}$ shell model orbit and the ground state spin should be $I = 5/2$. From this can be concluded that a spin 5/2 is a strong indication of an almost spherical nucleus (^{25,27}Na) and

that spin 3/2 indicates prolate deformation for ^{21,23,29,31}Na.

If only sd orbits are taken into account, spin 2 for the even ^{30}Na can be explained assuming a filled 3/2[202] orbit and the unpaired neutron being in the 1/2[200] orbit.

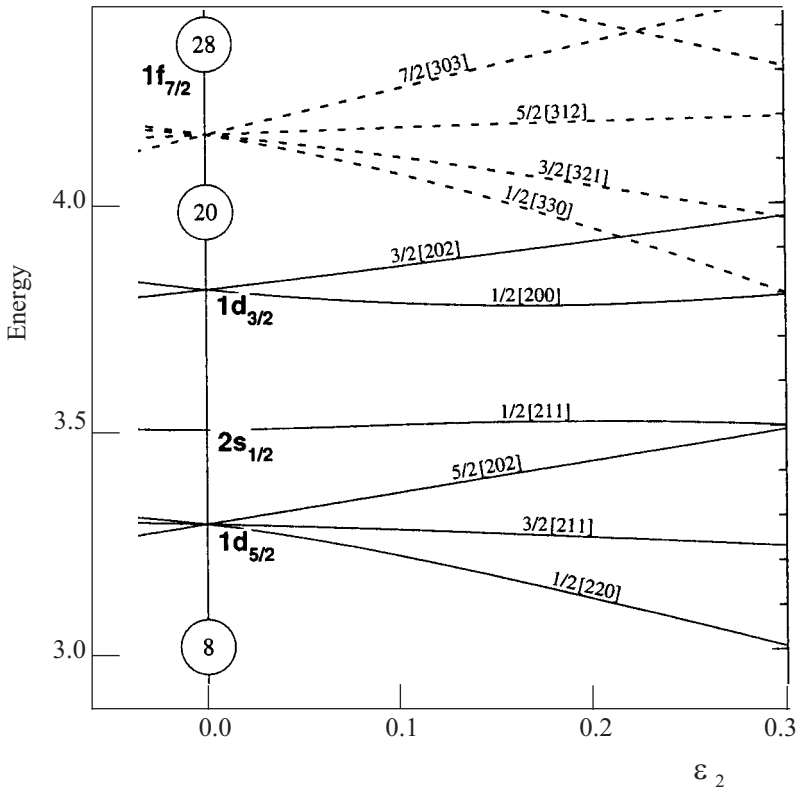

Figure 1.6: *Nilsson diagram for protons or neutrons (Z or N*$\leq$ 50 *as a function of the deformation parameter* $\varepsilon_2 \sim 0.95\beta$ *[94].*

From the hyperfine splitting, the magnetic and the electrostatic hyperfine constants are determined and the magnetic and the quadrupole moment of the sodium isotopes can be deduced. The obtained results can be found in table 1.2. The experimental magnetic moments are compared with USD results obtained with the free-nucleon M1 operator and with the effective operator [9] as well as compared with more recent MCSM calculations in the unrestricted sd-pf space [19]. The intruder's value is in better agreement with the experimental than the closed shell value for the $3/2^+$ state. Notice that the mixing between the intruder

Table 1.2: Spin and magnetic moments of the neutron rich sodium isotopes.

	Spin	μ_{exp} $[\mu_N]$	μ_{the} (sd-free) $[\mu_N]$	μ_{the} (sd-eff) $[\mu_N]$	μ_{the} (sd-pf free) $[\mu_N]$
^{29}Na	3/2	$2.449(8)^{[16]}$	$2.455^{[18]}$	$2.468^{[18]}$	
		$2.457(2)^{[18]}$			
^{30}Na	2	$2.083(10)^{[16]}$	$2.554^{[18]}$	$2.687^{[18]}$	
		$2.069(2)^{[18]}$			
^{31}Na	3/2	$2.283(38)^{[16]}$	$2.655^{[18]}$	$2.673^{[18]}$	$2.17^{[19]}$
		$2.298(2)^{[18]}$	$2.50^{[20]}$		

and the normal state will increase the value of μ moving it towards the experimental number.

By comparing the hyperfine transition frequencies of the different sodium isotopes, the isotope shift (IS) is obtained. The IS is the sum of the mass shift and the volume shift. When the mass A of the atom increases, the total kinetic energy of the atom increases and the electronic levels are shifted with $1/A^2$. When the amount of neutrons increases along an isotopic chain, the global nuclear charge density decreases. As a consequence the atomic levels narrow and the energy difference decreases. Although for the light elements (lighter than calcium), the volume shift is usually very small compared to the mass shift, the volume shift can not be neglected for the sodium isotopes. This volume shift can be divided into two parts: the normal volume effect and a deformation effect:

$$\delta\nu^{A,A'}_{volume} \sim \delta < r^2 >^{A,A'} \tag{1.5}$$

$$\delta < r^2 >^{A,A'} = < r^2 >^{A'} - < r^2 >^{A} \tag{1.6}$$

$$\delta < r^2 > = \delta_{sph} < r^2 > + \frac{5}{4\pi}\delta[< \beta^2 >< r^2 >_{sph}] \tag{1.7}$$

where $< r^2 >_{sph} \sim 3/5(r_0 A^{1/3})^2$ and $r_0 = 1.2fm$. When compared to the Hartree-Fock calculations [8], the mean square charge radii extracted from the isotope shift indicate prolate deformation for $^{28-31}$Na. No absolute deformation parameter

could be deduced since two stable isotopes are required to fix the mass shift unambiguously.

More precise measurements on the g-factor and quadrupole moments of $^{26-31}$Na have been performed by M.Keim *et al.* (CERN) [18, 21]. The isotopes produced in an ion source were reaccelerated, neutralized and polarized by optical pumping with a collinear laser beam. After implantation of the atoms in a cubic (non-cubic) lattice, the g-factor (quadrupole moment) was measured using the β-NMR (β-NQR) method. Results can be found in table 1.2 and figure 1.7.

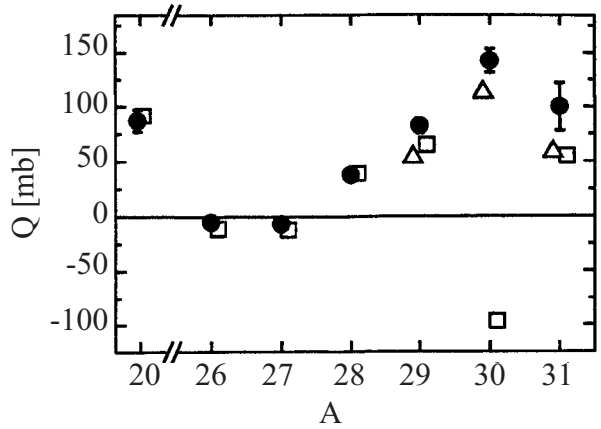

Figure 1.7: *Electric quadrupole moments of sodium isotopes. Experimental values (solid dots) are compared to calculations on a pure sd-shell model space (rectangles) and including fp-shell admixtures (triangles) [21].*

The calculation of the moments is based upon the wave functions obtained in the full sd model space $(1d_{5/2}, 1d_{3/2}, 2s_{1/2})$ with the USD Hamiltonian of Brown and Wildenthal [9]. Exclusion of core configurations (1s,1p) and of excitations to higher shells has to be accounted for by a renormalization of the operators. In the electric quadrupole operator this is done by introducing effective charges for the proton and the neutron. In this calculation effective charges $e_p = 1.35$ and $e_n = 0.35$ were used, common values for this mass region. The small quadrupole moments of $^{25-27}$Na are related to the main configuration of these isotopes: $(1d_{5/2})^3$ for protons and $(1d_{5/2})^6$, $(2s_{1/2})^{0-2}$ for neutrons. For this main

configuration, the neutrons have zero quadrupole moment because the valence neutrons outside the $1d_{5/2}$ closed shell are in the $2s_{1/2}$ state, and the protons have zero quadrupole moment because they are in the middle of a j shell. For the heavier isotopes, both protons and neutrons are in open shells, and the strong proton-neutron interaction gives rise to more collective states. Up to ^{28}Na the comparison with experiment and theory is good, but becomes significantly worse for ^{30}Na and ^{31}Na. This is an indication of the fp-intruder nature of these states and the basis has to be expanded to include the fp-shell intruder states.

The root mean square matter radii of $^{25-32}$Na were deduced from interaction cross sections of the sodium isotopes on a carbon target [22, 23, 24]. By combining these results with the mean square charge radii obtained from the isotope shift along the isotopic chain, a monotonic increase in the neutron skin thickness has been observed as the neutron number increases. Depending on different assumptions and corrections for quadrupole deformation, the thickness of the neutron skin of ^{32}Na varies from 0.2fm (almost the same as for the stable ^{23}Na) to 0.4fm. It is a unique situation where the nuclear charge radii and nuclear matter radii can be compared over a wide range of neutron numbers.

1.3 Lifetime, spin, parity and transition strengths of the magnesium and aluminum isotopes.

The spin and parity of the ground state of ^{29}Mg (N=17) $I^\pi = 3/2^+$ is fixed by the study of the β-decay of ^{29}Mg towards ^{29}Al, figure 1.9 [26]. The positions of the excited levels of this isotope, investigated via β-decay of ^{29}Na, showed a good agreement with USD calculations [27]. Two low lying levels (E_x=1095 and 1431keV), figure 1.8, have no measurable β feeding in the ^{29}Na decay but are strongly populated in the 1n channel of ^{30}Na [25]. They cannot be related to the sd-model states. Based on observed population intensities in multinucleon transfer reactions [13], a spin $I^\pi = 7/2^-$ is assumed for the 1431keV level, assigned to a $(s_{1/2})^2 f_{7/2}$ configuration. The $I^\pi = 3/2^-$ state resulting from the

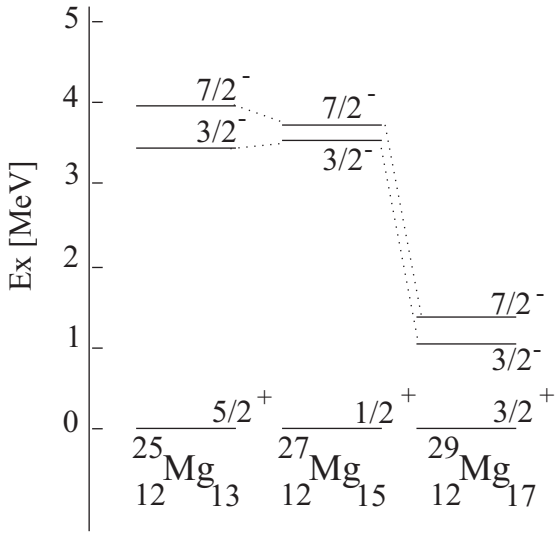

Figure 1.8: *The lowest experimental negative parity states for the odd mass* $^{25-29}$*Mg [25].*

$(s_{1/2})^2 p_{3/2}$ configuration would correspond to the 1095keV level [25]. This however necessitates the $p_{3/2}$ to be lower in energy than the $f_{7/2}$ orbit. A different possible explanation is a $3/2^-$ state corresponding to a coupling of a neutron to a deformed core of protons in a 2^+ state, as is proposed for ^{43}S [6].
The systematics of the lowest negative parity states of the odd mass $^{25-29}$Mg isotopes, figure 1.8, show a steep drop of the excitation energy for $N \geq 17$. This illustrates the importance of the $1f_{7/2}$ and $2p_{3/2}$ shells substantially below the region of strong deformation.

In the region of N=19,20 for the sodium and magnesium isotopes, β-decay studies have been performed by C.Détraz *et al.* [28], by D.Guillemaud-Muëller et al. [26] and by G.Klotz *et al.* [29]. In all the β-decay experiments, the magnesium isotopes were studied from the radioactive decay of the sodium isotopes. Since G.Klotz *et al.* gives the most extensive β-decay study, only this reference will be discussed. Moreover, the earlier measurements are in agreement with it.
The ^{31}Na, ^{32}Na isotopes were produced by bombarding an uranium carbide target by 600MeV protons, ionized and mass separated at CERN. Magnesium and alu-

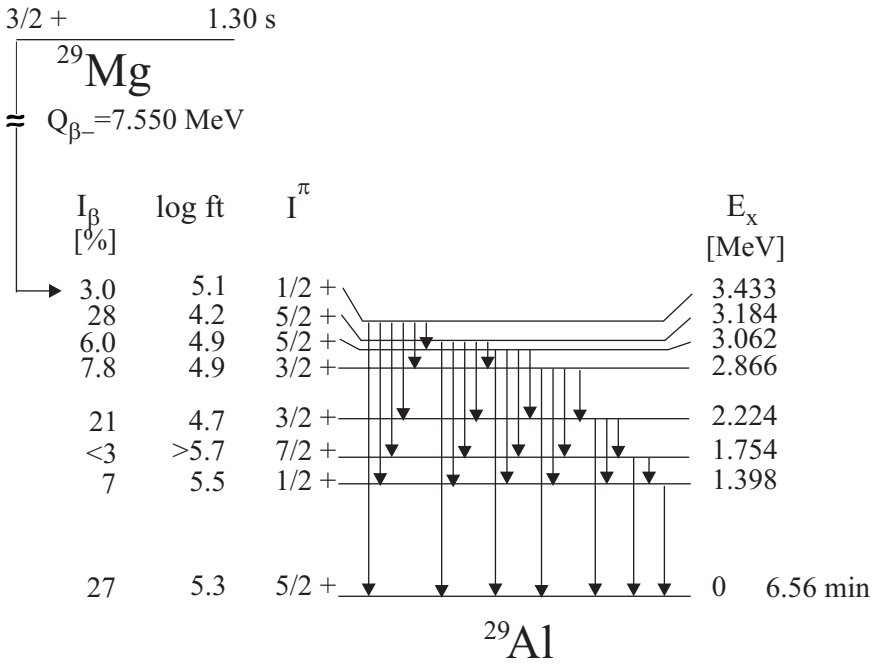

Figure 1.9: *Desintegration scheme of* ^{29}*Mg [94].*

minum isotopes resulted either from radioactive decay or direct production from the source. The relative amount of directly produced and ionized Mg and Al isotopes is not specified in the paper. As surface ionization mainly ionizes sodium atoms due to the lower ionization energy, the Na isotopes are more abundant compared to the Mg isotopes. Using a thin plastic scintillator for β detection, two germanium γ-detectors and a liquid scintillator for neutron detection, $\beta-\gamma$, $\beta-\gamma-\gamma$ and $\beta-\gamma-n$ measurements were possible. A small BaF_2 counter was used to measure the lifetime of low-energy transitions (up to 250keV). From the observed energy and intensity of the γ rays in the β decay and in the β delayed neutron emission, the disintegration scheme of ^{31}Na, ^{32}Na and ^{31}Mg was deduced, figure 1.10, 1.11 and 1.12.

The Q_β, S_{1n} and S_{2n} values are computed from the mass excess of ^{32,31}Na and ^{32,31}Mg obtained by the TOF method.

The half life of ^{31}Mg $t_{1/2} = 250(30)ms$ [28], is determined by the time dependence of the γ lines from the disintegration of the first and second excited level of

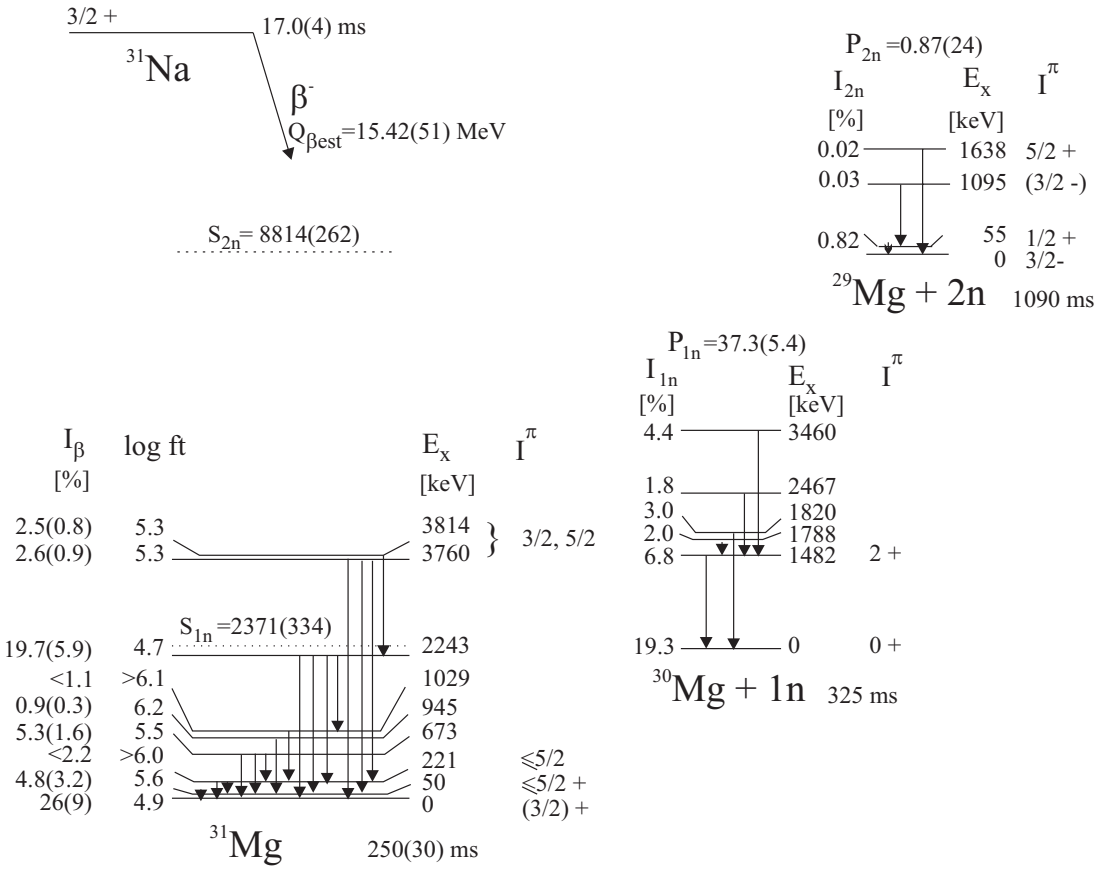

Figure 1.10: *Disintegration scheme of* ^{31}*Na [29].*

^{31}Al, figure 1.12. The obtained value is similar to the value found from the time dependence of the β-delayed neutrons $t_{1/2} = 230(20)ms$, once again after production of ^{31}Na [30].

In the ^{31}Mg $\rightarrow$ ^{31}Al β-decay, the observed allowed character of the transition towards the ground and second excited state of ^{31}Al gives a strong support to a limitation $I^\pi = (3/2, 5/2)^+$ of the spin and parity values of the ^{31}Mg ground state. The $5/2^+$ assignment is ruled out by the logf$_1$t=8.4 of the transition towards the first excited state if $I^\pi = 1/2^+$ is assumed for the 947keV state. The ^{31}Na $(I^\pi = 3/2^+) \rightarrow$ ^{31}Mg allowed transition to the ground state introduces similarly a limitation for the spin value of this state, $I = (1/2, 3/2, 5/2)$, the values $1/2$ and $5/2$ being rejected above. In the decay of ^{31}Na, the lifetime of low-energy

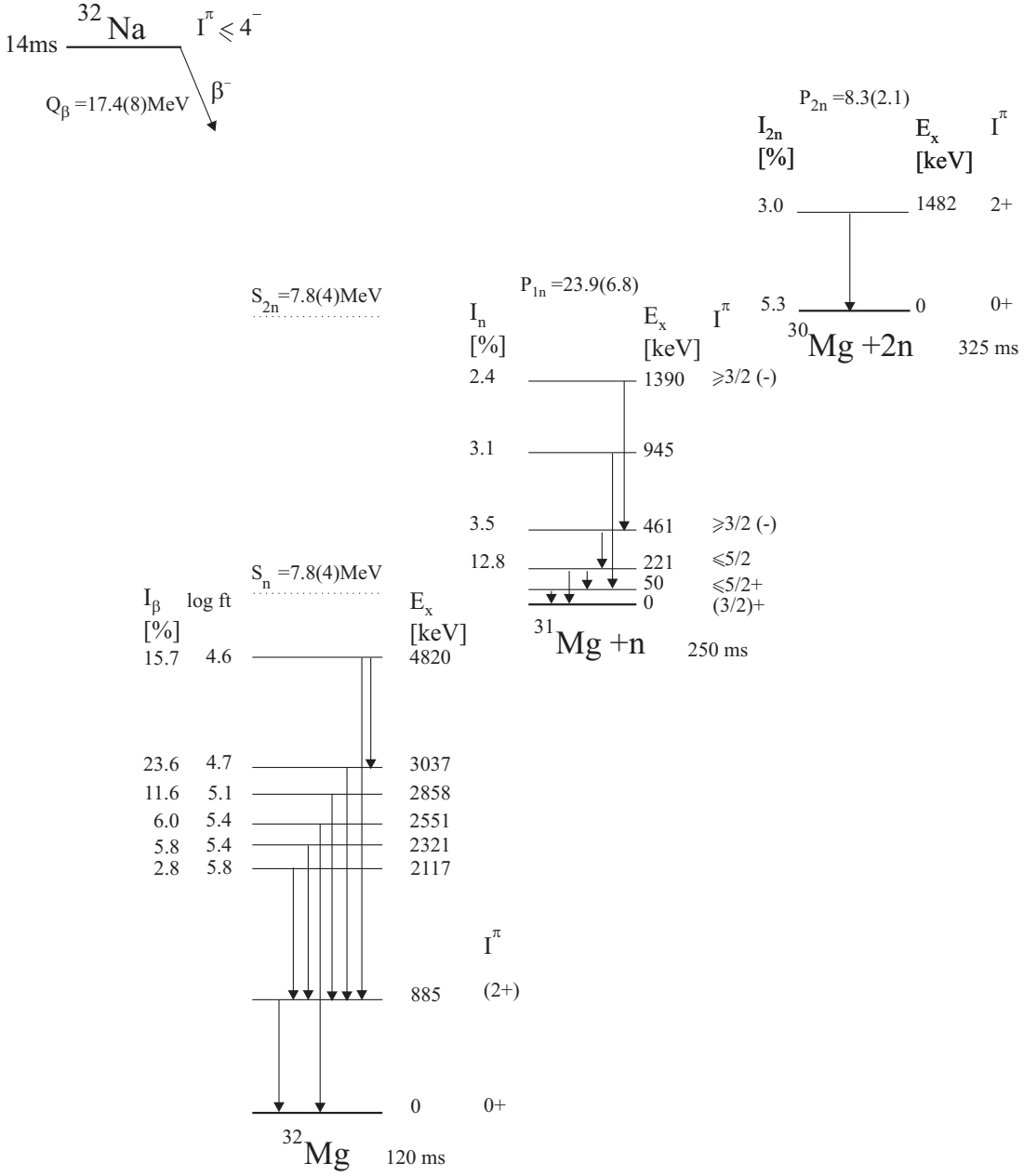

Figure 1.11: *Disintegration scheme of* ^{32}*Na [29].*

transitions between 50 and 250keV were measured by β delayed γ coincidence. The measured half life of the first excited state in ^{31}Mg (16.0(2.8)ns) and the nonobservation of the measured lifetime of the 171 and 221keV line, limits the multipole order of the 50keV and of the 221 and 171keV transitions to a dipole.

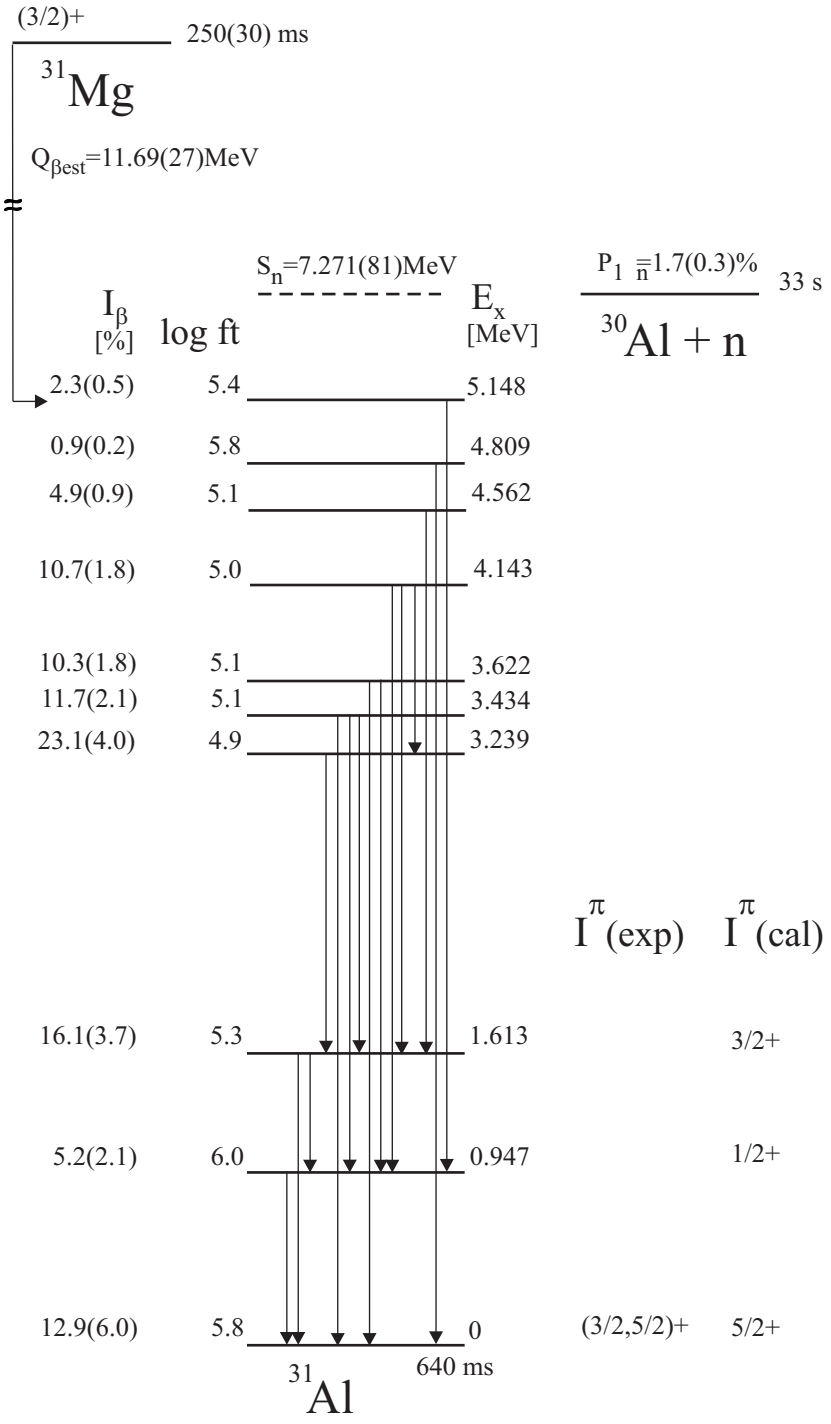

Figure 1.12: *Disintegration scheme of* ^{31}Mg. *The column at the right gives the theoretical* I^{π} *values obtained with USD shell model calculations [29].*

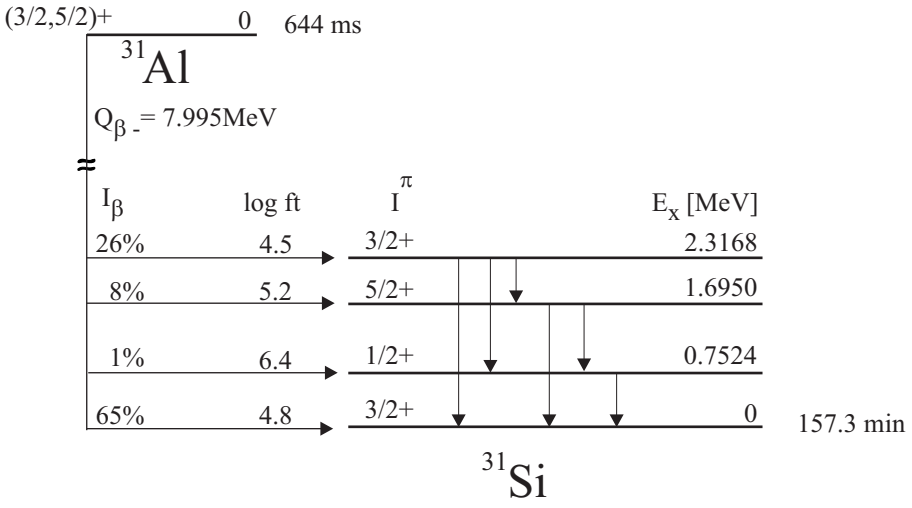

Figure 1.13: *Desintegration scheme of* ^{31}*Al [94].*

This results in the spin assignments as given in figure 1.10.
Interesting is the population of the 461 and 1390keV states related by a γ cascade through the β-delayed neutron decay of ^{32}Na, not observed in the ^{31}Na β decay. This suggests the population of levels with negative parity, resulting from the parity of the parent state ^{32}Na ($\pi = -$), figure 1.11.

Shell model calculations allowing two neutrons in the fp shell are in rather good agreement with the experimental energy levels of ^{31}Mg (figure 1.14), if one considers that, using USD calculations, the first excited state lies at 1.55MeV. The valence space for ^{31}Mg was enlarged compared with sd-pf calculations in the intruder region. The new configuration taken into account has one hole in the $2s_{1/2}$ shell, because the intruder configuration can be viewed as $^{29}\mathrm{Mg}\otimes(fp)^2$. And ^{29}Mg has its ground state $3/2^+$ almost degenerate with the $1/2^+$ state ($E_x = 54.6keV$), dominated by this configuration. This is a very peculiar situation which holds only for this nucleus. Moreover, the modification of the valence space has no appreciable consequences for nuclei other than ^{31}Mg. The ^{31}Mg ground state comes out as a 50% mixing of normal and intruder components. The half life of ^{31}Na, computed using the bare Gamow-Teller operator, is 4ms. With the usual renormalisation of 0.77 for the effective operator, the half life is 7ms, while the

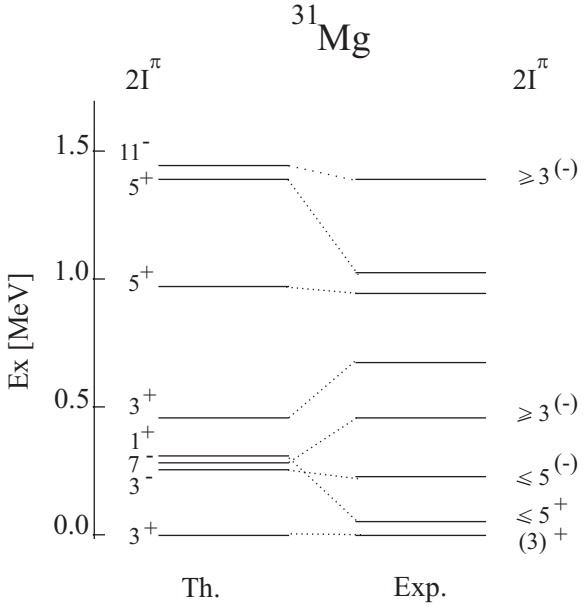

Figure 1.14: *Comparison of experimental and theoretical level structure of* ^{31}Mg *from the* ^{31}Na *decay [29].*

experimental value is 17ms. This discrepancy may suggest that the ^{31}Mg ground state is even more dominated by the intruder states. The experimental values of the Gamow-Teller strength for the states populated below 2MeV extracted from the measured decay of ^{31}Na, are in agreement with the general quenching factor of experiment relative to theory, which has been observed in most GT decays of sd or fp nuclei [31].

Considering ^{31}Al as a normal sd shell nucleus, $Q_\beta = 10.6$MeV is calculated for the decay of ^{31}Mg $\rightarrow$ ^{31}Al, compared to the experimental result $Q_\beta = 11.69(27)$MeV. Using the experimental value, one obtains $t_{1/2} = 120ms$ as the half life for ^{31}Mg with the bare Gamow-Teller operator. With the renormalised operator, the result becomes $t_{1/2} = 200ms$, compared to the experimental $t_{1/2} = 250ms$. USD calculations give a half life of 27ms using the renormalised operator.

The calculated Gamow-Teller strengths B(GT) puts too much intensity in the ground state of ^{31}Al by a factor of 8. Nevertheless, the obtained B(GT) in reference [29] shows a general agreement between the experiment and calculations,

and for the first three states the intensity is better reproduced by the inclusion of the intruder configurations.

The study of the β-decay of ^{32}Na showed a low lying first excited state in the even-even ^{32}Mg [28]. This was the second indication, after the mass measurements, that this nucleus could be well deformed. Coulomb excitation of ^{32}Mg to its 2^+ state was studied by T.Motobayashi *et al.* (Riken) [32], on ^{32,30}Mg by B.V.Pritychenko *et al.* (MSU) [33] and by A.Lépine-Szily *et al.* (GANIL) [34, 35]. The reaction cross section $\sigma(0^+_{g.s.} \rightarrow 2^+_1)$ of the secondary beam of ^{32}Mg on a heavy target was measured and a large reduced matrix element $B(E2; 0^+_{g.s.} \rightarrow 2^+_1) = 450e^2fm^4$ was deduced. The experimental $B(E2)$ is much larger than expected for a spherical nucleus with closed neutron shell, but the obtained value is comparable to shell model calculations in the sd-pf space for a nucleus with a 2p-2h configuration [20].
In the rotational model $B(E2; I_i \rightarrow I_f)$ and the Coulomb deformation β_C (the deformation reflecting the deformation in the proton density) are related to the first order via

$$B(E2; I_i \rightarrow I_f) = Q_0^2 \frac{5}{16\pi} < I_i K 20 | I_f K >^2 \quad (1.8)$$

$$Q_0 = \sqrt{\frac{16\pi}{5}} \frac{3}{4\pi} Z e R_0^2 \beta_C \quad (1.9)$$

Q_0 is the intrinsic quadrupole moment and the radius $R_0 = r_0 A^{1/3}$. When the proton and neutron deformation are taken equal, the quadrupole deformation parameter β_2 can be extracted directly. The three experiments obtained a large quadrupole deformation of $\beta_2 = 0.51(4)$ for ^{32}Mg. It does not provide direct information whether the deformation is static or dynamic, whether the static deformation is axially symmetric or whether an axially symmetric deformation is oblate or prolate. The overbinding of the nuclei provides strong evidence for static deformation. If a static quadrupole deformation with axial symmetry is assumed, the deformed shell model or Nilsson model can be used to calculate intrinsic quadrupole moments over a range of deformations by summing over the

contributions of the individual protons

$$Q_0 = (16\pi/5)^{1/2} \sum_{\lambda} < \lambda | r^2 Y_{20} | \lambda > \quad (1.10)$$

The quadrupole moments extracted from the B(E2) values can be reproduced if the nuclei have a substantial prolate deformation.

Similar experiments have been performed on ^{31}Na [36], where a first excited state is measured in agreement with shell model calculations [20] taking $\nu(f_{7/2}, p_{3/2})$ intruder states into account. A deformation parameter $\beta_2 = 0.58(8)$ close to the obtained value for ^{32}Mg is deduced.

In the case of ^{30}Mg, the situation is not clear. The obtained B(E2) is well reproduced [33] or larger [34, 35] compared with calculated values in the $0\hbar\omega$ model.

The first and second excited state of ^{34}Mg was studied by K.Yoneda *et al.* (Riken) [37] via a two-step projectile fragmentation reaction. A radioactive isotope beam of ^{36}Si was produced from the projectile fragmentation of ^{40}Ar, and ^{34}Mg were produced in the subsequent projectile fragmentation of ^{36}Si. Compared to Coulomb excitation experiments, higher excitation levels can be reached. The obtained excitation energy $E(2_1^+)$ is the lowest among the even-even isotopes nearby, even lower than that of ^{32}Mg, suggesting a very large deformation for this nucleus. The deduced ratio $E(4_1^+)/E(2_1^+) = 3.2$ is close to 10/3, which is expected for the rotational band of well-deformed isotopes where $E(I) = (\hbar^2/2\jmath)I(I+1)$. Monte Carlo shell model calculation in the full sd-pf space [38] reproduce the experimental $E(2_1^+)$ surprisingly well through the entire magnesium isotopic chain between N=16-22. The obtained theoretical value $E(4_1^+)/E(2_1^+) = 3.0$ for ^{34}Mg is also in good agreement.

1.4 Intruder characteristics in the neighborhood of the Island of Inversion.

Above the region of the Island of Inversion β decay studies [39], γ decay studies [40] and Coulomb excitation experiments [41, 42] showed that the ground states

and first excited states of the silicon isotopes ^{32,36,38}Si can be understood in terms of $0\hbar\omega$ (non intruder) configurations. They can be reproduced assuming a N=20 shell closure.

Table 1.3: Low-lying excited states with intruder character for silicon isotopes with $N \approx 20$.

		E_x [keV]	I^π	
^{33}Si	N=19	1435	$(7/2)^-$	$1\hbar\omega$
^{34}Si	N=20	2133	0^+	$2\hbar\omega$
		3305	2^+	$2\hbar\omega$
^{35}Si	N=21	974	$(3/2)^+$	$1\hbar\omega$

The low-lying excited states of isotopes with $N \approx 20$ can be found in table 1.3. A consistent description of the excitation energy of the 2_1^+ state at 3305(55)keV in ^{34}Si and the B(E2) value is possible in a shell model space that allows for a large component of the neutron fp-shell ($2\hbar\omega$) intruder state, while the ground state corresponds to a $0\hbar\omega$ configuration. A 0_2^+ state at 2133keV is assumed having a $2\hbar\omega$ character in order to interpret the observed γ transitions and B(E2) values. Therefore, ^{34}Si can be considered as a doubly magic nucleus, for which the ground state has a 0p-0h nature and the two lowest excited states are intruders [20].
An isomeric state with $t_{1/2}$=200(20)ns at 956keV is observed in ^{32}Al (N=19) [43, 40]. The lowest $1\hbar\omega$ and $2\hbar\omega$ estimated energies by shell model studies in the sdpf space using the WBMB interaction [7], give excitation energies of 959 and 2214keV respectively, relative to that of the energetically favored $0\hbar\omega$ configuration. Therefore, plausible candidates for a low-energy isomer arise from 0 or $1\hbar\omega$ configurations. Based on the life time of the isomer, a 4^+ state is assumed arising from the $0\hbar\omega$ sd shell space, however with an inversion of the nuclear levels obtained by the USD interaction. The ordering of the levels would be ex-

tremely rare and can only be explained with the Kuo G-matrix interaction for the sd-interaction, an older interaction used as starting point for the fitting that lead to the USD [44]. Unfortunately, from this interaction it is known that its main defect is that it moves whole bands of levels relative to one another, but the moments of inertia within the bands are reasonable accurate. This means that the excited band can be shifted with respect to the ground state [45].

In the region situated under the Island of Inversion less information is available since the isotopes are even more exotic and difficult to produce. Coulomb excitation at intermediate energy [33] proved that the energy of the 2_1^+ state in the N=18 isotope ^{28}Ne is considerably lower than the $0\hbar\omega$ prediction. Such a lowering in energy can be understood by the interaction between the $0\hbar\omega$ configuration which dominates the ground state and the more strongly deformed $2\hbar\omega$ configuration which occurs at a higher energy. The mixing of the two 2^+ states causes level repulsion, with the 2_1^+ state (still dominated by the $0\hbar\omega$ configuration) being pushed to a lower energy than the unmixed $0\hbar\omega$ state. The $0\hbar\omega$ $0_{g.s.}^+$ and the $2\hbar\omega$ 0_2^+ states mix as well. However, the energy shift of the 0^+ states due to the mixing will be smaller than that of the 2^+ states since the difference between the unperturbed energies of the 0^+ states is larger than that of the 0^+ states due to the smaller moment of inertia of the $0\hbar\omega$ configuration. ^{28}Ne is therefore clearly outside the deformation region.

Direct mass measurements indicated that the inversion in shell model level sequences observed for the N=20 ^{32}Mg and ^{31}Na may persist for ^{30}Ne. Based on large scale shell model calculations [20] the ground state of ^{30}Ne is expected to have a majority intruder character.

^{27,29}F (Z=9) and ^{29,30}Ne (Z=10) are produced and lifetimes measured [46, 47]. They are in good agreement with shell model calculations with the interaction of Retamosa *et al.* [48] which takes into account the spherical sd shell and the deformed fp intruder states. ^{31}F (Z=9) and ^{24}O (Z=8) are the neutron richest fluorine and oxygen isotopes observed [46]. The neutron drip line of F isotopes is located much further away as compared to that of O isotopes: at least six more neutrons can be contained in F isotopes, whereas it contains just one more

proton. Owing to 2p-2h and 4p-4h excitations, large attractive proton-neutron interaction are possible which makes the F isotopes bound. Oxygen has a closed proton shell, and the proton-neutron interaction becomes less important [19].

1.5 Theoretical approaches.

Several Shell Model calculations have been performed using different interactions, different valence spaces and with or without mixing by Warburton, Becker and Brown [7], by Courier, Nowacki and Poves [49] and by T.Otsuka *et al.* [50] and references therein. The mechanisms for lowering the $n\hbar\omega$ states are understood as consisting of two major ingredients: the monopole and the multipole terms of the Hamiltonian. The monopole gives the unperturbed energy of the different configurations. Far from stability, the energy gap between these configurations may be eroded because of the small binding energy of the orbits at the top of the well. The multipole terms in the N-N interaction, mainly pairing and quadrupole, further mix the single particle configurations. They can invert the energy ordering of the configurations given by the monopole. Summing up the lowering of the energy gap between the sd and fp shell when more neutrons are added, with an increase of the neutron-neutron pairing interaction and of the proton-neutron quadrupole interaction, may result in a more stable intruder configuration [49]. Whereas it has been demonstrated that one can obtain a fully reliable multipole hamiltonian, the monopole hamiltonian is usually incorrect [49]. By slight changes of this monopole term the limits of the intruder region are predicted differently, N=19 and N=22 are inside or outside depending on the calculation. Using the interaction by Poves and Retamosa (PR) [51] the transition from spherical to deformed takes place somewhere halfway between N=19 and 20 up to N=22 (for Z< 13). Calculations with the interaction of Retamosa *et al.* [48], an interaction where the cross shell matrix elements are modified in order to describe the neutron rich nuclei around N=28, predict $7/2^-$ ($1\hbar\omega$) as the ground state for ^{31}Mg. But, with a similar interaction by Caurier *et al.* [49]

with only a small change implemented to be able to reproduce experimental data on ^{35}Si, leads to a $3/2^+$ or $3/2^-$ ground state spin ($0\hbar\omega$ and a $1\hbar\omega$ coupled with a 2^+ proton configuration respectively). Therefore, measurements of the spin and static moments of nuclei in and around the island of inversion will yield vital information to fix the monopole terms of the cross shell interaction in the sd pf valence space.

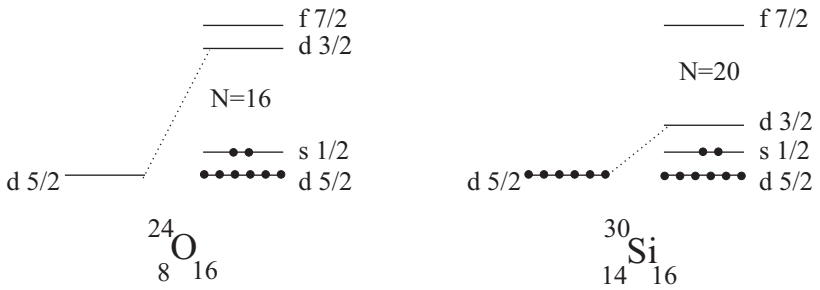

Figure 1.15: *The effective single particle energies for ^{30}Si and ^{24}O [50].*

Using the Monte Carlo Shell Model method, calculations without restriction on the valence space are performed by T.Otsuka *et al.* [50, 19]. T.Otsuka predicts that a new shell structure originates from a higher lying $d_{3/2}$ orbit inducing a new shell closure at N=16, figure 1.15. The part of the nucleon-nucleon (NN) interaction responsible for this process is written as

$$V_{\tau\sigma} \sim \tau \cdot \tau\sigma \cdot \sigma \tag{1.11}$$

here τ and σ stand for isospin and spin operators respectively. The σ operator couples the spin-orbit partners (j=l+1/2 and j=l-1/2, l being the orbital angular momentum and j the single particle angular momentum) strongly. And the τ operator favors the charge exchange processes. Combining these two properties, $V_{\tau\sigma}$ produces large matrix elements for the spin-flip isospin-flip processes: proton in j=l+1/2 $\rightarrow$ neutron in j=l-1/2 and vice versa. This gives rise to a strongly attractive monopole term.

In stable nuclei with $N \sim Z$, the neutron orbits are lowered by the proton spin-orbit partner and vice versa. In exotic nuclei, for example for ^{24}O with an empty

$d_{5/2}$ proton orbit (figure 1.15), this lowering can be absent, locating the highest spin-orbit partner not far from the upper shell. The disappearance of the N=20 shell closure arises from the small effective gap between the $d_{3/2}$ and fp shell for neutrons. It is caused by the absence of the strong attractive interaction between the protons in the $d_{5/2}$ and the neutrons in $d_{3/2}$, two spin-orbit coupling partners.

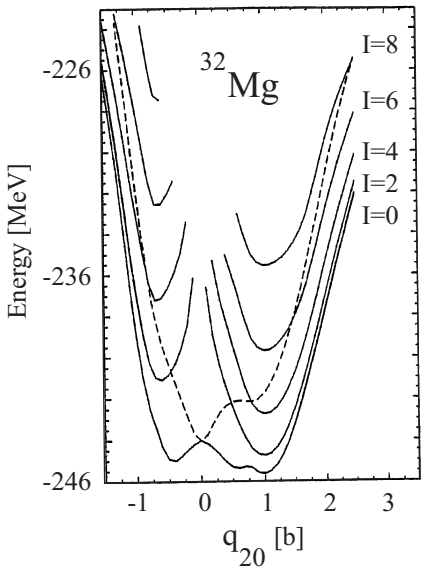

Figure 1.16: *The HFB (dashed line) and the AMP energies of* ^{32}*Mg [52].*

Relativistic mean field studies [53, 54] as well as Hartree-Fock Bogolioubov calculations (HFB) predicted a spherical shape for ^{32}Mg [55]. More recently, angular momentum projected generator coordinate method calculations (AMP-GCM) with the Cogny interaction and the mass quadrupole moment as generating coordinate were performed on ^{30,32,34}Mg by R.R.Rodríguez-Guzmán *et al.* [52]. On the deformation energy curve of the HFB calculation on ^{32}Mg (figure 1.16), an inflection point is visible at prolate deformation. Using the AMP method, for I=0 and 2, a prolate and an oblate minimum appear with almost the same energy for the nucleus ^{30}Mg, whereas the prolate minimum becomes significantly deeper corresponding to a deformation parameter $\beta = 0.4$ for ^{32,34}Mg. For increasing spins, the prolate minimum is even more pronounced.

The actual preference for a spherical or deformed ground state in mean field studies varies with the used two body interacting force [56]. The nucleus ^{32}Mg has been found to be an example of shape coexistence. The spherical and deformed configurations are close in energy and shape mixing is expected. This is consistent with recent measurements at GANIL by F.Azaiez *et al.* [57], according to which the E_{4+}/E_{2+} ratio in ^{32}Mg falls well below the rotational limit.

1.6 Objectives of the experiments.

By performing a β Level Mixing Resonance (LMR) experiment on ^{29,31}Mg after a fragment separator, the spin, the ratio of the quadrupole moment to the magnetic moment and the magnetic moment is obtained. The magnetic moment of ^{31}Al and ^{31}Mg is also studied using the Nuclear Magnetic Resonance (NMR) method. All studied isotopes are situated at the limits of the Island of Inversion.
The experiments are performed at GANIL (France). In order to study the static moments, the nuclei need to be spin oriented. In these specific experiments the orientation is obtained in the fragmentation reaction. Since it was the first time spin polarization was studied at Ganil, a test on ^{27}Na, a well understood nucleus, was performed. ^{27}Na was chosen since it has similar half life, Q_β and magnetic moment as assumed for ^{31}Mg and it has the major advantage that it is well produced in the fragmentation reaction and has a large asymmetry factor, figure 1.17.

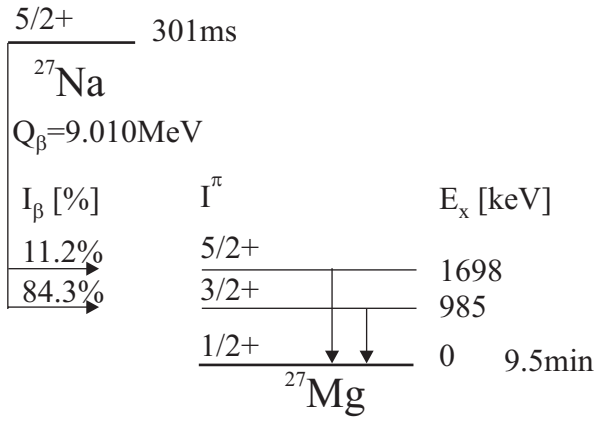

Figure 1.17: *Desintegration scheme of* ^{27}*Na [94].*

Chapter 2

β-LMR on ^{31}Mg and ^{29}Mg

2.1 Level Mixing experiments at a fragment separator.

The Level Mixing Resonance technique applied to β-decaying nuclei (β-LMR) [58] is a well established tool for measuring the ground state moments of nuclei far from stability [59].

In this section, some specific details of a LMR measurement performed at a fragment separator will be clarified. Not only the spin and the ratio of quadrupole to the magnetic moment can be obtained, but also the magnetic moment separately. Most techniques to measure moments need spin oriented nuclei. A major advantage of the β-LMR technique is that the initial nuclei need only to be aligned, and not necessarily polarized. Alignment is easier to produce via the nuclear reaction mechanism, and is obtained for the fragments selected in the forward direction [60, 61, 62] where the highest yield will be obtained.

2.1.1 The orientation of the nuclear spin.

Before mentioning how spin orientation can be obtained, the different types of orientation will be defined in a formal way.

An ensemble of nuclei with spin I is called spin-oriented if the nuclear spins have a preferential direction in space. By defining a Z_{OR}-axis, one can describe the spin orientation with respect to this axis as the probability $p(m)$ that the nuclear spin has a projection $|m\rangle$ of the nuclear spin onto this axis. The density matrix formalism can be used to describe the orientation:

$$\rho_{mm'} = \langle m|\rho|m'\rangle \tag{2.1}$$

with diagonal elements $\rho_{mm} = p_m$ describing the spin projections, and the non diagonal elements describing the coherence between different m-states. An axial symmetric ensemble has only the diagonal elements different from zero. The density matrix is related to the density tensor ρ_k^n:

$$\rho_k^n = \sqrt{2k+1} \sum_{mm'} (-1)^{I+m} \begin{pmatrix} I & I & k \\ -m & m' & n \end{pmatrix} \langle m|\rho|m'\rangle \tag{2.2}$$

and to the orientation tensor:

$$B_k^n = \sqrt{2I+1}\, \rho_k^{n*} \tag{2.3}$$

From the last two formulas one can derive that in case of axial symmetry, when $m = m'$, the orientation tensor will only contain $n = 0$ components. This simplifies the description of an axially symmetric oriented system.

In the angular distribution formula the spin orientation will always be described by the orientation tensor, because it allows an easy transformation from one axis system to another by rotation over the Euler angles [63]. However, when speaking about the amount of orientation, a different terminology is used, depending on the type of orientation. Two possible initial axial symmetric orientations will be considered. When the probability to have the spins along the symmetry axis is equal for both directions, $p(m) = p(-m)$, the ensemble of nuclei is spin-aligned, figure 2.1. When $p(m) \neq p(-m)$ the ensemble is spin-polarized, figure 2.2. Note that a polarized ensemble is also spin-aligned. The amount of initial alignment A and polarization P in case of axial symmetric orientation is defined as:

$$A(I) = \sum_m \frac{[3m^2 - I(I+1)]\, p(m)}{|\alpha_2(max)|} \tag{2.4}$$

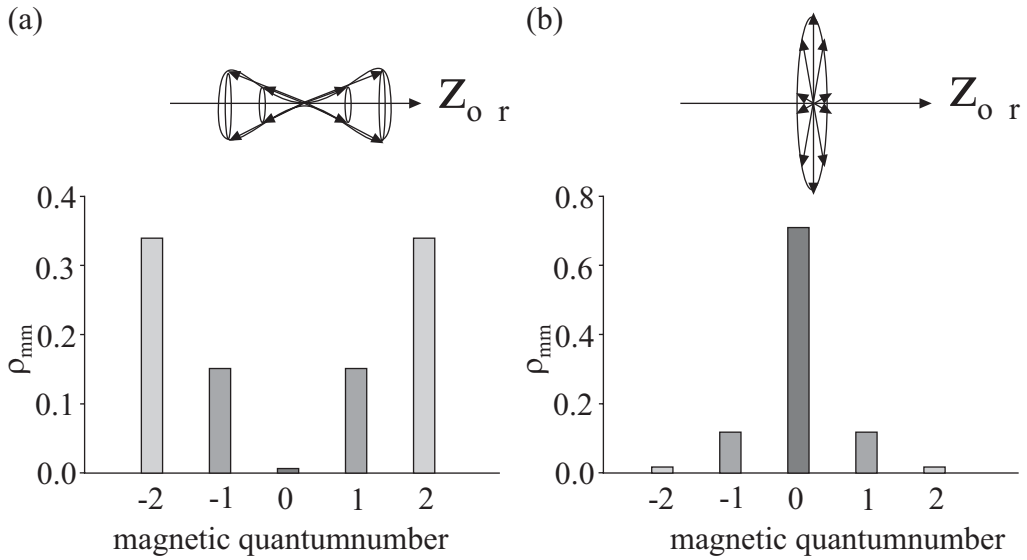

Figure 2.1: *The nuclear ensemble is spin aligned when* $p(m) = p(-m)$*, (a) prolate alignment* $(A > 0)$*, (b) oblate alignment* $(A < 0)$*.*

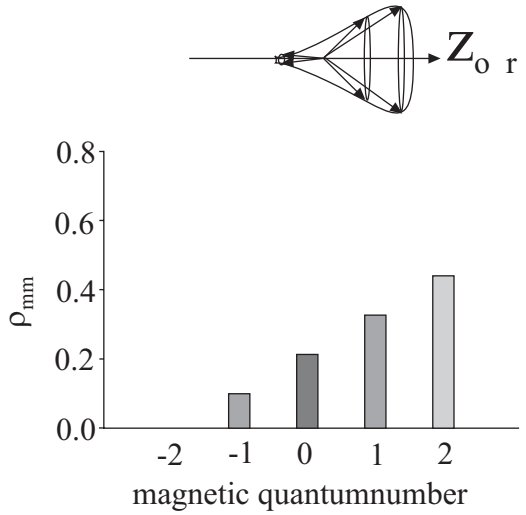

Figure 2.2: *The ensemble is spin polarized when* $p(m) \neq p(-m)$*.*

$$P(I) \;=\; \frac{1}{I}\sum_{m} m\, p(m) \tag{2.5}$$

with $\alpha_2(max)$, for oblate alignment $(A < 0)$ and integer spin defined as $\alpha_2(m = 0) = I(I+1)$ and for half integer spin defined as $\alpha_2(m = \pm 1/2) = I(I+1) - 3/4$.

For prolate alignment ($A > 0$) $\alpha_2(max)$ is defined as $\alpha_2(m = \pm I) = I(2I-1)$ for all spins.

Spin polarization is described by the odd tensor components $B^0_{1,3,5,...}$ and spin alignment with the even components $B^0_{2,4,6,...}$, both orientations in their own orientation frame (OR_A and OR_P). If we neglect higher order contributions to the alignment and polarization, then B^0_1 and B^0_2 are related to the initial alignment A and polarization P as follows [64]:

$$B^0_1(I, t=0)_{OR_P} = -\sqrt{\frac{3I}{I+1}}\,P(t=0) \tag{2.6}$$

$$B^0_2(I, t=0)_{OR_A} = \frac{\sqrt{5}|\alpha_2(max)|}{\sqrt{I(I+1)(2I+3)(2I-2)}}\,A(t=0) \tag{2.7}$$

The observed nuclei are oriented by the fragmentation reaction. When the fragments are selected in the forward direction with respect to the primary beam, the fragments are shown to be spin aligned [60, 61, 62]. As the recoil nuclei are mainly emitted in the forward direction, the highest yield will be obtained. Asahi et al. developed a model to describe the production of orientation [60]. This is based on the "participant-spectator" model, a rather simple model to describe the fragmentation reaction, [65, 66, 67].

2.1.2 The formalism for β-LMR at a recoil separator.

In LMR experiments, an ensemble of spin-oriented nuclei with spin I are implanted into a crystal, immersed in an external static magnetic field B. The non-cubic crystal has an axially symmetric electric field gradient V_{ZZ} along the C-axis, positioned at a small angle β with respect to the magnetic field. This electric field gradient (EFG) defines the principle axis system (PAS) with Euler angles $(\alpha, \beta, 0)$ for a transformation from the LAB-frame towards the PAS-frame, figure 2.3. The combination of the electric quadrupole and magnetic dipole interaction leads to the following Hamiltonian described in the principal axis system:

$$H_{LMR} = H_Q + H_B$$

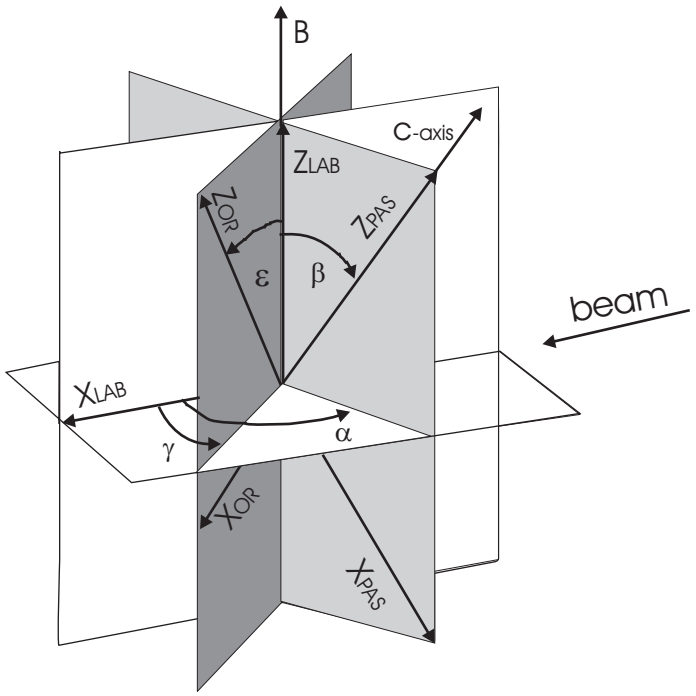

Figure 2.3: *Frame definition for the principal axis system (PAS) and the orientation (OR) frame with respect to the laboratory (LAB) frame. There is a separate orientation frame for the alignment* (OR_A) *and for the polarization* (OR_P).

$$= \frac{\omega_Q}{\hbar}(3I_Z^2 - I^2) + \omega_B I_Z \cos\beta - \omega_B I_X \sin\beta \tag{2.8}$$

with $\omega_B = -\frac{g\mu_N B}{\hbar}$ the magnetic interaction frequency and $\omega_Q = \frac{eQV_{ZZ}}{\hbar 4I(2I-1)}$ the quadrupole interaction frequency. Q is the spectroscopic quadrupole moment of the implanted nuclei, g the g-factor with $\vec{\mu} = g\mu_N\vec{I}$ the magnetic moment of the nuclei.

When the angle $\beta = 0^0$ between the static field B and the EFG, the orientation of the EFG coincides with the magnetic field. The Hamiltonian is axially symmetric in the PAS frame and the eigenstates $|m\rangle$ are fully determined by the magnetic quantum number m, the projection of $\vec{I}$ on the Z_{PAS} axis. A Breit-Rabi diagram shows the energy of the different eigenstates $|m\rangle$ as a function of the static magnetic field, figure 2.4(a) with

$$E_m = -\hbar\omega_B m + \hbar\omega_Q(3m^2 - I(I-1)) \tag{2.9}$$

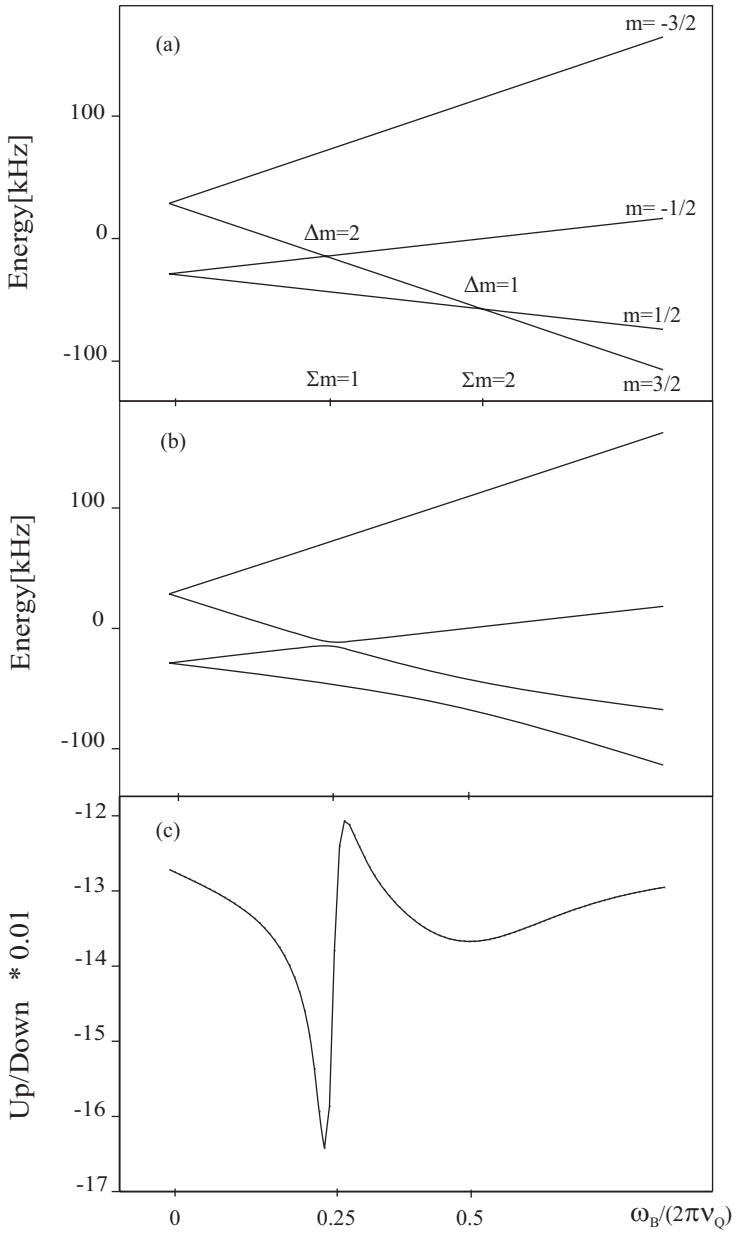

Figure 2.4: *(a) A Breit-Rabi diagram of a nucleus with spin $I = 3/2$ and tilt angle $\beta = 0^0$, (b) and tilt angle $\beta = 15^0$. When the populations of the hyperfine levels mix, the levels repel each other. (c) The up/down asymmetry as a function of a static magnetic field for $\beta = 15^0$, $B_1^0 = 0.2$, $B_2^0 = 0.2$, $\gamma_A = 2^0$, $\varepsilon_P = 90^0$ and $\gamma_P = 92^0$.*

and crossing of the sublevels occurs when $E_m = E_{m'}$, this is at equidistant distances when

$$\begin{aligned} \omega_B &= 3(m+m')\,\omega_Q \\ \Rightarrow \frac{\omega_B}{\nu_Q 2\pi} &= \frac{3(m+m')}{4I(2I-1)} \end{aligned} \tag{2.10}$$

The spin of the nuclei defines the number of eigenstates $|m\rangle$ and so the number of crossing sublevels. Moreover, equation 2.10 shows clearly how the distance between two crossing fields depends on the spin and that there is an equidistant distance $\frac{3}{4I(2I-1)}$ between two crossing fields.

For a small tilt angle β, the last term of the Hamiltonian can be considered as a perturbation. It causes breaking of the axial symmetry, giving rise to a level mixing interaction [68, 69, 58]. The sublevels $|m\rangle$ and $|m'\rangle$ will cross at a static magnetic field B when:

$$\begin{aligned} \omega_B &= 3(m+m')\cos\beta\,\omega_Q \\ \Rightarrow \frac{\omega_B}{\nu_Q 2\pi} &= \frac{3(m+m')\cos\beta}{4I(2I-1)} \end{aligned} \tag{2.11}$$

The level mixing is seen as a repelling of the two respective hyperfine m-quantum states, figure 2.4(b).

Near two crossing levels with $\Delta m = |m - m'|$ a "two level" approximation is allowed for small β. The mixed eigenstates, $|N\rangle$ and $|N'\rangle$, and the energy levels of the perturbed system can be calculated with quasi-degenerate perturbation theory, [68]:

$$\begin{aligned} |N\rangle &= \frac{1}{\sqrt{1+R^2}}(|m\rangle - R|m'\rangle) \\ |N'\rangle &= \frac{1}{\sqrt{1+R^2}}(R|m\rangle + |m'\rangle) \end{aligned} \tag{2.12}$$

with energy:

$$E_{N,N'} = \frac{E_m + E_{m'}}{2} \pm 1/2\sqrt{(E_m - E_{m'})^2 + 4(W^{\Delta m}_{mm'})^2} \tag{2.13}$$

and mixing parameter R depends on the perturbation matrix element $W^{\Delta m}_{mm'}$. It is a function of the static interaction frequencies ω_B, ω_Q and is proportional to

$(\sin\beta)^{\Delta m}$:

$$R = \frac{E_m - E_{m'}}{2W^{\Delta m}_{mm'}} + \sqrt{\left(\frac{E_m - E_{m'}}{2W^{\Delta m}_{mm'}}\right)^2 + 1} \tag{2.14}$$

The breaking of the axial symmetry induces mixing of the level populations, and so a resonant change of the initial spin orientation. This change of orientation can be measured by the time integrated angular distribution, $W(\theta, \varphi, \tau)$, of the radioactive β-decay but in simulations and for the experiments the Up/Down asymmetry will be observed, this is $W(0^0, \varphi, \tau)/W(180^0, \varphi, \tau)$, figure 2.4(c).
The time integrated angular distribution of the decay of the perturbed nuclear system can be calculated in the LAB-frame:

$$W(\theta, \varphi, \tau)_{LAB} = \sqrt{4\pi} \sum_{k,n} A_k \, B^n_k(I, \tau)_{LAB} \, Y^n_k(\theta, \varphi)_{LAB} \tag{2.15}$$

Two possible initial orientations will be considered, spin alignment $B^0_{2,4,6,\ldots}$ and spin polarization $B^0_{1,3,5,\ldots}$. Only B^0_2 and B^0_1 will be taken into account since the higher order tensors have a negligible contribution for nuclei with $I < 4\hbar$ [64]. Both orientations are described in their own orientation frames, OR_A and OR_P, with Euler angles defined as $(\varepsilon_A, \gamma_A, 0)$ and $(\varepsilon_P, \gamma_P, 0)$ for a transformation from the LAB-frame towards the respective OR-frame, figure 2.3. The orientation of the nuclei is observed in the laboratory frame. By transforming the initial orientation tensors from the OR-frame to the LAB-frame, tensors B^n_k with $n \neq 0$ become different from zero:

$$B^n_k(I, t=0)_{LAB} = \sqrt{\frac{4\pi}{2k+1}} \, e^{+in\gamma} \, Y^n_k(\varepsilon, 0) \, B^0_k(I, t=0)_{OR} \tag{2.16}$$

The time integrated orientation parameters can be written as a function of the initial orientation and the time integrated perturbation factors $G^{nn'}_{kk'}(I, \omega_B, \omega_Q, \tau)$:

$$B^n_k(I, \tau)_{LAB} = \sum_{k',n'} G^{nn'}_{kk'}(I, \omega_B, \omega_Q, \tau)_{LAB} \, B^{n'}_{k'}(I, t=0)_{LAB} \tag{2.17}$$

From equation 2.17 and 2.16 one can deduce that the initial alignment can be measured $B^0_{k'=2}(I, t=0)_{OR_A}$, although only β-particles are detected and $A_{k=1}$ will be the main contributing radiation parameter in equation 2.15.

The perturbation factors are a function of the magnetic and quadrupole interaction [68], and can be computed by expressing the Hamiltonian in the LAB frame and diagonalising it numerically.

An analytic expression for the perturbation factor gives more insight into the behaviour of the angular distribution as a function of the applied magnetic field. The perturbation factors can be calculated explicitly if the nuclear Hamiltonian is expressed in the principal axis system. Near two crossing levels with $\Delta m = |m - m'|$ quasi degenerate perturbation theory can be applied and equation 2.15 can be rewritten as:

$$\begin{aligned} W(\theta,\varphi,\tau) \;=\; & 1 + \cos\theta\, A_1 \Big[\cos\varepsilon_P \Big(1 + 1/2(\sum_i g^i_{11}(L)\mathbf{L}_i)\Big)\, B^0_1(I,t=0)_{OR_P} \\ & -\sqrt{1/2}\,\sin\varepsilon_P\;\cos\gamma_P \Big(\sum_{i(\Delta m=1)} g^i_{11}(D)\mathbf{D}_i\Big)\, B^0_1(I,t=0)_{OR_P} \\ & +1/4\,\Big(3\cos^2\varepsilon_A - 1\Big)\Big(\sum_i g^i_{12}(L)\mathbf{L}_i\Big)\, B^0_2(I,t=0)_{OR_A} \\ & -\sqrt{3/2}\,\sin\varepsilon_A\,\cos\varepsilon_A\;\cos\gamma_A \Big(\sum_{i(\Delta m=1)} g^i_{12}(D)\mathbf{D}_i\Big)\, B^0_2(I,t=0)_{OR_A} \\ & +\sqrt{3/8}\,\sin^2\varepsilon_A\;\cos 2\gamma_A \Big(\sum_{i(\Delta m=2)} g^i_{21}(D)\mathbf{D}_i\Big)\, B^0_2(I,t=0)_{OR_A} \Big] \end{aligned} \tag{2.18}$$

with the Lorentz absorption resonance

$$\mathbf{L}_i = \frac{(2W^{\Delta m}_{m_i m_{i'}})^2}{(E_{m_i} - E_{m_{i'}})^2 + (2W^{\Delta m}_{m_i m_{i'}})^2} \tag{2.19}$$

and Lorentz dispersion resonance

$$\mathbf{D}_i = \frac{2W^{\Delta m}_{m_i m_{i'}}(E_{m_i} - E_{m_{i'}})}{(E_{m_i} - E_{m_{i'}})^2 + (2W^{\Delta m}_{m_i m_{i'}})^2} \tag{2.20}$$

The summation over i is a summation over all mixing levels at the resonance field, while the summation over $i(\Delta m)$ is restricted to these levels which have $\Delta m_i = \Delta m$. The factors $g^i_{kk'}$ determine the amplitude of the resonances. They are sums of 3J-symbols and independent of the misalignment angle β. The resonant behaviour of the perturbation factors and thus of the angular distribution near a level mixing is expressed in the Lorentz absorption and dispersion resonances.

Due to symmetry considerations, the Z-axis of the orientation frame of an aligned

ensemble (Z_{OR_A}) of nuclei right after the production target is parallel to the beam axis, therefore $\varepsilon_A = 90^0$ and $\gamma_A = 0^0$. When the secondary beam is purified by

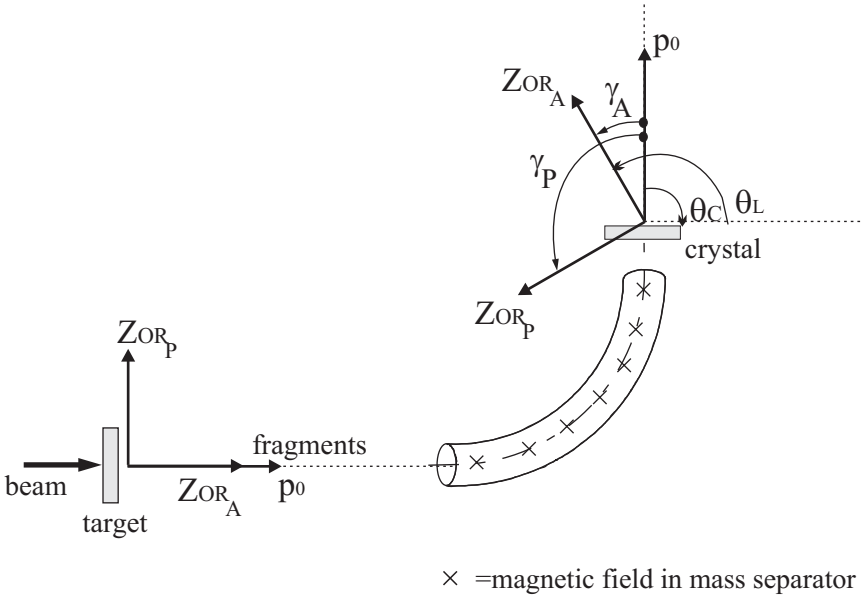

Figure 2.5: *The angle γ_A and γ_P between the direction of the fragments and the orientation axis of the initial alignment and polarization.*

a recoil mass separator, the beam rotates over a different angle $\theta_C = \omega_C.t$ than the nuclear orientation axis of the alignment $\theta_L = \omega_L.t$, because the Larmor frequency $\omega_L = -g\mu_N B/\hbar$ is different from the cyclotron frequency $\omega_C = qB/m$, with q and $m = A.u$ the charge and the mass of the nuclei. Therefore, the initial orientation axis for an aligned ensemble is not parallel to the beam after the dipole magnets, figure 2.5:

$$\gamma_A = \theta_C + \theta_L = \theta_C(1 - \frac{gA}{2q}) \tag{2.21}$$

In case of polarized fragments, the symmetry axis Z_{OR_P} is perpendicular to the beam direction, see further in section 3.1.1, thus $0^0 \leq \varepsilon \leq 180^0$ and $\gamma_P = \pm 90^0$. Similar as for alignment, if the secondary beam passes through a mass separator, figure 2.5, the angle between the orientation axis and the beam direction becomes:

$$\gamma_P = \pm 90^0 + \theta_C(1 - \frac{gA}{2q}) \tag{2.22}$$

At the Lise spectrometer, section 2.2, $\theta_C = -90^0$. At LISEIII (after the Wien filter), $\theta_C = -60^0$. The measured Up/Down asymmetry can be rewritten as:

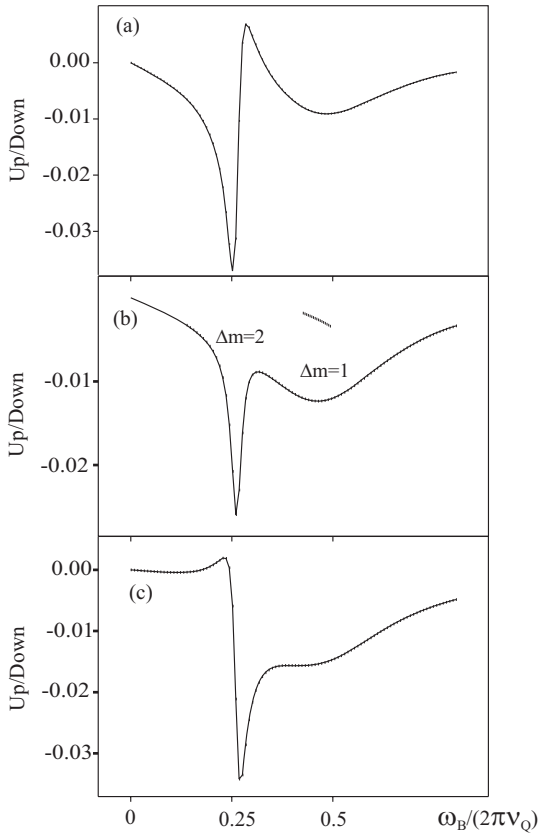

Figure 2.6: *The Up/Down asymmetry for spin aligned nuclei with $I = 3/2$, tilt angle $\beta = 15^0$, $B_2^0 = 0.2$ and different magnetic moments at the LISEIII spectrometer $\theta_C = -60^0$. The difference can only be seen in the $\Delta m = 2$ resonance (a) $\mu = 1.2 n.m.$ $\gamma_A = 2^0$, (b) $\mu = 2.0 n.m.$ $\gamma_A = 43^0$, (c) $\mu = -1.0 n.m.$ $\gamma_A = -111^0$.*

$$\begin{aligned}\frac{W(0^0,\varphi,\tau)}{W(180^0,\varphi,\tau)} \approx\ & 1 + 2\,A_1 \Big[\cos\varepsilon_P \Big(1 + 1/2(\sum_i g^i_{11}(L)\mathbf{L}_i)\Big)\, B^0_1(I, t=0)_{OR_P} \\ & -\sqrt{1/2}\,\sin\varepsilon_P\ \cos\gamma_P \Big(\sum_{i(\Delta m=1)} g^i_{11}(D)\mathbf{D}_i\Big)\, B^0_1(I, t=0)_{OR_P} \\ & +1/4\,\Big(\sum_i g^i_{12}(L)\mathbf{L}_i\Big)\, B^0_2(I, t=0)_{OR_A} \\ & +\sqrt{3/8}\,\cos 2\gamma_A \Big(\sum_{i(\Delta m=2)} g^i_{21}(D)\mathbf{D}_i\Big)\, B^0_2(I, t=0)_{OR_A}\Big] \quad (2.23)\end{aligned}$$

It is clear that for $\Delta m = 2$ $(I \geq 3/2)$, even if the nuclei are only spin aligned and not spin polarized, the angular distribution is sensitive to the g-factor via γ_A, equation 2.21, figure 2.6. The $\Delta m = 2$ resonance varies from a pure Lorenz resonance for $\gamma_A \approx \pm 45^0$, to a dispersion superimposed on a Lorenz resonance when $\gamma_A \approx 0^0$ or $\gamma_A \approx \pm 90^0$. If the nuclei are also spin polarized and if $\varepsilon_P \neq 0^0$ or $\varepsilon_P \neq 180^0$, the angular distribution reflects the g-factor already at $\Delta m = 1$, thus for spins $I \geq 1$.

It is very important to understand that because of this one can not only deduce the ratio of the quadrupole moment to the magnetic moment from the LMR resonance, but also the magnetic moment separately. Although, when fitting the experimental data with a LMR curve, the deduced value of the g-factor has a lousy accuracy $(> 50\%)$, the sign of the g-factor can be deduced unambiguously. Secondly, from the number of resonances and dispersions, and from the distance between two resonances, one can deduce the spin.

2.2 The experimental setup for β-LMR on ^{31}Mg.

The ^{31}Mg nuclei are neutron rich, light, exotic nuclei. They are produced and oriented by a fragmentation reaction at the Grand Accélérateur National d'Ions Lourds (GANIL, Caen, France), figure 2.7. A primary beam of $^{36}S^{16+}$ with an intensity of 1.5 to $2\mu A$ is accelerated by two segmented cyclotrons (Cyclotron à Secteurs Séparés: CSS1 and CSS2) to 77.5MeV/u and directed to the LISE beam line (Ligne d'Ions Super Epluchés) via the α-spectrometer.

The alpha spectrometer is a combination of dipole magnets and slits. Since in beam transport systems, the transmission of the beam as a whole and not the individual trajectories of the ions are important, the two main characteristics of the beam, its diameter and its divergence, are combined in one parameter, namely its phase space [70]. In this space a system is associated by the position coordinates of the N particles and by the conjugate momentum coordinates, and behaves like an incompressible fluid. The trajectory in the phase space of a particle with

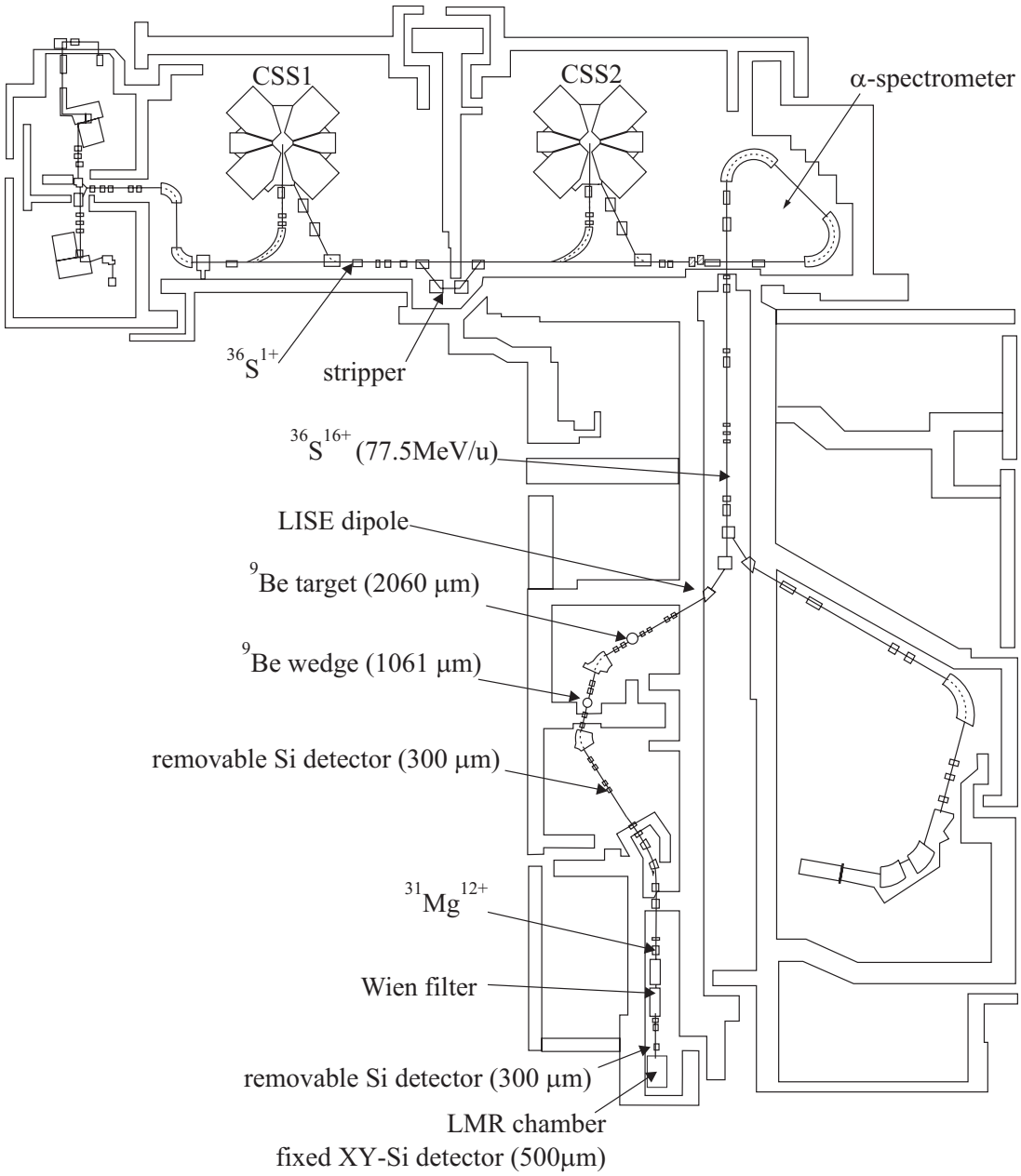

Figure 2.7: *Overview of the experimental hall of GANIL. The experiments were performed at LISEIII with a primary beam of $^{36}S^{16+}$ on a ^{9}Be target and wedge shaped degrader. Two silicon detectors are put in the beam line, one after the LISE spectrometer and one before the LMR setup.*

position $x = x_{MAX}\sin(\omega t)$ and conjugate momentum $p_x = m\omega x_{MAX}\cos(\omega t)$ is an ellipse, figure 2.8:

$$\frac{x^2}{x_{MAX}^2} + \frac{p_x^2}{p_{MAX}^2} = 1 \tag{2.24}$$

A beam going through a focusing system with opening $2a$ cannot accept particles

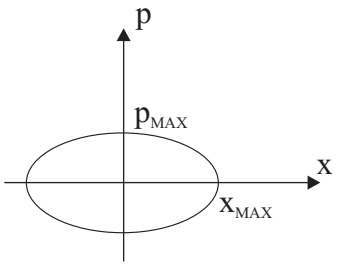

Figure 2.8: *The phase space reduced to the phase plane x, p_x. The emittance of the beam is the limiting area $\pi.x_{MAX}.p_{MAX}$ the ellipse occupies drawn in this space.*

lying outside the limiting ellipse with semiaxes a and $b = m\omega a$. The limiting ellipse in the phase space is called the emittance of the beam. The emittance of the beam after the alpha spectrometer is $6 * 6\pi$ mm.mrad.
At LISE, the beam is bombarding a rotating ^{9}Be target of $2071\mu m$.
Since LMR experiments require only alignment for spin orientation, the fragments are selected in the forward direction, so the highest yield is obtained [60, 61, 62]. The LISE-spectrometer not only mass separates the fragments according to the Projectile Fragmentation Isotopes Separation (PFIS) [71], but it also makes a selection in longitudinal momentum of the selected fragment, i.e. the momentum in the direction of the secondary beam [71, 72]. LISEIII is the combination of the LISE-spectrometer and the velocity or Wien filter.

2.2.1 Selection of the fragment.

The spectrometer consists of two dipole magnets and a wedge shaped degrader, $1062\mu m$ of ^{9}Be, halfway the two deflection magnets.

The dipole magnets permit a deviation of the secondary fragment beam according to their charge state, speed and mass. The determination of the magnetic rigidity $B\rho$ is a measurement of the deviation of the beam:

$$B\rho = \frac{\gamma m \beta}{qc} \tag{2.25}$$

$$\Rightarrow \frac{A}{q} = \frac{1}{3.1071}\frac{B\rho}{\beta\gamma} \tag{2.26}$$

with B the magnetic field in $[T]$, ρ the radius of the bending in $[m]$, m the mass of the nucleus in $[J]$ and A in $[a.m.u.]$, q the charge of the ion ($q \leq Z$), $c = 2.9979\ 10^8 m/s$, v the velocity of the nucleus in $[m/s]$, $\beta = v/c$ and $\gamma = \frac{1}{\sqrt{1-\beta^2}}$. The degrader, situated in the intermediate focal plane, purifies the secondary beam composed of several ions with a different charge state. The shape of the degrader preserves the achromaticity of the spectrometer. The energy loss is a characteristic of the ions with a specific mass A and atomic number Z:

$$\frac{dE}{E} \cong eK\frac{A^3}{Z^2} \tag{2.27}$$

with e the thickness of the degrader, K a constant associated with the degrader. The first dipole with $B\rho_1 = 2.8944 Tm$ selects only these nuclei with $A/Z = 31/12 = 2.58$. The degrader, in combination with the second dipole $B\rho_2 = 2.6665 Tm$, makes a second selection and accepts only nuclei which fulfill the condition $A^3/Z^2 = 31^3/12^2 = 206.88$, figure 2.9. The momentum acceptance of

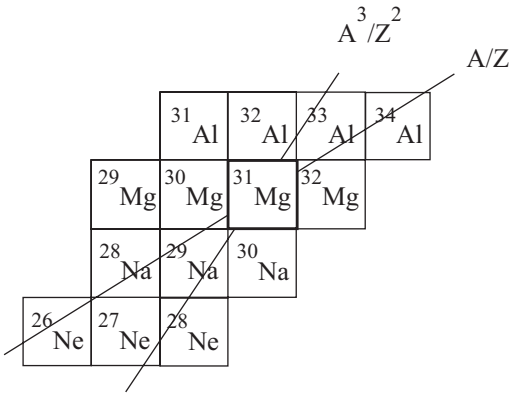

Figure 2.9: *The selection of the ^{31}Mg fragments by the LISE-spectrometer.*

the spectrometer is set to $\Delta p/p = 0.77\%$ (as low as the counting rate admits) in order not to lose the orientation.

2.2.2 Selection of the momentum of the fragment.

Fragment momentum distributions measured in relativistic heavy ion collisions are typically observed to be Gaussian shaped, discribed by the Goldhaber statistical model [73] with a parallel momentum width:

$$\sigma_{\parallel}^{gold} = \sigma_0 \sqrt{\frac{A_f(A_p - A_f)}{(A_p - 1)}} \tag{2.28}$$

A_f and A_p is the fragment respectively the projectile mass number, σ_0 is the reduced width.

A more universal model of the momentum distribution also valid at intermediate energies is developed and implemented in the LISE program [74], taking into account the occurrence of an exponential tail at lower energies and the reduction of the velocity relation of a fragment to projectile $v_f/v_b < 1$. To describe the experimental distributions of fragmentation products a convolution is used between a gaussian and an exponential lineshape for the tail reactions, like transfer reactions mainly at lower energies. The settings of the spectrometer come down to the selection in the center of the momentum distribution, figure 2.11.

In the experiments the higher energy side of the momentum distribution will be selected. This means we gain not only in purity, figure 2.12, but we also favor the fragmentation reaction over the transfer reaction. Note that the predicted alignment [60] is based on a Goldhaber distribution. In the tail of the convolution lower energy reactions take place, like transfer reactions. It is not clear how the orientation will behave for these lower energy reactions.

2.2.3 Detection and identification of the fragment.

A silicon detector of $300\mu m$ in front of the measurement chamber, figure 2.7, gives two signals when a fragment passes through the detector. One signal proportional

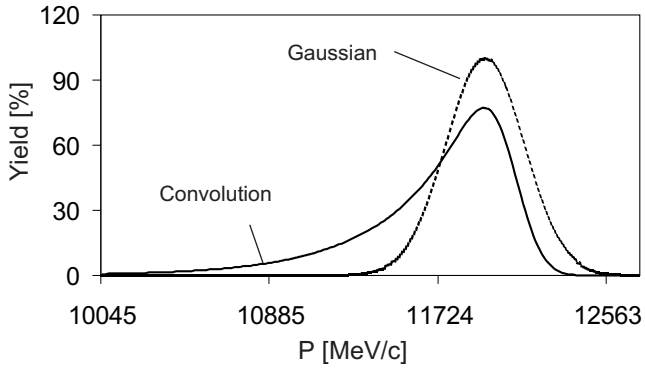

Figure 2.10: *The calculated momentum distribution of ^{31}Mg is a convolution of a Gaussian and an exponential distribution. The calculated ratio of the fragment velocity to the beam velocity is $v_f/v_b = 0.993$. The calculation is performed with the LISE program [75].*

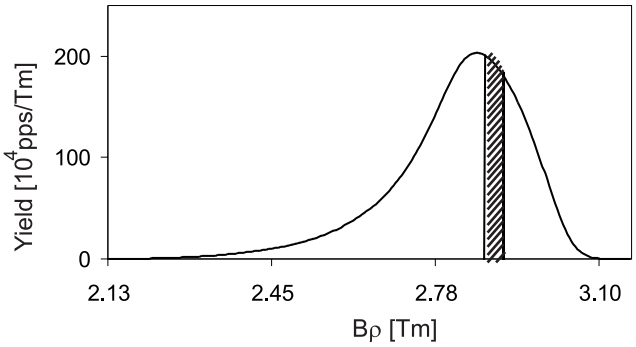

Figure 2.11: *The selection in longitudinal momentum distribution of ^{31}Mg for the settings of the spectrometer. The calculation is performed with the LISE program, [75].*

to the energy loss of the fragment in the detector, and one timing signal. The time of flight (TOF) of the fragment is the difference between this timing signal and the time signal from the RF of the cyclotron. The TOF for a constant length of flight is inversely proportional to the fragment velocity. Since the magnetic rigidity is given $B\rho = \frac{Av}{Zc^2}$, the TOF is proportional to (A/Z).

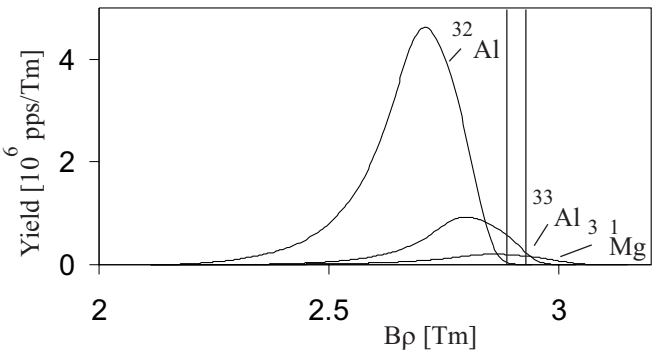

Figure 2.12: *The calculation of Bρ right after the target for the selected fragments, performed with the LISE program [75]. The selection in longitudinal momentum is at the higher energy side of the distribution of* ^{31}Mg*. Therefore a higher purity is obtained since the main contaminants are situated at lower Bρ.*

Based on the Bethe-Bloch formula, giving the energy loss per unit of length by a heavy ion in a silicon detector, we see that the energy deposited in the detector is proportional to Z^2.

$$-\frac{dE}{dx} = \frac{4\pi n Z^2 e^4}{mv^2}\left[\ln\frac{2mv^2}{I(1-(v/c)^2)} - (v/c)^2\right] \tag{2.29}$$

with n the amount of electrons per cm^2, m the mass of the electron, Z the charge of the incoming ion, v the speed of the ion and I the average excitation potential of the atoms in the silicon.
The performance of the (A,Z) separation of the spectrometer is monitored in a two dimensional ΔE-TOF spectrum, firgure 2.13. In this plot, a line of constant TOF (or constant velocity) represents isotopes with the same A/Z ratio, while a line of constant energy loss corresponds roughly to isotopes with the same Z^2.

With a primary beam of $2\mu A$ the silicon detector counts 2400 particles per second. With the settings of the spectrometer, a secondary beam of 95% of ^{31}Mg fragments is obtained. The main contaminants are ^{33}Al (4.5%) and ^{32}Al (0.5%), figure 2.13.

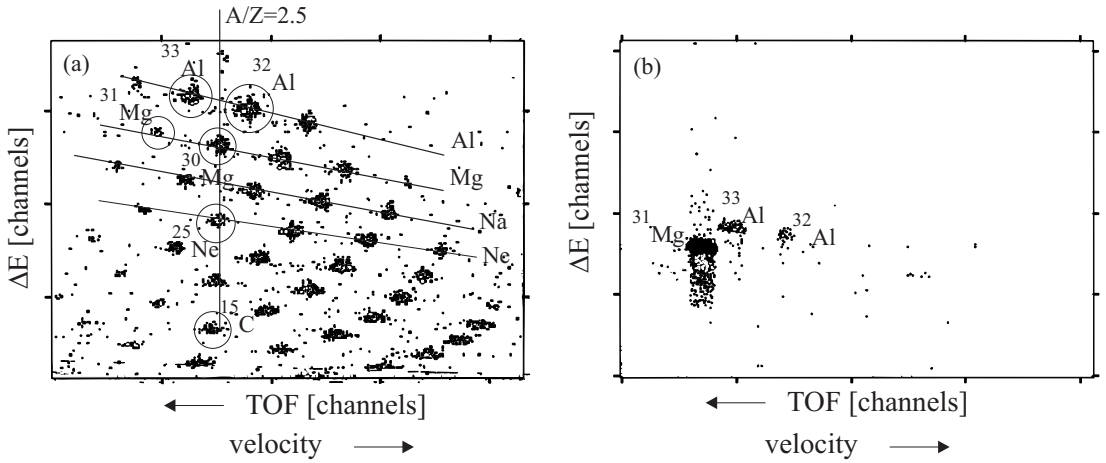

Figure 2.13: *(a) Identification of the fragments in a ΔE- TOF spectrum. (b) The selection made with the LISE spectrometer.*

2.2.4 The β-LMR setup.

When the isotopes enter the LMR measurement chamber, figure 2.14 [76], through a collimator with 20mm diameter, they pass a position sensitive silicon detector of 500μm and an aluminum degrader of 1.5mm thickness before they are stopped into the magnesium single crystal of $2mm$ thickness and purity 99.9%. More than 99% of the ions do not pickup electrons in the different detectors or degrader and are fully stripped when implanted into the crystal [75].

Above and under the crystal two β-telescopes are mounted in the vacuum chamber. One telescope consists of a thin plastic scintillator, a ΔE-detector of 1mm, and a thick trapezium shaped scintillator, a E-detector of 20mm. Every scintillator crystal is glued on a plexiglass light guide which guides the lightpulses to a photomultiplier tube. Scintillator and light guide are wrapped with aluminum foil in order to reflect the outgoing lightpulses back into the detector. The tubes are enclosed in a μ-metal shield to protect them from the stray field of the electromagnet. Photomultiplier and μ-metal are mounted in a weak iron holder, an additional protection against the stray field. When a β-particle hits the scintillator, the photomultiplier emits a time signal and a signal proportional

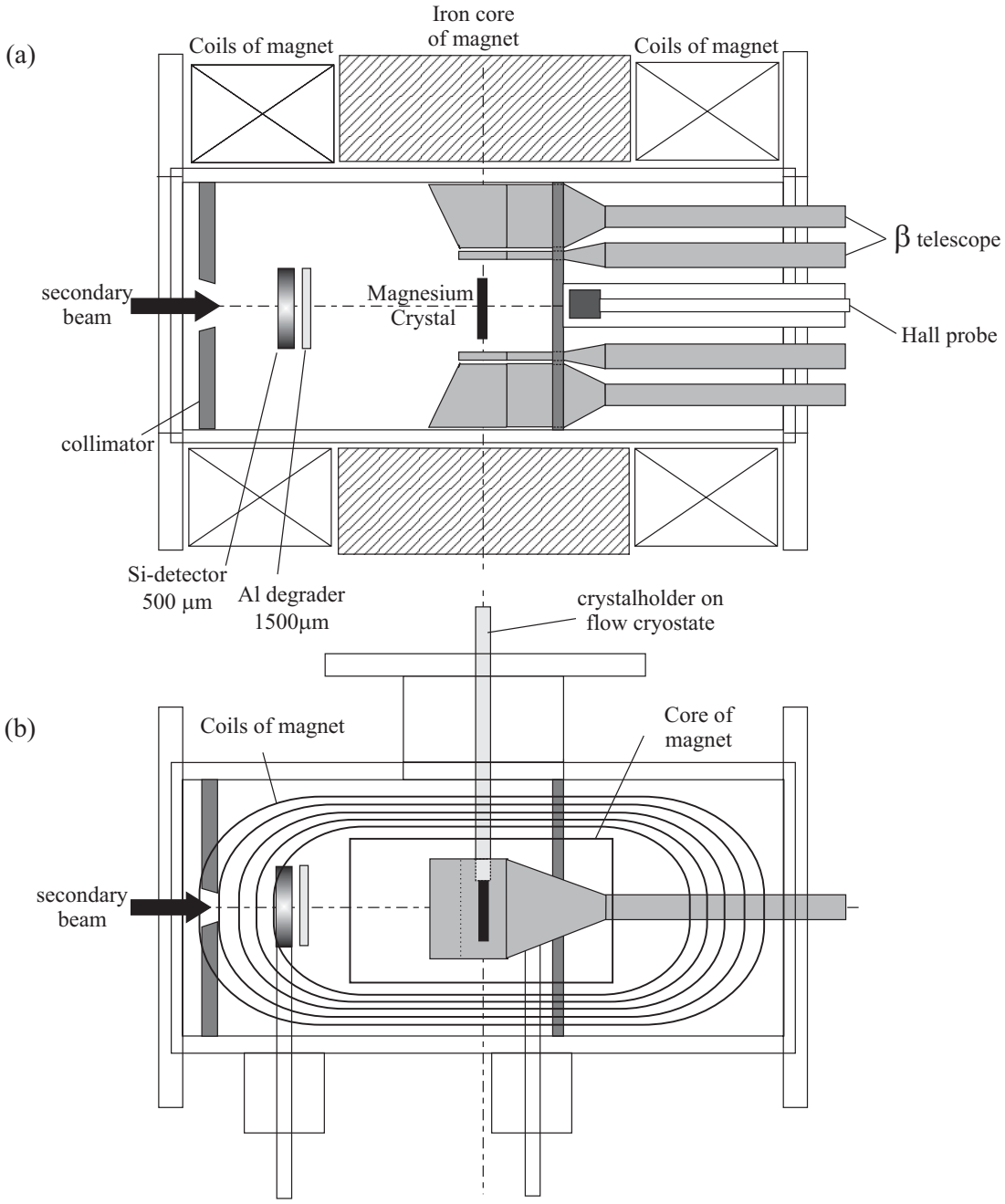

Figure 2.14: *The LMR measurement chamber (a) side view (b) top view.*

to the energy loss of the β in the detector. The ΔE- and E-detector are put in coincidence to eliminate the background radiation. Each telescope covers a spatial angle of 7% of 4π. In the thin ΔE-detector β particles with energy up to

300 keV are stopped, in the thick E-detector β's with energy up to 5 MeV are stopped.

The C-axis of the magnesium single crystal, a hexagonal closed packed (hcp) crystal, is put under an angle $\beta = 17(3)^0$ with respect to a vertical, static magnetic field. This field is induced by two Helmholtz coils with a weak iron core above and under the LMR chamber. The electromagnet has a field range from 0 to 2000 Gauss. Between the two β telescopes a Hall probe is mounted giving a signal proportional to the magnetic field at the position of the probe. Before and after the experiment, the magnetic field at the position of the crystal and at the position of the probe is calibrated.

Since mass and charge of ^{33}Al and ^{32}Al are almost equal to these of ^{31}Mg, it is almost impossible to play with the implantation behaviour of the contaminants in order to purify the isotopes stopped in the crystal, figure 2.15.

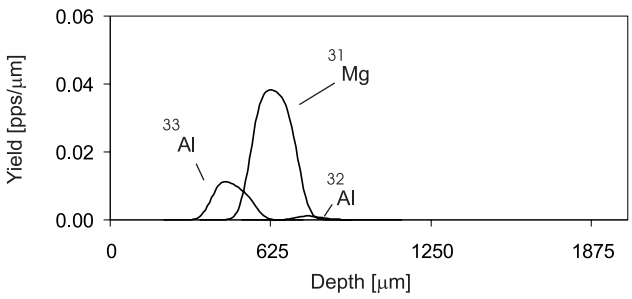

Figure 2.15: *The range distribution of ^{31}Mg, ^{33}Al and ^{32}Al in a magnesium crystal of 2mm calculated with the LISE program [75] assuming a 500μm Si detector and a 1.5mm Al degrader in the beam line.*

Once the isotopes are implanted, they interact with the axial symmetric EFG, $V_{ZZ}(Mg\underline{Mg}) = 6.7(1) * 10^{15} V/cm^2$. This value is obtained from the experimental value for $\nu_Q(^{25}Mg\underline{Mg}) = 324(6)kHz$ at temperature T=4.2K, [77], and $Q(^{25}Mg) = 199(2)mb$ [78].

Nuclei in a metallic crystal couple to the spin magnetic moments of the conduction electrons and therefore lose their initial spin orientation. This magnetic

dipole interaction is the dominant relaxation mechanism in a metal [79, 80, 81]. A lower limit for the magnetic spin lattice relaxation time T_1 is given by the Korringa relation [82, 83]:

$$T\,T_1 = C_K = \frac{1}{K^2\,g^2\,274.9\;10^3} \tag{2.30}$$

with T the lattice temperature, K the Knight shift. With $K(Mg^{25}\underline{Mg})$=0.00112(4) [84] we find $K^2(Mg) = 1.25\,10^{-6}$. The relaxation time is inversely proportional to the temperature T, equation 2.30. Therefore, the crystal holder is mounted on a continuous flow cryostate and is cooled to 4.05(5)K with liquid helium. With the predictions made for the g-factor, table 4.3, one can estimate the relaxation time: $T_1 = 897ms$ for $g = 0.895$ to $T_1 = 1.446sec$ for $g = 0.705$, this is 2 to 4 times the lifetime $\tau = 360(40)ms$ of ^{31}Mg. As a consequence, a reduction of spin-orientation of 50% to 30% is expected.

The temperature is monitored during the experiment by camera.

During 30 minutes data is accumulated for one specific magnetic field value from 0 to 150 Gauss with a continuous implantation of nuclei in the crystal.

2.3 Results on ^{31}Mg.

Data analysis.

The data are collected event by event. One event consists of the time and the energy signal of the two silicon detectors in the beam line, four position signals plus the timing and the energy signal from the silicon detector in the LMR chamber, four energy signals plus the timing between the ΔE and E detector from the four plastic detectors, and a signal coming from the hall probe to monitor the magnetic field.

A signal is accepted as a valid β when the ΔE_{UP} and E_{UP} or the ΔE_{DOWN} and E_{DOWN} are in coincidence. The coincidence condition is put by software. This condition eliminates the background radiation. A signal giving a coincidence in

the up and the down telescopes simultaneously is not accepted, to avoid counts from cosmic muons.

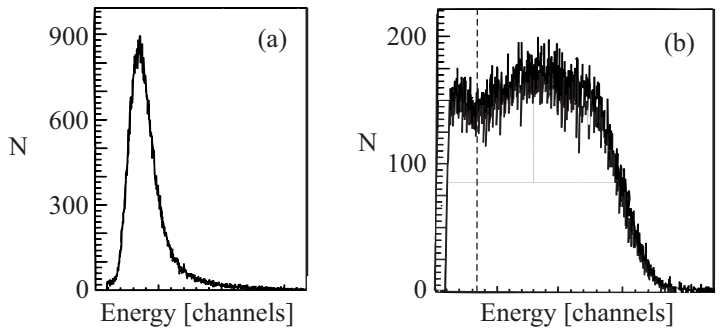

Figure 2.16: *(a) ΔE-spectrum of ^{31}Mg conditioned by a $\Delta E - E$ coincidence. (b) E-spectrum of ^{31}Mg. When β's with the highest energy loss in the E-detector are selected, only those with an energy loss above the dotted mark are taken into account.*

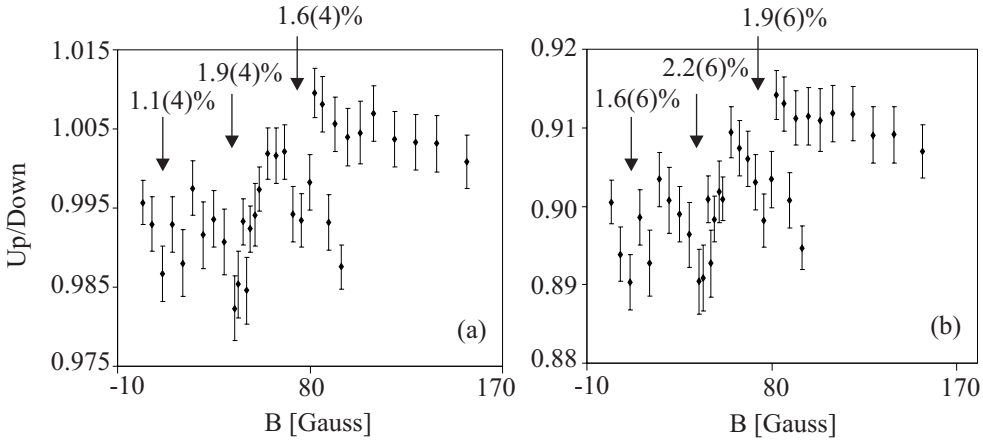

Figure 2.17: *(a) Data when all β's are taken into account. (b) Data when only the β's with the highest energy loss in the E-detector are taken into account.*

β-particles from the mother nucleus ^{31}Mg ($Q_\beta = 11.7MeV$, $t_{1/2} = 230ms$), the daughter nucleus ^{31}Al ($Q_\beta = 8.0MeV$, $t_{1/2} = 644ms$) and the granddaughter nucleus ^{31}Si ($Q_\beta = 1.5MeV$, $t_{1/2} = 157min$) are detected by the telescope. Only β's with 5MeV are stopped in the E-detector. Therefore, the spectrum of the

E-detector is an accumulation of a ΔE-spectrum from the β's going through the detector and a E-spectrum from the stopped β's, figure 2.16. No discrimination between a β from the mother nucleus and from the daughter nucleus can be made by selecting a specific energy loss in the the detector. As a consequence, if only β's with the highest energy loss in the E-detector are selected, the lowest energy β's are neglected and the proportion of the amount of mother nuclei to daughter nuclei changes slightly towards more mother nuclei since 80% of the branching of ^{31}Mg has a higher endpoint energy than those of ^{31}Al, figure 1.121.13.

Figure 2.17 shows firstly that the amplitude from the resonances increases a little, although the difference in amplitude is still in the accuracy interval. This is probably because the daughter nuclei give an almost constant background in the LMR-curve since they have lost most of their orientation before they decay. This orientation loss is a combination of the long time between implantation and the second β decay ($t = 250 + 640ms$), of the high g-factor of ^{31}Al (section 4.3 and therefore a short relaxation time T_1, and of the orientation loss in the first β decay of ^{31}Mg and γ decay in the deexcitation of ^{31}Al.

Secondly, when one compares the amplitudes of the different resonances, they stay in proportion to each other. Therefore, even if the daughter nucleus would have kept some orientation before decay, none of the resonances is created by a LMR of the daughter nucleus.

In the third place, the average asymmetry changes from 0.995 to 0.900. This can be explained by the fact that the amplification of the up and down detectors is a little different from each other and no energy calibration is performed. Therefore, by selecting the specific channel corresponding to the β energy it is possible that in the upper detector more particles are discriminated.

Most of the β's of the granddaughter are stopped in the crystal, the crystal holder and the ΔE-detector, before they reach the E-detector.

For every field value of the static magnetic field, the position of the beamspot is monitored with the position sensitive silicon detector. A change in position of the spot could induce a change in asymmetry because this means a change in opening angle of the up and the down telescope. If the asymmetry change is

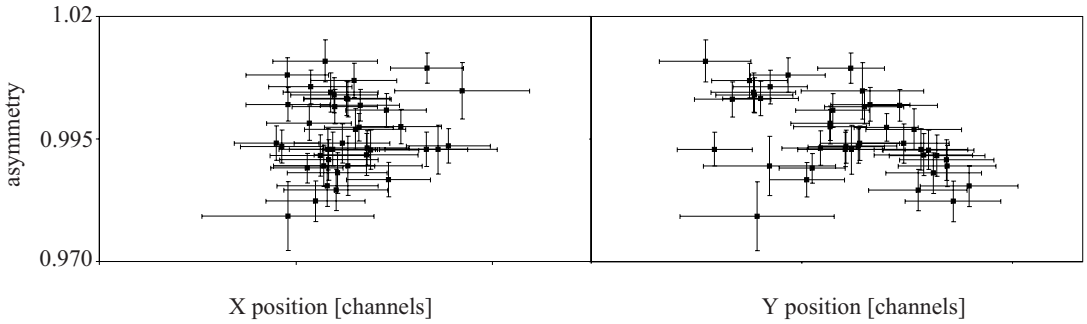

Figure 2.18: *The asymmetry plotted as a function of the horizontal and vertical position of the center of gravity of the beam.*

determined by the change of the implantation position, one expects a continuous increasing or decreasing asymmetry as a function of the implantation position. The asymmetry is plotted as a function of the horizontal and vertical position of the center of gravity of the beam, figure 2.18. Cables of the x and y position are possibly switched before the experiment started. Therefore, it could be that the x position represents the horizontal and y the vertical or vice versa. No correlation is found between the position and the asymmetry.

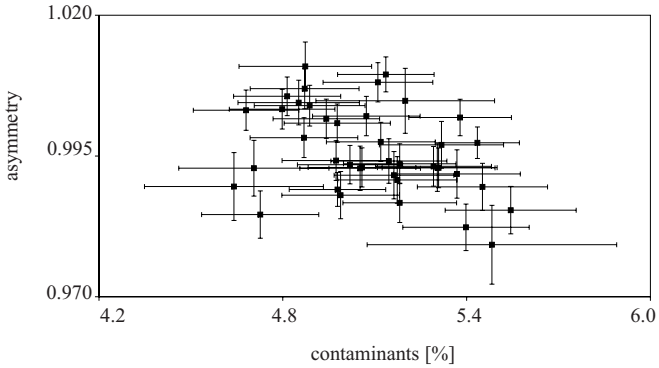

Figure 2.19: *The asymmetry plotted as a function of the amount of contamination.*

The silicon detector in front of the LMR chamber monitors the amount of contamination of the beam. A large increase of the contaminants will induce a decrease of the amplitude of the LMR resonances. Therefore, the asymmetry is

also plotted as a function of the amount of contamination, figure 2.19, and no clear correlation is found.

Since the main contaminants are ^{33}Al ($Q_\beta = 11.99MeV$, $t_{1/2} = 54ms$) and ^{32}Al ($Q_\beta = 13.02MeV$, $t_{1/2} = 33ms$) with Q_β so close to $11.7MeV$, the value of ^{31}Mg, it was impossible to eliminate them by making a specific energy selection of the β particles. But 5% contamination will not influence the results, and can't induce a LMR resonance.

The data fitted with a LMR curve.

From spectroscopy experiments, chapter 1, spin I=3/2 was expected. Figure 2.20(a) gives a simulation of an LMR curve on top of the experimental data for spin aligned ^{31}Mg with spin $I = 3/2$, tilt angle $\beta = 17^0$, radiation parameter $A_1 = -0.3$, $|\nu_Q/\mu| = 100kHz/\mu_N$, $\nu_Q = 0.12$MHz and $\mu = 1.2\mu_N$. The values obtained for the quadrupole and magnetic interaction are close to the predicted values (table 4.3), but one can see that the data points at 30 Gauss or lower, and those around 100 Gauss are far from the LMR curve. Therefore, it is impossible to fit the data.

In an attempt to fit the data around 30 and 100 Gauss better, figure 2.20(b) shows a simulation with $|\nu_Q/\mu| = 120kHz/\mu_N$ but a less realistic quadrupole interaction frequency $\nu_Q = 0.17$MHz and a negative magnetic moment $\mu = -1.4\mu_N$.

In figure 2.20(c) one sees a last attempt for a spin $I = 3/2$ with $|\nu_Q/\mu| = 110kHz/\mu_N$, this time with a combination of spin polarization and spin alignment. Also this simulation is far from good. Although the ratio of the interaction frequencies are close to the predicted value, the quadrupole interaction $\nu_Q = 0.26$MHz and magnetic moment $\mu = 2.3\mu_N$ are not realistic.

Figure 2.21(a) shows the data points with a theoretical LMR curve for ^{31}Mg with spin $I = 5/2$. This picture demonstrates clearly the spin dependence of the distance between two resonances, equation 2.11. The data points around 50 Gauss form one resonance and fix the position of the other resonances. It is clear that

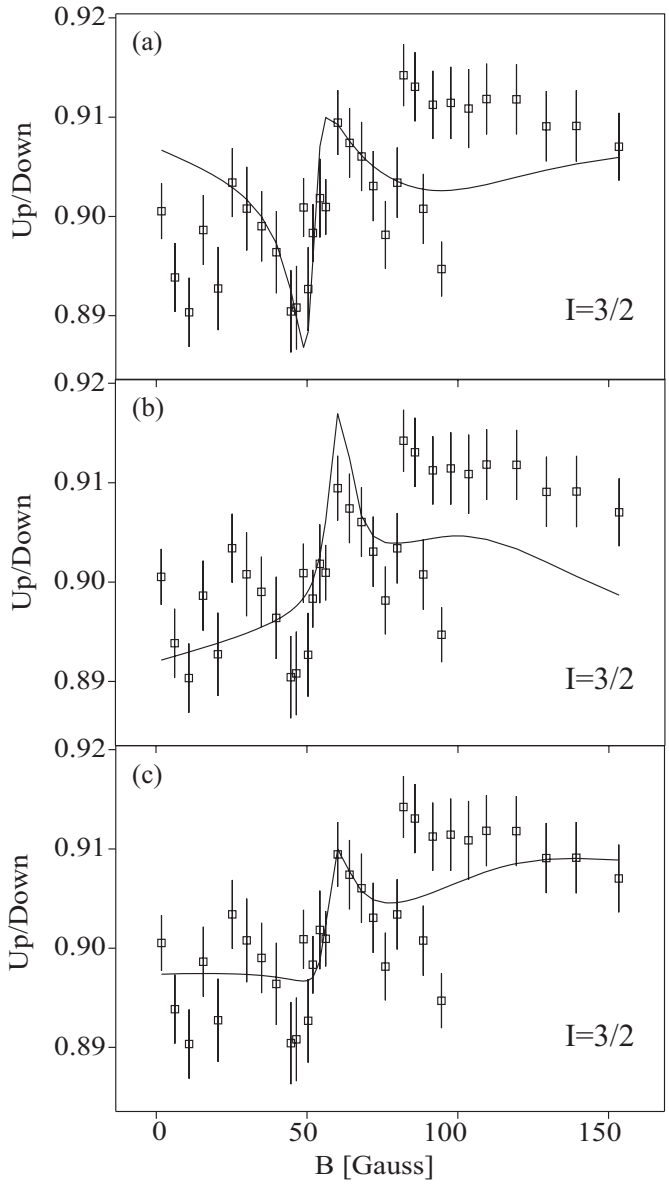

Figure 2.20: *The data points with a simulated LMR curve for* $^{31}MgMg$ *with* $I = 3/2$, $\beta = 17^0$, $A_1 = -0.3$ *(a) for purely spin aligned nuclei with* $\nu_Q = \pm 0.12 MHz$, $\mu = +1.2\mu_N$ *and* $B_2^0 = -0.11$ *(b) for purely spin aligned nuclei with* $\nu_Q = \pm 0.17 MHz$, $\mu = -1.4\mu_N$ *and* $B_2^0 = -0.19$ *(c) for spin aligned and spin polarized nuclei with* $\nu_Q = \pm 0.26 MHz$, $\mu = +2.3\mu_N$, $B_2^0 = +0.04$, $B_1^0 = -0.09$, $\gamma_P = -33^0$ *and* $\varepsilon_P = +90^0$.

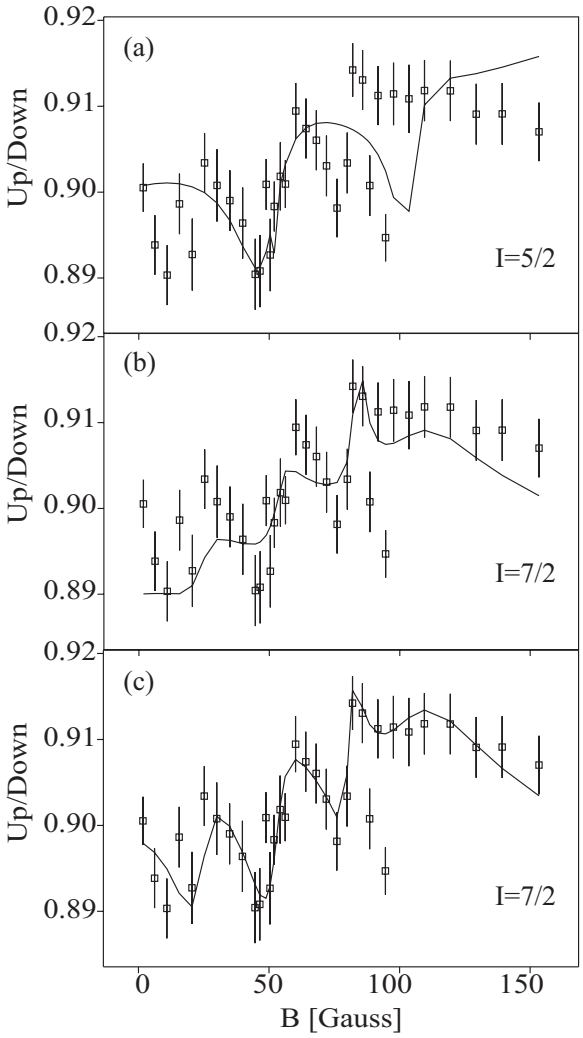

Figure 2.21: *The data points with a LMR curve for* $^{31}MgMg$ *(a) for spin aligned and spin polarized nuclei with* $I = 5/2$, $\beta = 19^0$, $A_1 = -0.3$, $\nu_Q = \pm 0.40 MHz$, $\mu = +2.0\mu_N$, $B_2^0 = -0.26$, $B_1^0 = -0.26$, $\gamma_P = -32^0$ *and* $\varepsilon_P = 0^0$ *(b) for purely spin aligned nuclei with* $I = 7/2$, $\beta = 19^0$, $A_1 = -0.3$, $\nu_Q = \pm 0.41 MHz$, $\mu = -2.5\mu_N$ *and* $B_2^0 = -0.25$ *(c) The best fit with* $\chi^2 = 1.64$ *for spin aligned and spin polarized nuclei with* $I = 7/2$, $A_1 = -0.3$, $\beta = 17(2)^0$, $\nu_Q/\mu = 158.2(2.6) kHz/\mu_N$, $\nu_Q = \pm 0.27\binom{+0.11}{-0.22} MHz$, $\mu = -1.7\binom{-0.7}{+1.4}\mu_N$, $B_2^0 = +0.27(2)$, $B_1^0 = -0.132(14)$, $\gamma_P = -7^0\binom{-15^0}{+30^0}$ *and* $\varepsilon_P = -20.3^0\binom{-3.6^0}{+4.5^0}$.

$I = 5/2$ will never fit the data.

In the simulation for spin aligned ^{31}Mg nuclei with spin $I = 7/2$, figure 2.21(b), the positions of the resonances follow the trend of the data points better for $|\nu_Q/\mu| = 164 kHz/\mu_N$, $\nu_Q = \pm 0.41$MHz, $\mu = -2.5\mu_N$.

The best fit with $\chi^2 = 1.64$ is obtained in figure 2.21(c) for spin aligned and spin polarized nuclei with $I = 7/2$, $A_1 = -0.3$, $\beta = 17(2)^0$ and $|\nu_Q/\mu| = 158.2(2.6) kHz/\mu_N$. With a quadrupole frequency of $\nu_Q = \pm 0.27\binom{+0.11}{-0.22}$MHz and an EFG with $V_{ZZ} = 6.7(1) * 10^{15} V/cm^2$ the quadrupole moment becomes $Q = \pm 170\binom{+70}{-140}$mb. A magnetic moment $\mu = -1.7\binom{-0.7}{+1.4}\mu_N$ gives a g-factor $g = -0.5\binom{-0.2}{+0.4}$. $B_2^0 = +0.27(2)$ and $\gamma_A = -97^0\binom{-15^0}{+30^0}$ is found for the alignment. The polarization is $B_1^0 = -0.132(14)$ with $\gamma_P = -7^0\binom{-15^0}{+30^0}$ and $\varepsilon_P = -20.3^0\binom{-3.6^0}{+4.5^0}$. The accuracy of the fitted values is within 10% of χ^2. Remark that because a variation on γ_A and γ_P influences only the shape of the resonances, the accuracy of the moments is lousy. But the ratio $|\nu_Q/\mu|$, deduced from the position of the resonances, is very precise.

With equations 2.4 and 2.5, one can deduce that to obtain the fit the initial alignment is $A = 16\%$ and the initial polarization is $P = 9\%$, assuming the asymmetry parameter $A_1 = -0.3$. With the polarization perpendicular on the reaction plane, the angle between the horizontal and the reaction plane is $\varepsilon_P = -20.3^0\binom{-3.6^0}{+4.5^0}$, figure 2.22.

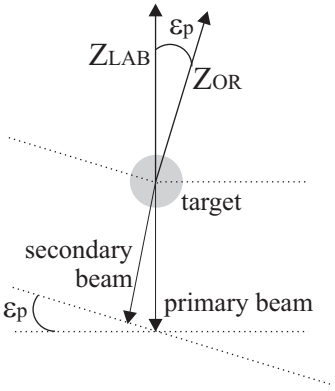

Figure 2.22: *The primary and secondary beam define the reaction plane. The symmetry axis of the polarization Z_{OR} is perpendicular on the reaction plane.*

A simulation of the LMR curve, with the obtained values from the last fit, figure 2.23, shows clearly that data of field values higher than 150 Gauss would give us extra information on the $\Delta m = 1$ resonance. They would proof that the baseline is at around 0.89 and that it is only reached at 300 Gauss. This would confirm the high spin.

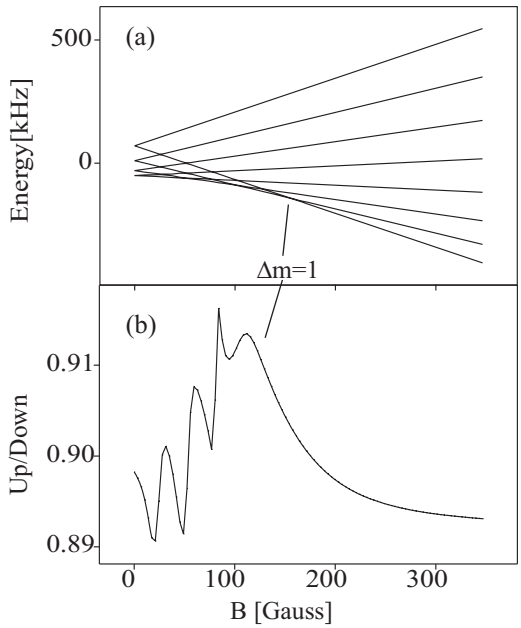

Figure 2.23: *(a) Breit-Rabi plot for ^{31}Mg with spin $I = 7/2$, $\beta = 0^0$ and $|\nu_Q/\mu| = 160kHz/\mu_N$ (b) Simulation of the LMR curve for the spin aligned and spin polarized magnesium isotopes with $\beta = 17^0$.*

2.4 Experimental setup and results for ^{29}Mg.

2.4.1 Experimental setup.

Also the ^{29}Mg isotopes are produced at GANIL. The same primary beam on a rotating ^{9}Be target of $1324\mu m$ is used. The isotope selection is performed with the first dipole at $B\rho_1 = 2.8634Tm$ and $B\rho_2 = 2.6665Tm$, with the momentum

acceptance of the spectrometer $\Delta p/p = 0.23\%$. The spectrometer selects the longitudinal momentum as in figure 2.24.

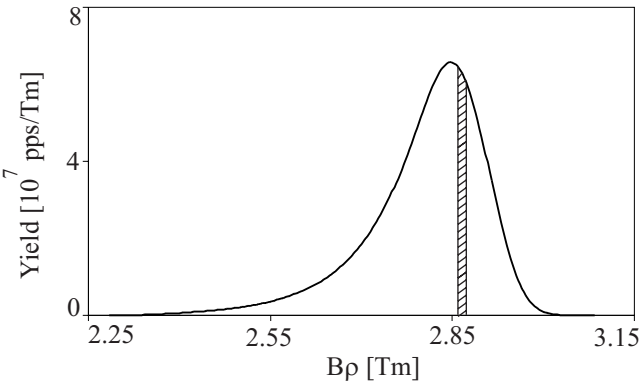

Figure 2.24: *The selection in longitudinal momentum distribution of ^{29}Mg for the settings of the spectrometer. The calculation is performed with the LISE program and $v_f/v_b = 0.993$, [75, 74].*

To obtain a better purification of the beam the spectrometer is used in combination with a velocity filter (LISEIII). This velocity filter or Wien filter in front of the LMR measurement chamber, figure 2.7, consists of a vertical electric field $\vec{E}$ perpendicular on a horizontal magnetic field $\vec{B}$. A selection of the isotopes is made according to $\vec{E} = -\vec{v} \times \vec{B}$ [85]. Only isotopes with velocity $|v| = |\frac{E}{B}|$ pass the filter. With B=204.7G and E=2252.5kV/m a 98% pure beam is obtained with ^{30}Al as the main contaminant. With a primary beam of $2\mu A$ the silicon detector in front of the LMR chamber counts 5000 particles per second.
The same detector setup is used as in the ^{31}Mg case.
The magnesium single crystal is cooled to 4.25(25)K. Since at this temperature the relaxation time, equation 2.30, is expected to be of the same order as the lifetime ($t_{1/2} = 1.3sec$, $T_1 = 1.7(1)sec$) the beam is bunched with 1.5sec beam on and 3.5sec beam off in order to let the relaxed isotopes decay before newly oriented are implanted.
Data is accumulated during 40 minutes for one specific field value from 0 to 150 Gauss.

2.4.2 Results on ^{29}Mg.

For every event two extra signals are stored: a signal drawing distinction between beam-on and beam-off, and a clock signal. At every start of the beam-on period, the clock is reset to zero.

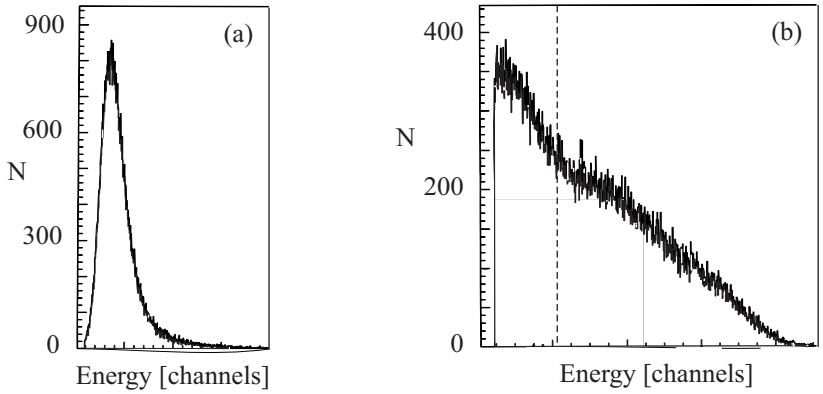

Figure 2.25: *(a) ΔE-spectrum of ^{29}Mg. (b) E-spectrum of ^{29}Mg. When β's with the highest energy loss are selected, only those with an energy loss above the dotted mark are taken into account.*

β-particles from the mother nucleus ^{29}Mg ($Q_\beta = 7.55MeV$, $t_{1/2} = 1.30sec$) and the daughter nucleus ^{29}Al ($Q_\beta = 3.68MeV$, $t_{1/2} = 6.56min$) are detected. Only the data during beam-on period are taken into account by software. Similar as in the ^{31}Mg case, when only β's with the highest energy loss in the E-detector are selected, figure 2.25, the β's from the daughter nucleus are discriminated and the resonances slightly deeper.
Since we have only 2% contamination, mostly ^{30}Al ($Q_\beta = 8.56MeV$, $t_{1/2} = 3.60sec$), it will hardly influence the results.
As in the case for ^{31}Mg, the asymmetry is plotted as a function of the horizontal and the vertical position of the beam, and as a function of the contaminants and no correlation is found.

Figure 2.26 shows the best fit with $\chi^2 = 0.88$ and is obtained for spin aligned nuclei with $I = 3/2$. From the asymmetry parameter of the different β branches

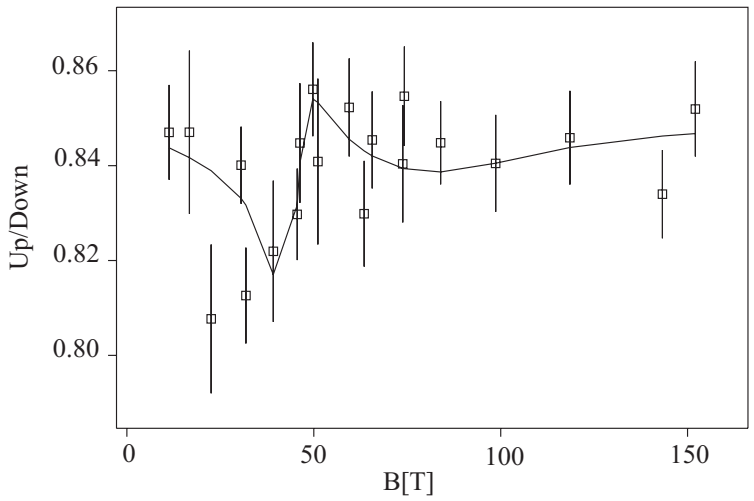

Figure 2.26: *The data of ^{29}MgMg fitted with a LMR curve:* $\chi^2 = 0.88$ *for spin aligned nuclei with* $I = 3/2$, $A_1 = -0.3$, $\beta = 17^0$ *and fitted values* $\nu_Q/\mu = 87.8(1.5)kHz/\mu_N$, $\nu_Q = \pm 0.110(35)MHz$, $\mu = 1.24(24)\mu_N$, $B_2^0 = +0.22(7)$.

the total asymmetry can be calculated. The asymmetry parameter for the full β spectrum, figure 1.9, consists of 61% $A_1(3/2 \rightarrow 5/2) = -\sqrt{I/3(I+1)} = -0.45$, of 10% $A_1(3/2 \rightarrow 1/2) = \sqrt{(I+1)/3I} = 0.75$ and of 29% $A_1(3/2 \rightarrow 3/2) = 1/\sqrt{3I(I+1)} = 0.30$, which makes in total $A_1 = -0.11$. Since only the highest energy β particles are selected, the main contributing branch will be the one from ground state to ground state and the branches with the larger end-point energies. Therefore, the asymmetry parameter can be estimated as $A_1 = -0.3$. As explained in section 2.1, the width of the resonances is given by this mis-alignment angle between the EFG and the magnetic field. This angle $\beta = 17^0$ is fixed on the basis of the fit of ^{31}MgMg where the width of the resonances is clearly well reproduced, figure 2.21. The ratio of the quadrupole frequency to the magnetic moment is $|\nu_Q/\mu| = 87.8(1.5)kHz/\mu_N$. A quadrupole frequency of $\nu_Q = \pm 0.110(35)$MHz with EFG $V_{ZZ} = 6.7(1) * 10^{15} V/cm^2$ gives the quadrupole moment $Q = \pm 69(22)$mb. The fitted magnetic moment $\mu = 1.24(40)\mu_N$ gives a g-factor $g = 0.83(27)$. $B_2^0 = +0.22(7)$ and $\gamma_A = 0^0(19^0)$ is found for the alignment. The accuracy of the fitted values is within 10% of χ^2.

Chapter 3

β-NMR on ^{27}Na, ^{31}Al and ^{31}Mg.

3.1 Nuclear magnetic resonances at a fragment separator.

The Nuclear Magnetic Resonance (NMR) method on β decaying nuclei is a technique used to measure the g-factor of ground state nuclei. To perform a NMR experiment the nuclei have to be spin polarized. This initial orientation is destroyed by a RF frequency.
In this section the production of the orientation will be explained. And since the NMR method is a well known technique, it will only be described with special attention to the similarities with the LMR method.

3.1.1 Polarization in fragmentation reactions.

As mentioned in section 2.1.1 the ensemble of nuclei is spin polarized when the probability to have the spins along the symmetry axis is different for opposite directions $p(m) \neq p(-m)$ and the amount of initial polarization can be calculated with equation 2.5.
There are several methods to orient nuclei, such as low temperature nuclear orientation (LTNO), optical pumping, tilted foil, or polarization induced by an

oriented beam of protons or neutrons. The different orientation methods are strongly linked with the production method and lifetime of the studied isotope. To perform LTNO, the probe has to be immersed in a very high hyperfine field of a ferromagnetic host. This field is far too low for nuclei with $Z \leq 20$ like magnesium. Tilted foil requires a certain interaction time of the atom with the foils. The atoms have to be produced at low energy and only a few percent of polarization can be reached. Optical pumping is optimal for specific nuclei as the alkali and alkaline earth metals, for which the atomic excitations can be reached by the frequency of the available lasers. The beam must have a very small energy resolution so that the laser excitation is applicable to all the nuclei. Therefore the atoms have to be produced at low energy or have to be cooled. It is very good orientation method when coupled to an ISOL beam (CERN-ISOLDE, Collaps). When the isotopes are produced in an ISOL system and ionized in the laser ion source, the orientation can also be induced by a two step resonant ionisation with polarized laser light, a technique still under development. In tilted foil, optical pumping and two step laser ionisation and polarization, the atomic polarization will be converted to a net nuclear polarization. Polarization induced by an oriented beam of neutrons is used for production and polarization of isotopes with one neutron more than the stable isotope. For exotic neutron rich nuclei far from the line of stability, production by neutron capture would require a too dense neutron flux.

When the described experiment was initiated, the ^{31}Mg isotopes were best produced via projectile fragmentation intermediate energies. Therefore, the orientation obtained in the production mechanism itself is the most straightforward way to orient these isotopes. Since the light isotopes are fully stripped, the orientation is conserved during the flight time to the implantation crystal.

The momentum distribution of fragments observed in a projectile fragmentation reaction shows a width, which arises from the internal motion of the removed nucleons of the projectile nucleus in case of a ultra thin target and a very small energy spread of the projectiles, equation 2.28. Consequently the intrinsic momentum of the removed nucleon is correlated with the fragment momentum. If

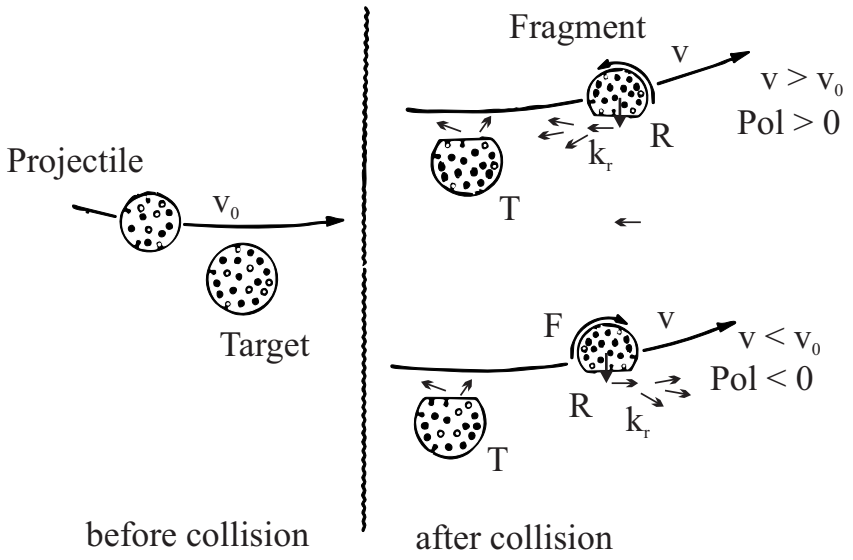

Figure 3.1: *Predicted correlation between the fragment spin and longitudinal momentum in the participant spectator model for a near-side trajectory, [86]. A projectile at a velocity $\vec{v}_0$ is converted to a fragment through removal of nucleons at the position $\vec{R}$ with linear momentum $\vec{k}_r$.*

the removal or abrasion takes place from a localized volume of the projectile, the fragment angular momentum is also correlated with its longitudinal momentum, [87, 86] and figure 3.1. Since the selection of the longitudinal momentum can be handled in the standard scheme of fragment separation, section 2.2.2, the correlation between the longitudinal and angular momentum serves for the selection of the fragment angular momentum.

Let us consider a peripheral collision of a projectile nucleus with a target in which the nucleons in the overlapping volume are removed from the projectile and the resulting nucleus is observed as an outgoing fragment. The essential feature of the process is that the fragment part remains as a spectator, an assumption that holds for high energy only ($\sim 100 MeV/u$). From the conservation laws of linear and angular momentum, since in the participant-spectator model no transfer of momentum between the target and projectile is assumed, one can see the correlation of the longitudinal momentum $\vec{p}_f$ and the angular momentum $\vec{J}_f$ of the

fragment, figure 3.2:

$$\begin{aligned} \vec{p}_{projectile} &= \vec{p}_{fragment} + \vec{p}_{removed} \\ \Rightarrow \vec{p}_f &= m\vec{v}_0 - \vec{k}_r \end{aligned} \tag{3.1}$$

with m and $\vec{v}_0$ the projectile mass and velocity, $\vec{k}_r$ the linear momentum of the removed portion.

$$\vec{J}_{fragment} = -\vec{R} \times \vec{k}_r \tag{3.2}$$

with $\vec{R}$ the position vector pointing from the fragment to the removed portion. For simplicity one assumes zero spin of the projectile and ignores the intrinsic spins of the removed nucleons [88].

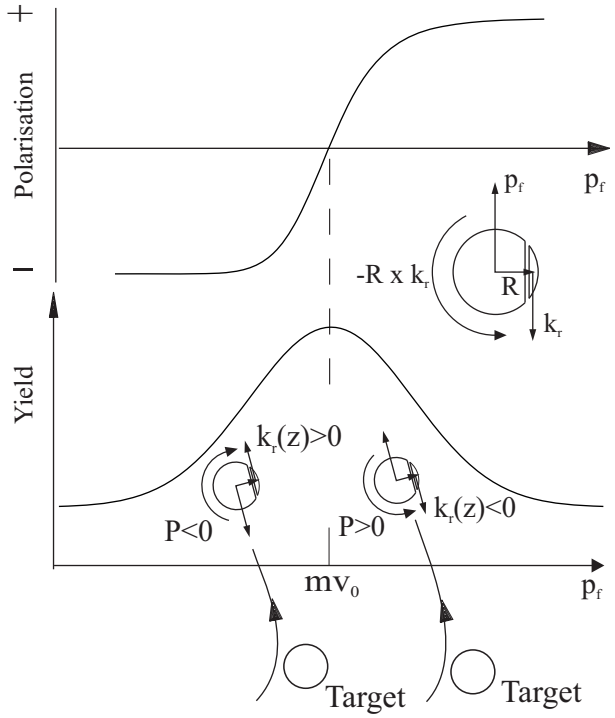

Figure 3.2: *Schematic diagram of the correlation between the polarization P and the longitudinal momentum of the fragment p_f and of the removed portion k_r, for a near-side trajectory [89].*

Thus processes associated with $\vec{k}_r$ parallel to the beam direction, $\vec{k}_r(z) > 0$, should correspond to events of lower $\vec{p}_f$ side and favor negative polarization,

$P < 0$. While those associated with $\vec{k}_r(z) < 0$ lead to events of high $\vec{p}_f$ and $P > 0$. The magnitude of polarization is expected to be the same for low and high momentum sides, while a slight reduction is observed for the low momenta [88]. This indicates that other reaction processes like transfer reactions (see section 2.2.2) may also contribute to the low momentum region but not to the orientation or in opposite way.

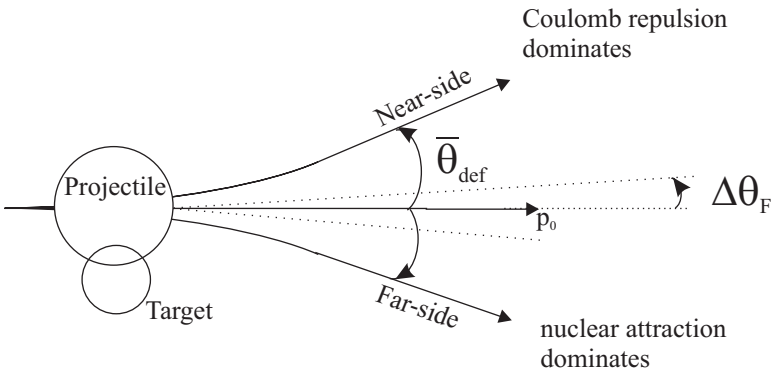

Figure 3.3: *The near-side and far-side trajectory.*

In the above argument the scattering is assumed to proceed along near-side trajectories. The reversed relation of the sign of polarization versus $\vec{p}_f$ is expected if far-side trajectories are occuring, figure 3.3.

A criterion for the dominance of near-side trajectories may be obtained by a condition that the repulsive Coulomb deflection should be larger than the nuclear attraction [87]. This condition may be expressed in terms of the mean deflection angle as $\overline{\theta}_{def}$ which can be calculated classically with the Coulomb and nucleus-nucleus potentials. $R = \overline{\theta}_{def}/\Delta\theta_F$ provides a measure of the competition between the near- and the far-side collisions. The parameter $\Delta\theta_F$ represents the spread of the deflection angle due to the Fermi motion of the projectile nucleons with $\Delta\theta_F = \sigma_t/p_0$ (> 0) and σ_t the dispersion of the transverse momentum and p_0 the projectile momentum. $R \gg 1$ $(R \ll 1)$ represents collisions dominated by the near-side (far-side) trajectory, whereas $R \sim 0$ implies a strong mixing of the two contributions. To obtain a net polarization the projectiles must be selected at an angle θ_L, usually set larger than $\overline{\theta}_{def}$. A gradual change is observed from

near-side to far-side with decreasing target Z number and increasing beam energy [89].

Typical values are $\Delta\theta_F \sim 1^0$ and $R \sim 5$ for a primary beam with $\sim 50 MeV/u$ to $R \sim 0.5$ for a primary beam with $100 MeV/u$ when a 2 to 3 nucleons are abraded. For a selection at the extremes of the momentum distribution up to 20% of polarization can be reached, but usually it is considerably less.

When high beam energies are used, the deflection angle $\overline{\theta}_{def}$ becomes very small, therefore R becomes small and no large polarization can be expected. Moreover, the selection of the fragments at an angle θ_L with respect to the primary beam is difficult if an appreciable counting rate is desired.

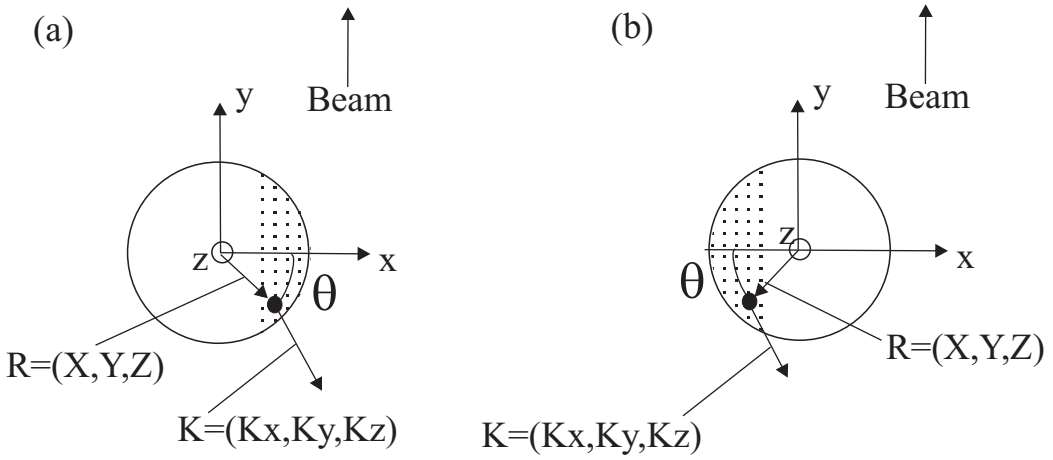

Figure 3.4: *A projectile turns into a fragment through removal of nucleons at the position R (a)for the near-side trajectory (b)for the far-side trajectory. The removed portion has a linear momentum K at the moment of impact. The removal takes place uniformly over the overlap region of projectile and target. [87]*

In the model described above the fragment is a spectator as if no momentum transfer between the fragment and the target nucleus occurs. The model involves that the yield weighted average of the polarization should be zero and that the zero-crossing of the polarization should occur at p_0 independently of the competition of the near- and the far-side collision which is not observed experimentally [87]. Therefore the model is modified. The removed portion, figure 3.4, of the

projectile has an angular momentum $R \times K$ with $R = (X, Y, Z)$ the position and $K = (K_x, K_y, K_z)$ the momentum of the removed nucleon or cluster of nucleons at the instant of removal. The z-component l_z of the angular momentum l left in the fragment after the abrasion is then $l_z = -XK_y + YK_x$. If one assumes that the nucleon removal takes place uniformly over the overlap region, one obtains $< X > \sim R_0$ and $< Y > \sim 0$, with R_0 the radius of the projectile. This assumption was taken in the preceding model, leading to the prediction for the zero crossing of the polarization to occur at p_0, where the highest production yield is obtained. Alternatively, one can consider $< Y > \neq 0$ so that l_z remains non-vanishing even at p_0. Assuming that the average location $(< X >, < Y >)$ is given as $(R_0 \cos\theta, R_0 \sin\theta)$ with $\theta \leq 0$ or $< Y > \leq 0$, is compatible with the zero-crossing of the polarization to occur at higher (lower) momentum than p_0 for the near-side (far-side) trajectory.

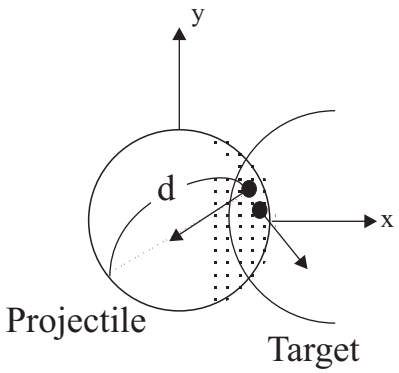

Figure 3.5: *Nucleons of the overlap region between target and projectile traverse the prefragment over a path length d. [87]*

The negative value of $< Y >$ can be understood if one considers the nucleon rescattering through the fragment, figure 3.5. Projectile nucleons hit by the target nucleons traverse the remaining portion of the projectile or prefragment in a backward (negative Y) direction. In such a process the nucleons will rescatter on those in the prefragment, which eventually evaporates some nucleons. The survival probability of the fragment should increase as Y decreases, resulting in a weighted average of $Y \leq 0$.

The polarization around p_0 can be useful because it allows a momentum selection of the isotopes which simultaneously optimizes P and intensity.
The polarization mechanism is also valid for *heavy* isotopes (typically $A > 50$) produced with projectile fragmentation reactions. However, the energies used are usually not high enough to produce them fully stripped, consequently the orientation of the nuclear spin will be destroyed due to the random interaction of the atomic spin with the magnetic elements of the beam transport and separating system. On the other hand, atomic ions with a charge state corresponding to magic atomic numbers have an atomic spin $J = 0$ in their ground state and no interaction with the magnetic environment of the beam optics occurs. This results in a partial preservation of the nuclear orientation

3.1.2 The NMR formalism.

The Nuclear Magnetic Resonance (NMR) method on β decaying nuclei is a well understood technique to measure the g-factor of ground state nuclei [83, 90]. The spin polarized nuclei are implanted in a cubic single crystal, this is a crystal without an EFG. The system is immersed in a static magnetic field B parallel to the orientation axis to preserve the spin orientation of the ensemble and to induce the Zeeman splitting of the nuclear hyperfine levels. Perpendicular to B, in the direction of the beam line, a linearly polarized oscillating magnetic field, with amplitude $2B_1$ and frequency ω_{RF}, is added:

$$RF = 2B_1 \cos(\omega_{RF} t)\vec{e}_{X_{LAB}} \tag{3.3}$$

The oscillating magnetic field is composed of a right and a left circularly polarized component. Only the component rotating with the same sense as the nuclear Larmor precession ω_B can induce a resonance. The sign of the frequency is therefore defined by $\omega_{RF} = -\frac{g}{|g|}|\omega_{RF}|$.
The time dependent Hamiltonian of this system in the LAB-frame (figure 2.3) is:

$$H_{NMR} = \omega_B I_Z + \omega_1[\cos\theta(t) I_X + \sin\theta(t) I_Y] \tag{3.4}$$

with $\omega_B = -\frac{g\mu_N B}{\hbar}$, as in equation 2.8, $\omega_1 = -\frac{g\mu_N B_1}{\hbar}$ and $\theta(t) = \omega_{RF}t + \Delta$. The phase Δ is the phase of the RF field at $t = 0$, the instant of implantation of the nucleus in the crystal.

After a unitary transformation to a rotating axis system ($X'Y'Z'$) with the same frequency as the RF field, the Hamiltonian becomes time independent: [90]

$$H'_{NMR} = [\omega_B - \omega_{RF}]I_{Z'} + \omega_1 I_{X'} \tag{3.5}$$

The non-axial term inducing the mixing of different $|m>$ states is proportional to B_1, typically 1 to 10 Gauss. When compared to LMR, equation 2.8 where the mixing is proportional to $B\sin\beta$, one can see that the mixing for a LMR is easily stronger since the static field B is of the order of 100 to 1000 Gauss and β can be chosen large (up to $15 - 20^0$).

As in the LMR, it is possible to make a Breit-Rabi diagram in the rotating frame showing the energy of the different $|m>$ states as a function of the static magnetic field B. The mixing of the population of the levels will be induced when two (or more) $|m>$ states are crossing, this is when $\omega_B = \omega_{RF}$ or when

$$\nu_{RF} = \frac{g\mu_N B}{\hbar} \tag{3.6}$$

In fact, at the level crossing all levels are degenerate. A mixing will make all the levels equally populated, and the β-emission will become isotropic. This is why a spin aligned ensemble is not sufficient, since a change in alignment can not be detected in the β asymmetry.

It can also be understood as following. When $\omega_B = \omega_{RF}$, equation 3.5 becomes $H'_{NMR} = \omega_1 I_{X'}$. The spins of the nuclei will precess around $I_{X'}$ and the nuclear orientation will be destroyed.

Similarly, the perturbation factors can be calculated as for the LMR with the perturbation matrix element:

$$W_{mm'}^{\Delta m} \sim \frac{\hbar\omega_1}{\Delta m} \tag{3.7}$$

This demonstrate that the width of the resonance increases with increasing B_1 also called power broadening. Before this perturbation can be implemented in

the angular distribution (equation 2.15), the perturbation factors have to be transformed back to the LAB-system.

The nuclear states are produced continuously, without any time relation to the RF field. Therefore all phase angles Δ are equally probable. The corresponding perturbation coefficients must be integrated over the phase angle.

The orientation axis is vertical, perpendicular on the horizontal reaction plane. The OR-frame coincides with the LAB-frame and no transformations on the orientation tensors have to be performed.

The angular distribution (equation 2.15), comes down to

$$W(\theta,\tau)_{LAB} = 1 + A_1 B_1^0(I,\tau)_{LAB}\cos(\theta) \tag{3.8}$$

For equidistant splittings caused by a static magnetic field, the perturbation coefficients $G_{kk'}^{nn'}(t)$ are independent of the spin I of the nuclear states and one can proof that terms with $k \neq k'$ vanish, [90]. Integration over all phase angles Δ leaves only terms with $n \neq n'$ and equation 2.17 reduces to:

$$B_0^1(I,\tau)_{LAB} = G_{00}^{11}(\omega_B,\tau)_{LAB}\, B_0^1(I,t=0)_{LAB=OR} \tag{3.9}$$

$$B_0^1(I,t=0)_{OR} = -\sqrt{\frac{3I}{I+1}}\,P(t=0) \tag{3.10}$$

In the resonance condition, all levels are equally populated and the perturbation coefficient is $G_{00}^{11}(\omega_B = \omega_{RF},\tau) = 0$. The angular distribution is isotropic. Taking the efficiency of the two β telescopes into account the observed asymmetry is

$$R_{IN} = \frac{W(0^0,\tau)}{W(180^0,\tau)}(\omega_B = \omega_{RF}) = \frac{\epsilon_{UP}}{\epsilon_{DOWN}} \tag{3.11}$$

Far from the resonance condition, the RF perturbation is too small to induce a change in orientation and therefore is $G_{00}^{11}(\omega_B \neq \omega_{RF},\tau) = 1$ or

$$R_{OUT} = \frac{W(0^0,\tau)}{W(180^0,\tau)}(\omega_B \neq \omega_{RF}) \approx \frac{\epsilon_{UP}}{\epsilon_{DOWN}}(1 + 2A_1\sqrt{\frac{3I}{I+1}}P(t=0)) \tag{3.12}$$

When the asymmetry is normalized to the asymmetry obtained when no RF frequency is applied, knowing that $R_{RFoff} = R_{OUT}$, one obtains

$$\frac{R_{IN}}{R_{RFoff}} \approx 1 - 2A_1\sqrt{\frac{3I}{I+1}}P(t=0) \tag{3.13}$$

$$\frac{R_{OUT}}{R_{RFoff}} = 1 \tag{3.14}$$

and the amount of polarization can be obtained directly from the amplitude of the resonance.

3.2 Experimental setup.

The setup for the nuclear magnetic resonance is very similar to the one of the LMR as discussed in section 2.2. This section will focus only on the specific details different from the setup described above, especially the way how a broad region of g-factors can be scanned with only a few measurements by changing the magnetic field and keeping the RF frequency with a broad modulation constant.

3.2.1 Selection of the fragment.

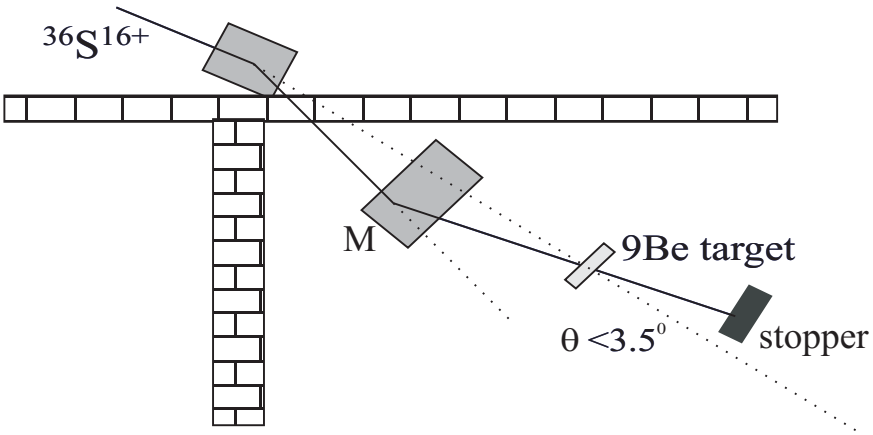

Figure 3.6: *Schematic drawing of the deviation of the primary beam by the movable magnet M in front of the LISE target.*

In order to obtain a net polarization (section 3.1.1), the primary beam of $^{36}S^{16+}$ is deviated by a movable magnet in front of the rotating ^{9}Be target, figure 3.6. A maximum deflection angle of 3.5^0 can be reached at LISE and can not be set smaller than 1^0 as the heavy stopper for the primary beam would hinder the free passage of the secondary beam.

This system was designed to avoid contamination of the different charge states of the primary beam in the selected secondary beam [72]. Light projectiles at intermediate energy are fully stripped after their way through the target. However the charge of heavier elements can have a large distribution according to their nature, energy and thickness of the target. The different charge states are transported by the spectrometer together with the studied isotopes. By stopping the primary beam, the secondary beam is purified without loosing too much in counting rate (a factor 2 to 3) due to the rather small acceptance of LISE compared to the angular distribution of the fragments.

The primary beam is deviated with an angle of 2^0 for the selection of the ^{27}Na, ^{31}Al and ^{31}Mg fragments.

To purify the secondary fragment beam, a last selection can be made by the Wien filter, additional to the selection by the LISE spectrometer, figure 2.7 and section 2.2.1. The beam passes through an electric field $\vec{E}_{Wien}$ perpendicular to a magnetic field $\vec{B}_{Wien}$. The direction of the electric field is vertical, consequently the direction of the magnetic field is horizontal and their intensities are chosen so that the selected ion can pass this filter without being decelerated nor deviated from the initial path. The forces induced by the two fields are compensated:

$$q(\vec{v} \times \vec{B}_{Wien}) = \vec{F}_B = -\vec{F}_E = -q\vec{E}_{Wien} \tag{3.15}$$

This velocity filter is used for the experiment on ^{31}Al. It induces an additional rotation of the polarization axis around the horizontal magnetic field $\vec{B}_{Wien}$. This will reduce the measured asymmetry.

3.2.2 The β-NMR setup.

Detection and identification is performed in a similar way as for the LMR experiment, section 2.2.3. The same measurement chamber as shown in figure 2.14 is used. The polarized ^{27}Na are implanted in a NaCl single crystal, the ^{31}Al and ^{31}Mg in a MgO single crystal. Both the crystals are cubic and insulators. Since no random interaction with conduction electrons is possible, the relaxation of

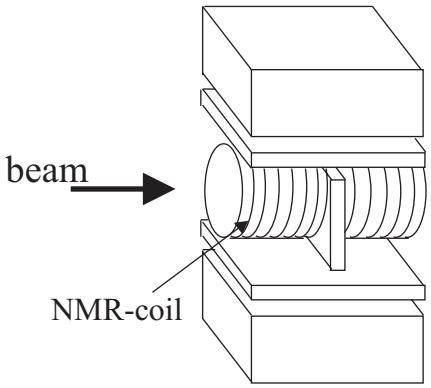

Figure 3.7: *The NMR coil is mounted between the two β telescopes on top of the cubic crystal and with the linearly polarized field in the direction of the beam.*

the orientation is expected to be much longer than the lifetime of the isotopes and cooling is not necessary [79, 80, 81]. Around the crystal, a coil is installed inducing the linearly polarized oscillating magnetic field in the direction of the beam, figure 3.7.

To overcome the inhomogeneous linewidth as a result of defects in the lattice or due to the inhomogeneity of the static magnetic field, a modulation with amplitude $\Delta\nu_{RF}$ and frequency ν_{mod} is applied on the central frequency $\nu_{RF} = \omega_{RF}/2\pi$. The shape of the modulation is triangular, in order to spread the power equally over the whole frequency band, figure 3.8. The same amplitude of the resonance can be expected if the resonance would occur in the middle of the modulation interval (figure 3.8(a)), or at the extreme of the modulation interval (figure 3.8(b)). This would not be the case if for example a sinusoidal shape would have been used.

The amplitude B_1 of the RF frequency is monitored by a pick-up antenna in the back of the crystal. The tension S induced in this antenna is proportional to the field strength in the coil:

$$B_1 = \frac{S}{2\pi\nu_{RF}NA} \tag{3.16}$$

with N the amount of windings with radius r, and $A = \pi r^2$ the surface enclosed by the windings.

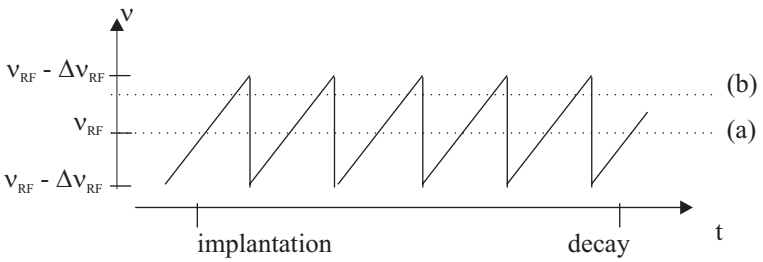

Figure 3.8: *Schematic view of the frequency modulation with a triangular shape. The power of the RF frequency is equally spread over the full frequency band and therefore the same amplitude of the resonance can be expected if (a) the resonance would occur in the middle of the modulation interval, or (b) at the extreme of the modulation interval.*

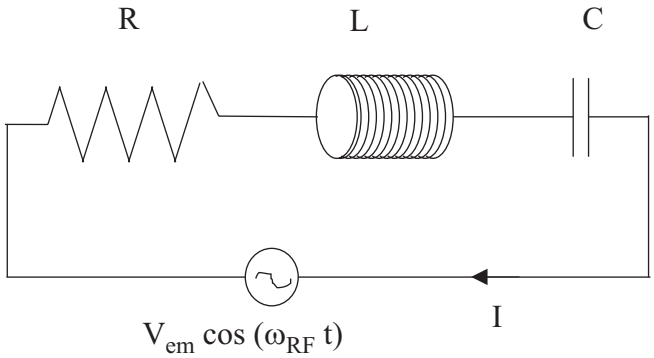

Figure 3.9: *Schematic drawing of an RLC-circuit which consists of a resistance R [Ω], a inductance L [H] and a capacitance C [F].*

The RF coil connected with a synthesizer providing an electromagnetic tension V_{em} with pulsation $\cos(\omega_{RF}t)$ is part of a RLC-circuit, figure 3.9. According to the second law of Kirchhoff

$$L\frac{d^2q}{dt^2} + R\frac{dq}{dt} + \frac{q}{C} = V_{em}\cos(\omega_{RF}t) \tag{3.17}$$

the current $I(t)$ in the circuit becomes

$$I(t) = \frac{V_{em}}{Z}\cos(\omega_{RF}t - \Delta) \tag{3.18}$$

with the electric impedance $Z = \sqrt{R^2 + (L\omega_{RF} - 1/C\omega_{RF})^2}$ and Δ the phase

difference between the imposed voltage and the current. The current is maximal when $\omega_{RF} = \sqrt{1/LC}$, figure 3.10.

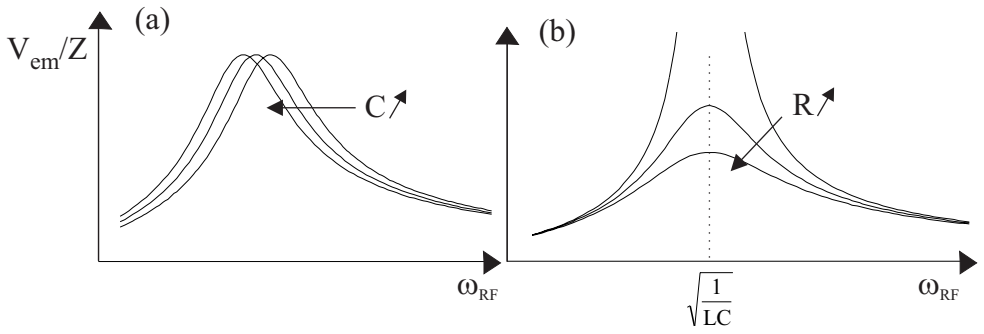

Figure 3.10: *The resonant behavior of V_{em}/Z of an RLC-circuit as a function of the frequency (a) for different capacities and (b) for different resistors.*

To saturate the NMR signal, i.e. to mix the populations of the hyperfine levels fully, a sufficiently large current is required to obtain sufficient magnetic field strength in the RF coil. Therefore a variable capacitor is used to be able to get the highest current at the desired frequency, figure 3.10(a).
To be able to scan over a broad region of g-factors, a large modulation amplitude is required, and the current must be maximal for a large ω_{RF} interval. The FWHM of the resonant curve of V_{em}/Z as a function of ω_{RF} is inversely proportional to the quality factor Q of the RF system. So a low Q-factor is necessary, easily obtained by the intrinsic resistance of the wires, figure 3.10(b). Unfortunately a broader FWHM also implies a lower maximum of the current.
In a classical NMR experiment the β asymmetry is detected as a function of the RF frequency. When a higher or lower value for the g-factor is investigated, the RLC circuit has to be adapted to obtain a maximum current with an appropriate Q-factor for the new frequency region at the expense of valuable beam time. To overcome this problem, the frequency and modulation is kept constant, and the asymmetry is detected as a function of the static magnetic holding field B.
As for the LMR, the static magnetic field is monitored by a Hall probe. The power supply of the magnet is PC-controlled with a Lab-View programme (National

Instruments).

3.2.3 Experimental procedure.

The β asymmetry N_{up}/N_{down} is detected as a function of the static magnetic field. In one sweep, the field is changed every 3 minutes over 3 to 9 field values to avoid an experimental asymmetry induced by beam fluctuations.

Due to technical problems (the communication between the synthesizer and the control PC broke down), no normalization on the β asymmetry without RF was possible. Theoretically, normalization on the asymmetry measured for a static magnetic field far from resonance gives exactly the same result, equation 3.13. However, in this case no correction is made for the experimentally observed asymmetry change due to other effects different from the NMR. For example, the static magnetic field can influence the trajectory of the charged β particles, and therefore induce a change in observed asymmetry when changing the magnetic field. When for every field value the asymmetry is normalized to the asymmetry without RF frequency, this effect is sorted out and a flat baseline is obtained.

All the figures on the β NMR experiments show the asymmetry $W(108^0,\tau)/W(0^0,\tau)$ since the upper detector is the detector positioned at 180^0 with respect to the orientation axis Z_{OR}. The detector positioned under the crystal, is the one at 0^0 with respect Z_{OR}. The observed ratio R' becomes (equations 3.11, 3.12, 3.13):

$$R'_{IN} = \frac{W(180^0,\tau)}{W(0^0,\tau)}(\omega_B = \omega_{RF}) = \frac{\epsilon_{DOWN}}{\epsilon_{UP}} \tag{3.19}$$

$$R'_{OUT} = \frac{W(180^0,\tau)}{W(0^0,\tau)}(\omega_B \neq \omega_{RF}) \approx \frac{\epsilon_{DOWN}}{\epsilon_{UP}}(1 - 2A_1\sqrt{\frac{3I}{I+1}}P(t=0))$$

or after normalization:

$$\frac{R'_{IN}}{R'_{RFoff}} \approx 1 + 2A_1\sqrt{\frac{3I}{I+1}}P(t=0) \tag{3.20}$$

$$\frac{R'_{OUT}}{R'_{RFoff}} = 1 \tag{3.21}$$

When a resonant change in β asymmetry is observed, the g-factor of the isotope can be deduced from the position of the resonance, equation 3.6. From the

amplitude, the initial amount of polarization is obtained, equation 3.20.

3.2.4 Production yields, a comparison of the experimental values with the LISE calculations.

The aim of the NMR measurement is not only to determine the magnetic moment of ^{31}Al and ^{31}Mg, but also to understand the behaviour of the polarization in a fragmentation reaction as a function of momentum selection (section 2.2.2). Therefore, for every selection, the experimentally obtained production yields are compared to the theoretical calculation (LISE program [75]), to investigate if we can rely on this program as far as the momentum selections are concerned.
In order to change the magnetic rigidity of the spectrometer, the thickness of the target is varied by tilting the target over an angle with respect to the vertical direction without changing the settings of the spectrometer. The production rate is obtained by the amount of particles detected by the silicon detector in the LMR measurement chamber divided by the real time, this is the measuring time from which the death time is subtracted. Also the purity of the beam is taken into account. No accurate normalization on the intensity of the primary beam is possible. One can assume for ^{31}Al that no intensity fluctuations occurred since the measurement of production rates are performed in 15 minutes. The situation for ^{27}Na is different. The intensity of the primary beam is put very low in order not to destroy the silicon detector with a too high counting rate and therefore no measurement of the intensity was possible. Since the emittance of the beam after the alpha spectrometer is differently set for each target thickness, influencing the intensity of the primary beam, the comparison of the experimental to the calculated yield is not reliable.

Production rate of ^{31}Al.

The emittance of the beam after the alpha spectrometer is $2 * 2\pi$ mm.mrad. The thickness of the ^{9}Be target amounts to 959 μm at 0^0. The magnetic rigidity

of the first dipole of the LISE spectrometer is $B\rho_1 = 2.8177$Tm, of the second $B\rho_2 = 2.6023$Tm and a 1.062mm Be wedge is used. The momentum acceptance is set to $\Delta p/p = 0.46\%$. Using the Wien filter, the purity of the beam is $98,5(5)\%$ for the different target settings ($B_{WIEN} = 257.2$Gauss).
The absolute theoretical production rates overestimates the experimental values, but the calculation reproduces well the ratio of the production yields of the three selections, as shown in table 3.2 and figure 3.17(a). In the figure, the theoretical values are normalized to the experimental ones at the maximum of the curve, this is for the target tilted to an angle of 40^0.

Production rate of ^{27}Na.

The magnetic rigidity of the first dipole of the LISE spectrometer is $B\rho_1 = 2.91450Tm$, of the second $B\rho_2 = 2.73750Tm$ and a 1.062mm Be wedge is used. The momentum acceptance is set to $\Delta p/p = 0.29\%$. Not only the intensity but also the purity of the beam differs with the thickness of the target. The counting rates are corrected for the emittance and purity, table 3.1 and figure 3.13(a).
Once more, the theoretical yields are proportionally comparable to the experimental. In figure 3.13 the theoretical values are normalized to the experimental at the maximum of the curve, this is at a tilt angle of the target at 40^0.

3.3 Experimental results on ^{27}Na.

Several experiments on ^{27}Na ($t_{1/2}$=301ms, $I^\pi = 5/2^+$, Q_β=9.010MeV, $\mu = 3.895(5)\mu_N$, g=1.558(2) [16]) are performed to examine the best conditions concerning maximal polarization and maximal destruction of the orientation by the radio frequency.
A precise measurement is performed with a small modulation amplitude of $\Delta\nu_{RF} =$ 2kHz and modulation frequency $\nu_{mod} = 5$Hz on a central frequency of $\nu_{RF} =$

1000kHz and $B_1 = 4$Gauss, with the target tilted to 58^0. A fit with a Gaussian-shape function ($\chi^2 = 1.4$) of these data yields a g-factor of 1.559(1), figure 3.11. With a systematic error of 0.1% on the measurement of the static field, a g-factor of 1.559(2) or $\mu = 3.896(6)\mu_N$ is found. The result is consistent with earlier g-factor measurement g=1.558(2) [16].

From the decay of ^{27}Na (figure 1.17), one can deduce that 84.3% of the β-decay has a radiation parameter $A_1 = +\sqrt{(I+1)/3I} = +0.6831$ and 11.2% has $A_1 = +1/\sqrt{3I(I+1)} = +0.1380$. For the total decay this becomes $A_1 \approx +0.619$. With equation 3.20 and $R'_{OUT} = 0.618(7)$ the amplitude of the resonance is 5.4(1.4)% in asymmetry or $P = 3.0(0.8)$%.

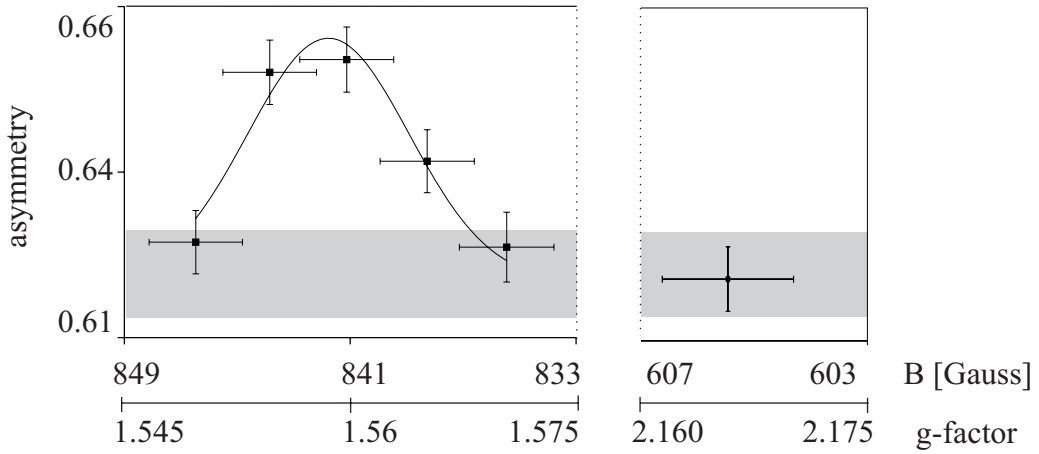

Figure 3.11: *Precise measurement of the g-factor of ^{27}Na, $\nu_{RF} = (1000 \pm 2)kHz$ and $\nu_{mod} = 5Hz$, resulting in g=1.5585(23).*

The aim of the experiment is first to measure the g-factor of ^{31}Al and ^{31}Mg with low accuracy in order to have an idea about the order of magnitude. This implicates a scan of a broad g-factor range to cover the full region predicted for different configurations of the nuclei. To find the optimal RF-conditions, several test with a large modulation amplitude are performed on ^{27}Na, figure 3.12.

To investigate the best settings of the RF frequency, a first test using $\nu_{RF} = (450 \pm 35)$kHz and $B_1 = 4.5 \pm 1.5$Gauss is performed with a modulation fre-

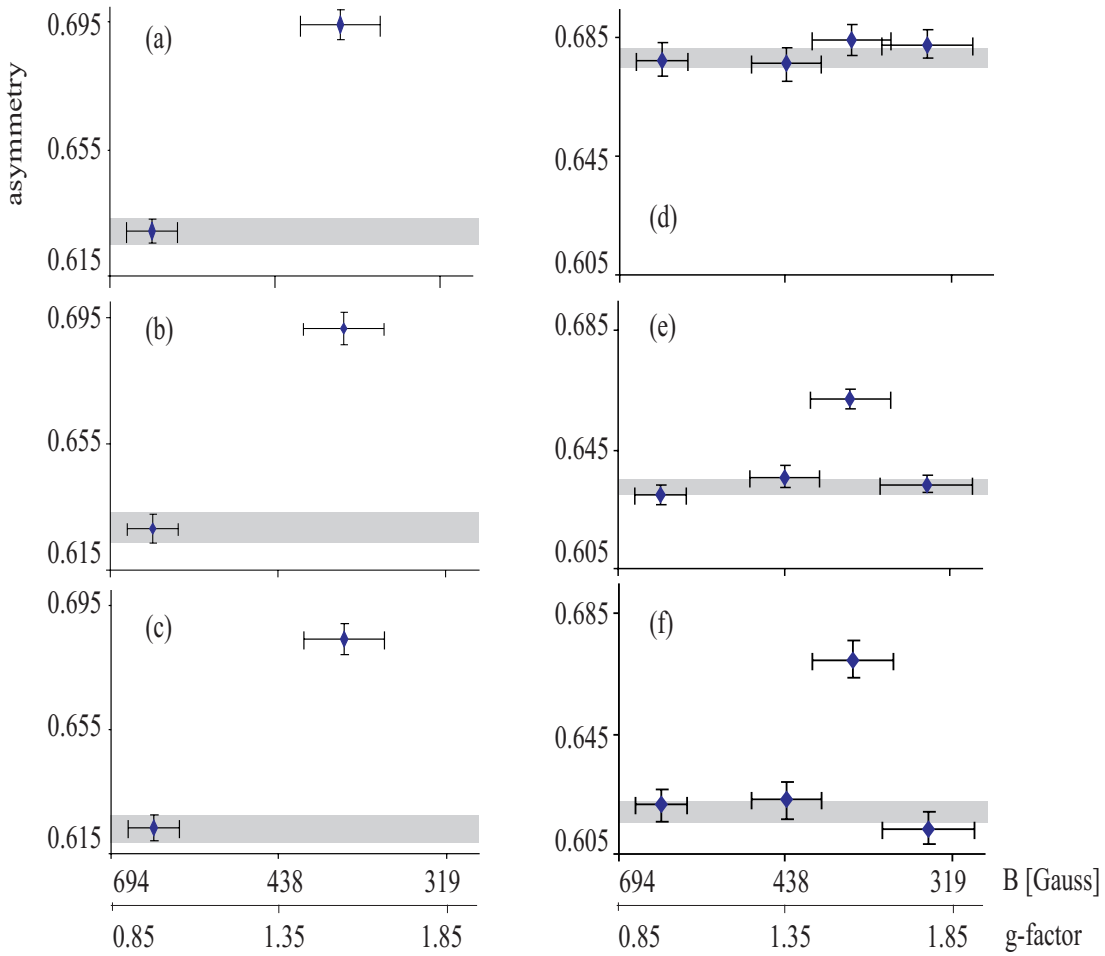

Figure 3.12: *Several test are performed on ^{27}Na to find the optimal conditions for the maximal amount of initial polarization and maximal destruction of the polarization, using $\nu_{RF} = (450 \pm 35) kHz$ and $B_1 = 4.5(1.5)\, Gauss$ (a)$\nu_{mod} = 5Hz$, target at 58^0 (b)$\nu_{mod} = 800Hz$, target at 58^0 (c)$\nu_{mod} = 5Hz$, target at 58^0 and using the Wien filter (d)$\nu_{mod} = 100Hz$, target at 40^0 (e)$\nu_{mod} = 100Hz$, target at 50^0 (f)$\nu_{mod} = 100Hz$, target at 58^0.*

quency of $\nu_{mod} = 5$Hz. This means that the frequency is modulated 1.5 times during the halflife of the nucleus, figure 3.12(a) (emittance after the alpha spec-

trometer $2 * 2\pi$ mm.mrad, the target at 58^0). The β-asymmetry is +10.4(1.0)% or $P = 5.7(0.6)\%$.

When the modulation amplitude $\Delta\nu_{RF}$ and the amplitude of the RF field B_1 are kept constant, but the modulation frequency ν_{mod} is raised, the power at the resonance frequency is lowered. To examine if the system is saturated, the modulation frequency is put at $\nu_{mod} = 800$Hz, or 241 times a sweep over the whole frequency band during $t_{1/2}$, figure 3.12(b). A similar β-asymmetry as in previous case is found 10.1(1.1)% or $P = 5.6(0.6)\%$, indicating that the system is saturated in both situations.

To obtain a beam with higher purity, the Wien filter can be used. The spin polarization of the fragments will be influenced by the static magnetic field B_{WIEN} which is in the horizontal direction (section 3.2.1), but not by the electric field E_{WIEN}. Although the direction of the beam is not disturbed, the spins rotate over a small angle with the Larmor frequency $\omega_L = g\mu_N B_{WIEN}/\hbar$ during their passage through the velocity filter. Figure 3.12(c) shows the result of the measurement making use of the Wien filter, $B_{WIEN} = 252$Gauss. With the speed of the fragments of 10.14cm/ns and 5m effective magnetic length of the filter, the passage takes t=49ns. The spins will be rotated over $\theta = g\mu_N B_{WIEN}.t/\hbar = 5.28^0$, the polarization in the vertical direction is reduced with $\cos(5.28^0) = 0.996$ and this is negligible as the asymmetry proves: 9.8(1.1)% or $P = 5.4(0.6)\%$.

To study the polarization as a function of the longitudinal momentum selection, three test are performed keeping the settings for the RF frequency constant ($\nu_{RF} = (450 \pm 35)$kHz, $\nu_{mod} = 100$Hz, $B_1 = 4.5(1.5)$Gauss). A first test is performed on fragments from the center of the distribution, using the target tilted to 40^0 with respect to the vertical direction (emittance of the primary beam after the alpha spectrometer $0.8 * 0.8$ mm.mrad) , figure 3.12(d) and figure 3.13(a). With this settings, no appreciable asymmetry is obtained: 0.7(0.9)% or $P = 0.4(0.5)\%$. The target is tilted at 50^0 for a second test (emittance $1 * 1\pi$ mm.mrad). The selected fragments have a slightly higher momentum than the central one, figure 3.13(a). The total asymmetry is 4.6(0.6)% or $P = 2.5(0.3)\%$, figure 3.12(e). In the third test, the target is set at 58^0 (emittance $2 * 2\pi$), figure 3.13(a). The

obtained asymmetry is 8.2(1.1)% or $P = 4.5(0.6)\%$, figure 3.12(f).

Table 3.1: Comparison for the ^{27}Na isotopes of the experimentally obtained production rate I_{exp} and the calculated rate with LISE [75] I_{the} for different tilt angles of the target or target thickness d. The experimentally obtained polarization is also tabulated.

tilt angle	d μm	emittance mm.mrad	purity %	I_{exp} cps	I_{the} cps	P %
40^0	1252	$0.8 * 0.8\pi$	93	1880	$1.4 * 10^4$	0.4(0.5)
50^0	1492	$1 * 1\pi$	98	1601	$1.2 * 10^4$	2.5(0.3)
58^0	1810	$2 * 2\pi$	96.5	755	$5.9 * 10^3$	4.5(0.6)

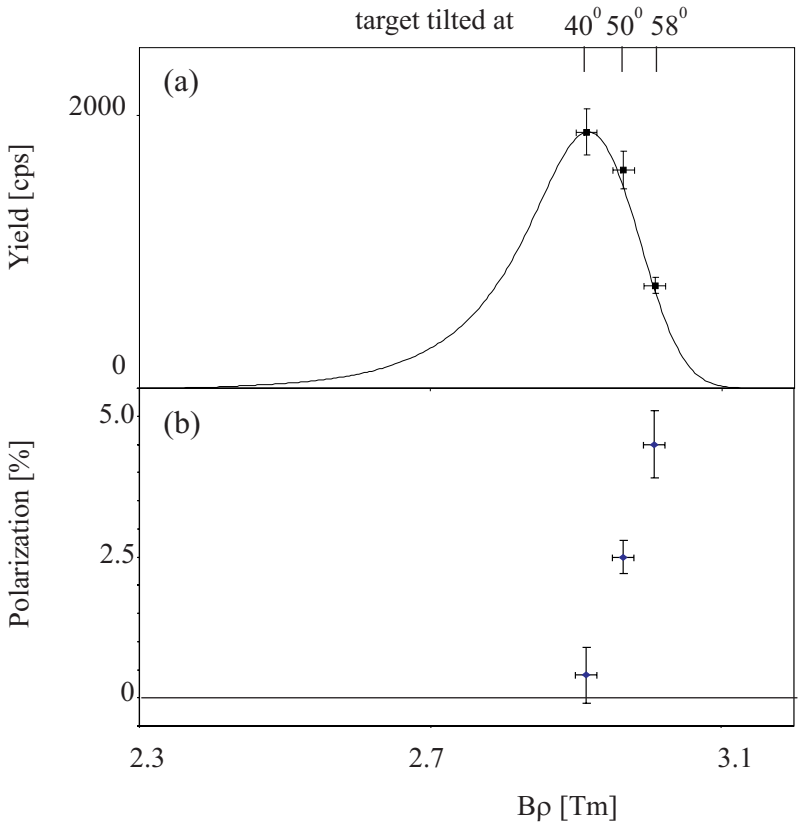

Figure 3.13: *(a) The yield of ^{27}Na as a function of the selection in longitudinal momentum, comparison of theoretical [75] to experimental values. (b) The experimental polarization as a function of the magnetic rigidity of the Lise spectrometer.*

3.4 Experimental results on ^{31}Al.

The emittance of the beam after the alpha spectrometer is put at $1*1\pi$ mm.mrad for all NMR experiments on ^{31}Al ($t_{1/2}$=644ms, Q_β=7.995MeV). The search for the g-factor is performed with the target tilted to 56^0 with respect to the vertical direction, figure 3.17(a).

Since the spin is experimentally not known, but limited to $I = 3/2$ or $5/2$, a broad scan of the g-factor is made from 0.5 $\leq$ g-factor $\leq$ 1.9 to cover all possible g-factors, section 4.3. A radio frequency $\nu_{RF} = (450 \pm 35)$kHz is used with $\nu_{mod} = 50$Hz and $B_1 = 8$Gauss. Although the data between 600 and 1200 Gauss have a descending tendency, figure 3.14, one data point has clearly a higher asymmetry, indicating that the g-factor of ^{31}Al is situated in the interval $[1.387(1), 1.621(1)]$. The descending tendency for high magnetic fields is probably due to the interaction of the charged β particle in the static field.

Deduced from the decay (figure 1.13), the radiation parameter amounts to $A_1 = +\sqrt{(I+1)/3I} = +0.683$ for 91% of the β decay, and $A_1 = +1/\sqrt{3I(I+1)} = +0.1380$ for 8% of the decay. In total this gives $A_1 \approx +0.639$. With equation 3.20 and $R'_{OUT} = 0.713(4)$ around 400 Gauss, the amplitude of the resonance is 4.0(1.1)% or $P = 2.1(0.6)\%$.

To increase the accuracy on the measured g-factor, a smaller RF modulation and higher magnetic field is used in the next two measurements. The radio frequency is now $\nu_{RF} = (1000 \pm 12)$kHz, $\nu_{mod} = 50$Hz and $B_1 = 6$Gauss. Due to technical problems the Wien filter is not used, resulting in a less pure beam, and the silicon detector monitoring the purity, is accidentally put on non-active. With $R'_{OUT} = 0.779(2)$ the amplitude of the resonance is 2.9(0.5)% or $P = 1.6(0.3)\%$, figure 3.15(a).

The asymmetry is almost 30% lower than in the first experiment and can not be explained by an increase of the amount contaminants of a few percent. To investigate if the power of the RF signal is sufficient to saturate the resonance, a second measurement is performed with $B_1 = 10$Gauss, giving an even smaller asymmetry. With $R'_{OUT} = 0.786(2)$ the amplitude of the resonance is 1.5(0.5)%

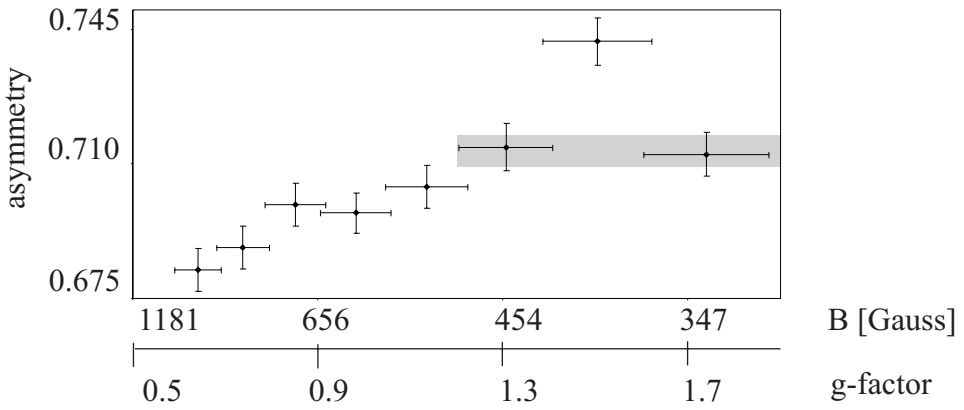

Figure 3.14: *Study of the g-factor of* ^{31}*Al using* $\nu_{RF} = (450 \pm 35) kHz$ $\nu_{mod} = 50\,Hz$ *and* $B_1 = 8\,Gauss$.

or $P = 0.8(0.3)\%$, figure 3.15(b).

The main results of these two measurements is the value of the g-factor: $g = 1.517(20)$. The accuracy of this value is partly determined by the modulation amplitude of the radio frequency, and partly by the accuracy of the readout of the static magnetic field.

For the last measurement the target is tilted to 50^0 with respect to the primary beam in order to select the fragments with a momentum closer to the central momentum, figure 3.17(a). With $R'_{OUT} = 0.816(3)$ the amplitude of the resonance is $2.2(0.6)\%$ or $P = 1.2(0.3)\%$, figure 3.16. The same result for the g-factor is found: $g = 1.517(20)$.

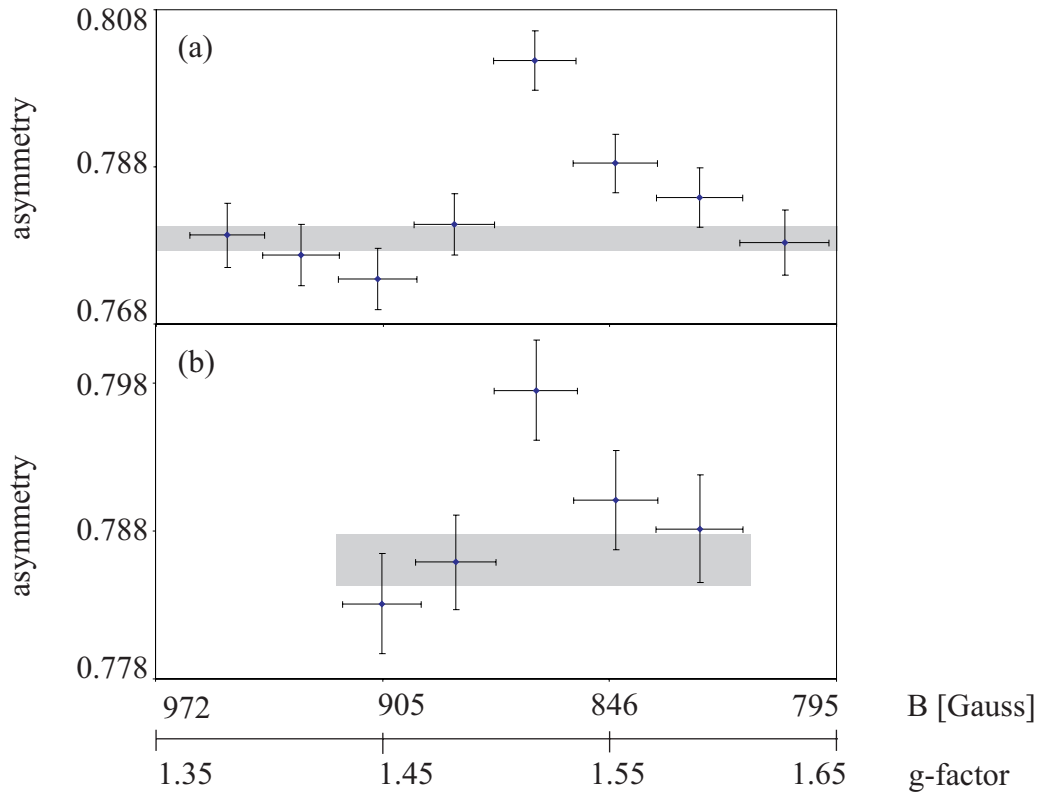

Figure 3.15: *Study of the g-factor of* ^{31}*Al with high accuracy, using* $\nu_{RF} = (1000 \pm 12) kHz$ $\nu_{mod} = 50 Hz$ *(a)*$B_1 = 6\,Gauss$ *(b)*$B_1 = 10\,Gauss$.

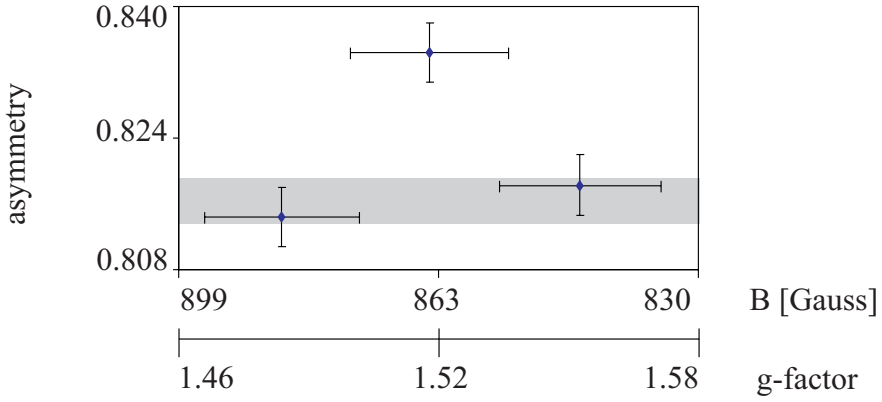

Figure 3.16: *g-factor measurements using a target tilted at* 50^0, $\nu_{RF} = (1000 \pm 12)kHz$, $\nu_{mod} = 50\,Hz$ *and* $B_1 = 10\,Gauss$.

Table 3.2: Comparison for the ^{31}Al isotopes of the experimentally obtained production rate I_{exp} and the calculated rate with LISE [75] I_{the} for different tilt angles of the target or target thickness d. The obtained polarization is also mentioned.

tilt angle deg	d μm	I_{exp} cps	I_{the} cps	P %
40^0	1252	2279	$1.4 * 10^5$	
50^0	1492	1254	10^5	1.2(0.3)
56^0	1715	457	$2.8 * 10^4$	$2.1(0.6)^{fig\ 3.14}$
56^0				$1.6(0.3)^{fig\ 3.15(a)}$
56^0				$0.8(0.3)^{fig\ 3.15(b)}$

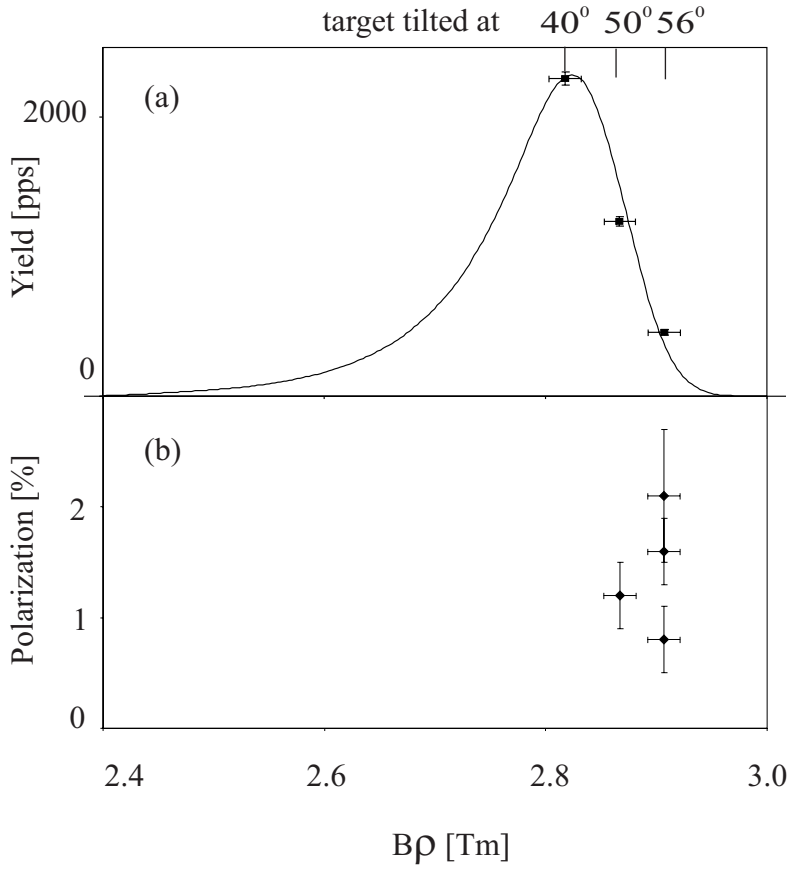

Figure 3.17: *(a) The yield of ^{31}Al as a function of the selection in longitudinal momentum, comparison of theoretical [75] to experimental values. (b) The experimental polarization as a function of the magnetic rigidity of the Lise spectrometer.*

3.5 Experimental results on ^{31}Mg.

In order to determine the g-factor of ^{31}Mg, several measurements are performed with following parameters. The emittance of the beam after the alpha spectrometer is $10 * 10\pi$. The target thickness is varied. The magnetic rigidity of the first dipole of the LISE spectrometer is $B\rho_1 = 3.0017$Tm, of the second $B\rho_2 = 2.7954$Tm and a 1.062mm Be wedge is used. The momentum acceptance is set to $\Delta p/p = 0.46\%$. The Wien filter is used to purify the secondary beam ($B_{WIEN} = 261.1$Gauss). The purity of the secondary beam amounts to 96(2)%. With a primary beam of $2\mu A$ the silicon detector in the measurement chamber counts typically 250 particles per second, or 10 times less compared to the LMR measurement, when the particles are selected in the forward direction (no deviation of the primary beam and selection of the fragments in the middle of the momentum distribution).

For the first setting (SET1), the thickness of the ^{9}Be target is $1991\mu m$ ($959\mu m$ at 61^0), figure 3.18(a). A thicker target of $2103\mu m$ ($2071\mu m$ at 10^0) is used for the second setting (SET2), figure 3.18(b). And the third setting (SET3) is a target of $1558\mu m$ ($959\mu m$ at 52^0), figure 3.18(c).

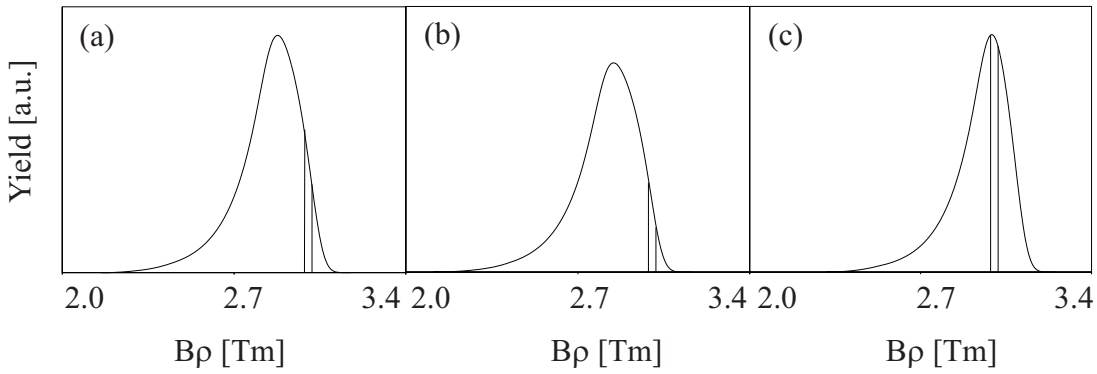

Figure 3.18: *The target thickness is varied without changing the magnetic rigidity of the Lise spectrometer in order to obtain different selections of the longitudinal momentum of the ^{31}Mg fragments, (a)*$1991\mu m$ *(SET1) (b)*$2103\mu m$ *(SET2) (c)*$1558\mu m$ *(SET3).*

Different measurements are performed using fragments selected according to SET1, figures 3.19(b), according to SET2,figures 3.19(a,c) and 3.20(b), and according to SET3,figures 3.20(a). A broad g-factor region is scanned to cover all possible values, table 4.3.

The data from figure 3.19 show an increasing asymmetry for decreasing magnetic field between 2000 and 1000 Gauss. For lower fields, lower than 1000 Gauss it is not clear, in figure 3.19(b) the tendency persist but in figure 3.20 not. Similar tendency was seen in the ^{31}Al measurement although for lower magnetic field values between 1200 and 600 Gauss (figure 3.14). This can be understood by the endpoint energy of the β's being $\sim 2MeV$ lower for the ^{31}Al decay. The influence on trajectory of the particles is therefore detectable from lower fields on.

There are two indications for a resonance signal corresponding to: $0.453 \leq$ g-factor ≤ 0.530 fig 3.19(b), and $0.454 \leq$ g-factor ≤ 0.611 fig 3.19(c).

For each data set obtained with one specific setting of the spectrometer (each setting has a different asymmetry because of a different implantation of the isotopes into the crystal) a function $b.ln(x) - a$ is fitted through the data, in order to normalize to asymmetry $R'_{OUT} = 1$. For SET1 $a = 0.876(1)$ and $b = 0.0322(1)$, for SET2 figure 3.19(a) $a = 0.803(1)$ and $b = 0.0366(1)$. For a second measurement with the same settings (SET2) the beam is retuned due to technical problems and therefore, new fit-parameters are appropriate, figure 3.19(c) $a = 0.745(1)$ and $b = 0.0366(1)$.

All the normalized data with the same settings for the radio frequency and with the same static magnetic field are averaged, figure 3.21. For a g-factor of g=0.498(26), an asymmetry of 1.6(5)% is reached, giving an indication of the magnetic moment of ^{31}Mg. The obtained accuracy on the change in asymmetry is not large enough to give a conclusive result on the g-factor.

One more measurement with smaller modulation amplitude is performed using SET2, $\nu_{RF} = (450 \pm 9)$kHz and $\nu_{mod} = 50$Hz, to establish the g-factor with higher precision, figure 3.22. The dotted line is the change in asymmetry that is expected from the previous results of the measurement using a broad modula-

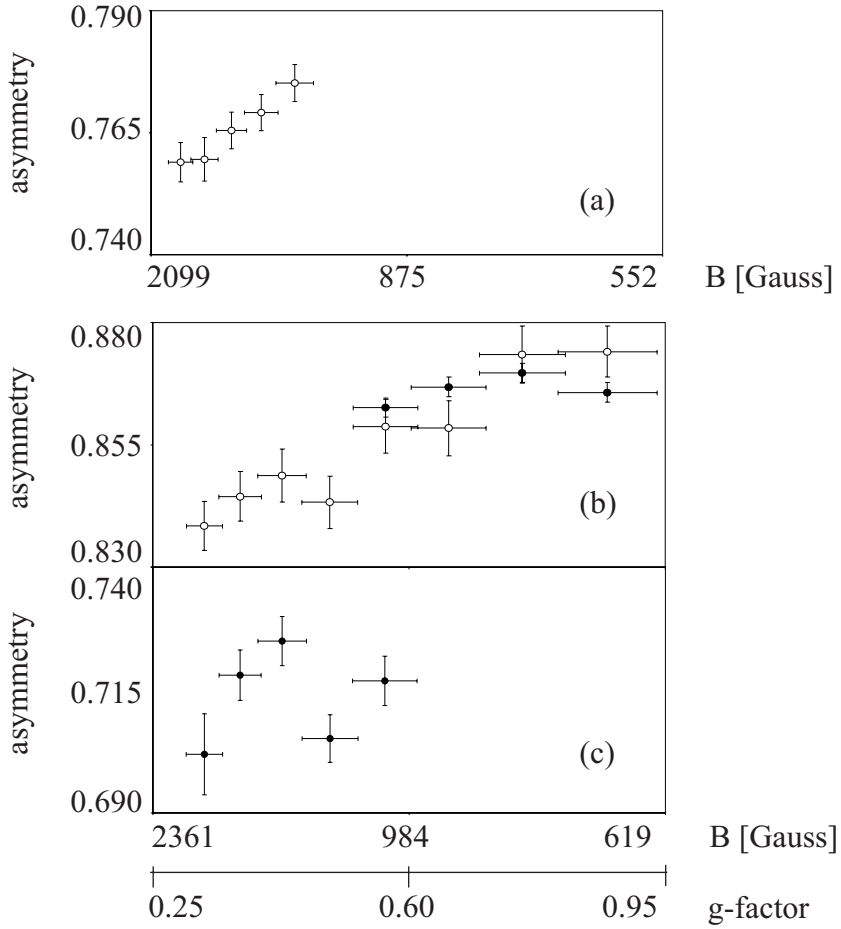

Figure 3.19: *NMR measurement on ^{31}Mg obtained with (a)SET2, $\nu_{RF} = (400 \pm 23)kHz$, $\nu_{mod} = 50Hz$ and $B_1 = 4Gauss$ (b)SET1, $\nu_{RF} = (450 \pm 35)kHz$, $\nu_{mod} = 50Hz$ and $B_1 = 4Gauss$ (c)SET2, $\nu_{RF} = (450 \pm 35)kHz$, $\nu_{mod} = 50Hz$ and $B_1 = 4Gauss$.*

tion amplitude. Unfortunately, the statistics are not sufficient in order to determine the g-factor unambiguously. For g=0.495(10) the measured β-asymmetry is $-1.1(0.7)\%$, which does not contradict but also does not confirm the results obtained using a broad modulation amplitude.

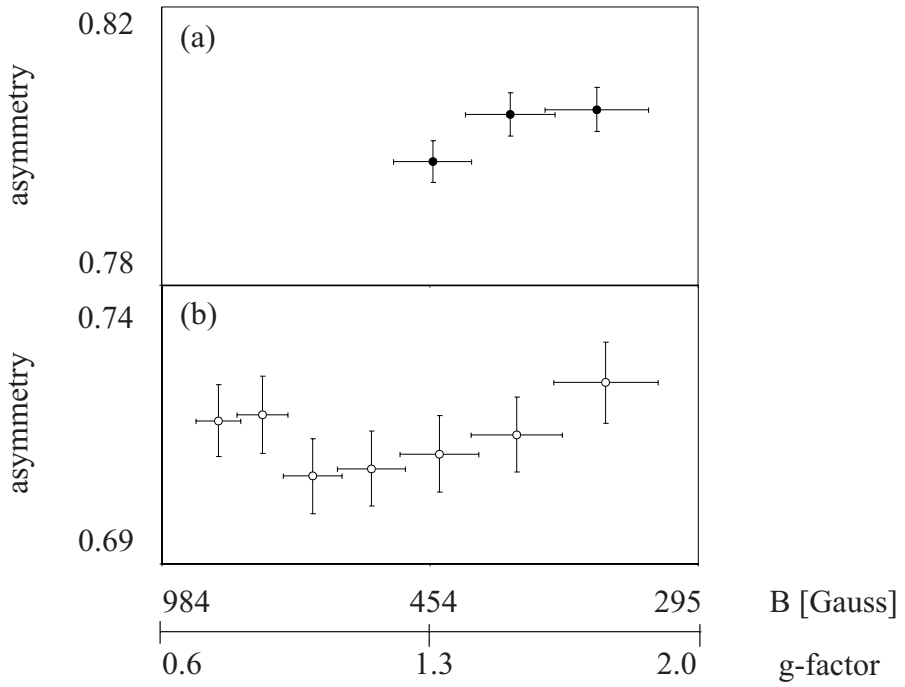

Figure 3.20: *NMR measurement on ^{31}Mg obtained using $\nu_{RF} = (450 \pm 35)kHz$, $\nu_{mod} = 50Hz$ and $B_1 = 4Gauss$ (a) for a selection of fragments using SET3 (b) using SET2.*

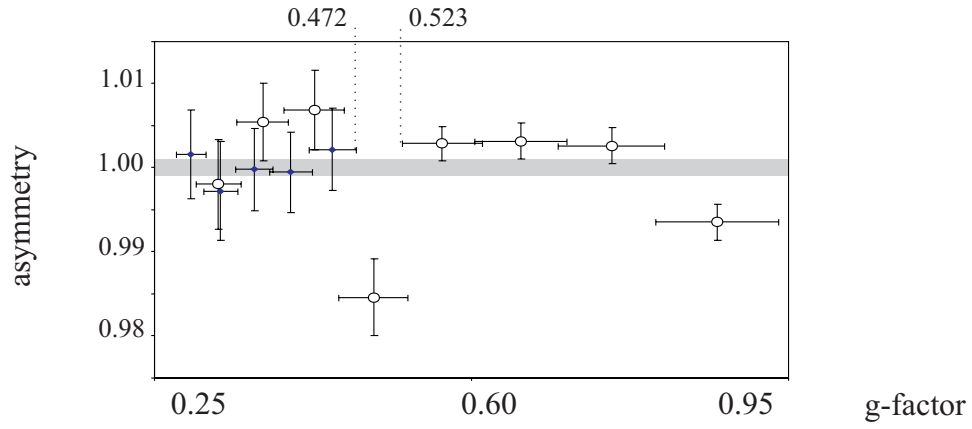

Figure 3.21: *Average of the normalized data on ^{31}Mg obtained with a large modulation amplitude.*

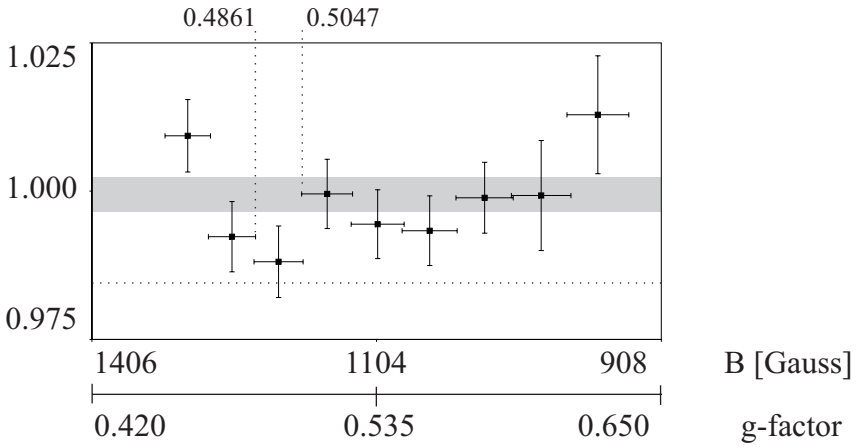

Figure 3.22: *Normalized data of the NMR measurement on ^{31}Mg using SET2, $\nu_{RF} = (450 \pm 9)kHz$, $\nu_{mod} = 50Hz$ and $B_1 = 7Gauss$. The dotted line shows the asymmetry expected from the measurement with a broad modulation amplitude. Because of the poor statistics, the results do not confirm but do not contradict either the previous results.*

Chapter 4

Interpretation of the results.

4.1 Polarization in a fragmentation reaction.

A positive polarization is obtained for ^{27}Na and ^{31}Al when the fragments with a larger longitudinal momentum than the primary beam are selected, figure 3.13 and 3.17. When compared to the theoretical model of K.Asahi *et al.* [86], one concludes that Coulomb repulsion between target nucleus and projectile dominates over nuclear attraction. The ^{27}Na and ^{31}Al fragments produced by fragmentation of ^{36}S on a ^{9}Be target, follow the near-side trajectory, figure 3.3.

For ^{27}Na, in the middle of the momentum distribution no considerable polarization is detected, 0.4(0.5)%, figure 3.13. Clearly a raising trend of the polarization is observed as a function of selection of the fragments. A maximum of 4.5(0.6)% is obtained for fragments in the extreme of the momentum distribution. This trend reproduces nicely the theoretical model, figure 3.2.

For the ^{31}Al, no measurement in the middle of the momentum distribution is performed, but a positive polarization is observed, figure 3.17. The raising trend of the orientation as a function of the momentum selection is not clear since a lot of scattering is present on the value for the polarization at the extreme of the distribution. No precise reason is found for this scattering. A maximum polarization of 2.1(0.6)% is measured for ^{31}Al. This is half the value compared

to ^{27}Na. It could be due to a faster relaxation of the ^{31}Al ($t_{1/2} = 644ms$) in the MgO crystal compared to the relaxation of ^{27}Na ($t_{1/2} = 301ms$) in NaCl.

4.2 The quadrupole and magnetic moment of ^{29}Mg.

Table 4.1: Calculated values with the USD interaction for the magnetic moment and quadrupole moment of ^{29}Mg using $e^{\nu}_{eff} = 0.5$ and $e^{\pi}_{eff} = 1.3$.

μ_{free} $[\mu_N]$	Q_{the} [mb]	ν_Q/μ_{the} $[kHz/\mu_N]$
0.953	-98	-165

From the theoretical shell model calculations using the USD interaction a magnetic moment $\mu = 0.953\mu_N$ is obtained. With a spin $I = 3/2$ the g-factor of the ground state of ^{29}Mg is g=0.635. With temperature $T = 4.25(25)K$ and using the Korringa relation (equation 2.30), the spin lattice relaxation becomes $T_1 = 1.7sec$. The beam was pulsed and data are only collected during beam on $1.5sec$ which is of the same order of the relaxation time. Several nuclei are fully relaxed before decay. They do not contribute to the LMR but cause a constant back ground, inducing a reduction of the amplitude of the resonances, figure 4.1. The reduction factor is calculated assuming a continuous implantation of the isotopes [91, 92]. Therefore, in order to estimate the reduction factor, the ratio of the relaxation time to the detection time is used instead of the ratio of the relaxation time to the lifetime and a factor 5 is obtained.

Assuming a large value for the spin alignment $A = 20\%$ and a factor 5 for the orientation loss, the orientation tensor component becomes $B^0_2 = 0.06$. To fit the experimental data with a LMR curve, figure 2.26, a $B^0_2 = 0.22(7)$ was required. This means that 3 to 4 times more initial alignment was necessary to

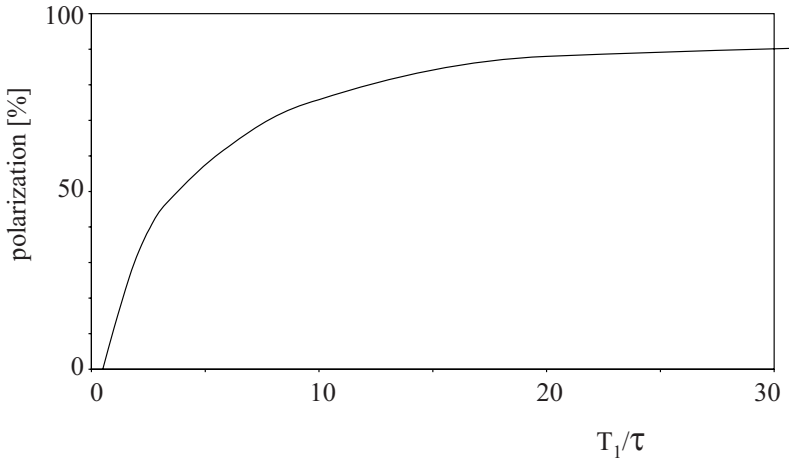

Figure 4.1: *Influence of the relaxation on the amplitude of a level mixing resonance assuming a continuous implantation of the isotopes [91, 92].*

reproduce the fitted resonance. Moreover, an asymmetry parameter $A_1 = -0.3$ was assumed, taking only the β particles with the highest energy into account (section 2.4.2). If this parameter is smaller, a even larger B_2^0 is required. Therefore, one can conclude that the statistics are not sufficient in order to determine the magnetic and the quadrupole moment of ^{29}Mg.

4.3 The spin and g-factor of ^{31}Al.

The magnetic moment of the odd-even nucleus (Z=13,N=18) can be estimated by the Schmidt value assuming the extreme single particle shell model (SPSM). Following equation is used [93]

$$\mu = g_l^\pi (j - 1/2) + 1/2 g_s^\pi \tag{4.1}$$

for j=l+s, l the orbital angular momentum, s the spin angular momentum of the single particle, and with the free proton orbital and spin g-factors $g_l^\pi = 1.0$ and $g_s^\pi = 5.58$. In this calculation, the ground state of ^{31}Al is assumed to have a configuration with all neutron pairs coupled to spin I=0 and with 1 unpaired proton in the $d_{5/2}$ orbit $(\pi d_{5/2}^5)_{5/2^+}$ $(\nu = 1)$.

From this calculation the magnetic moment is obtained. In the SPSM the nuclear spin I is the total angular momentum of the single particle $I = j = 5/2$ and the g-factor can be obtained with $\mu = jg\mu_N$.

The theoretical value g=1.917 is much higher than the experimental value g=1.517(20) (table 4.2 and figure 3.15and 3.16). From this, one can conclude that the configuration is not purely the one proposed above.

Calculations with the USD interaction provide an excellent description of the low lying spectrum, figure 1.12 [29]. A spin $I = 5/2$ is predicted for the ground state, with 57% of the $\pi(d_{5/2})^5\ \nu(d_{5/2})^6(s_{1/2})^2(d_{3/2})^2$ configuration. The remaining part of the $5/2^+$ wave function consists of a complex mixture of many sd-shell configurations. The theoretical value is calculated using the free nucleon g-factors ($g_l^\pi = 1.0$, $g_l^\nu = 0.0$, $g_s^\pi = 5.58$ and $g_s^\nu = -3.81$). A very good agreement is found between the USD_{free} and experimental g-factor. It confirms that there is less quenching of the M1 spin operator than of the Gamow-Teller operator for sd nuclei, as claimed by A.Brown *et al.* [9].

The calculated value for the ground state with $I = 3/2^+$ is $g = 0.806$, much lower than the experimental. This allows the assignment of spin and parity $I = 5/2^+$ for the ground state of ^{31}Al.

Using the effective charges $e_\pi = 1.3$ and $e_\nu = 0.5$, a quadrupole moment $Q = 142.1mb$ is predicted. This value needs to be confirmed in a future experiment.

Table 4.2: Experimental and calculated values for the g-factor of ^{31}Al with $I = 5/2$.

^{31}Al	g_{exp}	g_{free}^{SPSM}	g_{free}^{USD}
I=5/2	1.517(20)	1.917	1.524
I=3/2	1.517(20)		0.806

From the measured magnetic moment corresponding to a ground state with $I = 5/2^+$ can be concluded that no intruder configurations are necessary to describe

the ground state of ^{31}Al. It can be understood in the pure sd space. Therefore, the isotope is clearly out of the Island of Inversion.

4.4 The spin, g-factor and quadrupole moment of ^{31}Mg.

4.4.1 Theoretical predictions for the quadrupole and magnetic moment.

When the experiment on ^{31}Mg was initiated, a LMR and NMR measurement on the ground state with spin $I = 3/2^+$ was aimed. However, the obtained data show a LMR of a level with spin $I = 7/2$, figure 2.21. From simulations of such a resonance a lower limit on the lifetime of this level can be deduced $\tau \geq 20\mu sec$. Therefore, the most important conclusion of this measurement is that for ^{31}Mg, a long living state with spin $I = 7/2$ is observed. Whether it is the ground state or an isomeric state can not be decided (see further).

Theoretical values for the magnetic moment and quadrupole moment are given for the $I = 3/2$ case as well as the values obtained for a $I = 7/2$ state, table 4.3. Using the Oxbash code with the WBMB interaction [7], the magnetic moment and quadrupole moment are calculated for the lowest lying, pure 0, 1 and $2\hbar\omega$ configurations. In the pure $0\hbar\omega$ configuration, all the neutrons are confined in the sd space and the WBMB interaction restricted to the sd space is exactly the same as the USD interaction. In the 1 and $2\hbar\omega$ configurations, 1 and 2 neutrons respectively are occupying the fp shell.

A more recent interaction, developed to fit the N=28 neutron rich isotopes by Retamosa et al. [48], is used with the Antoine code for the pure and for the mixed 0 and $2\hbar\omega$ states, and for the lowest lying $1\hbar\omega$ state. All these states are very low in energy, but with this interaction, the $7/2^-$ state becomes the ground state, figure 4.2. Due to the open $d_{5/2}$ proton shell (Z=12) and the open $f_{7/2}$ neutron shell, a large quadrupole proton neutron interaction induces deformation.

The protons couple to a 2^+ configuration and the $7/2^-$ ground state originates from a coupling of the 2^+ proton configuration with a $7/2^-$ neutron configuration $(\pi(d_{5/2})_{2+} \otimes \nu(f_{7/2})_{7/2-})_{7/2^-}$.

Calculations with a similar interaction but with a small modification on the

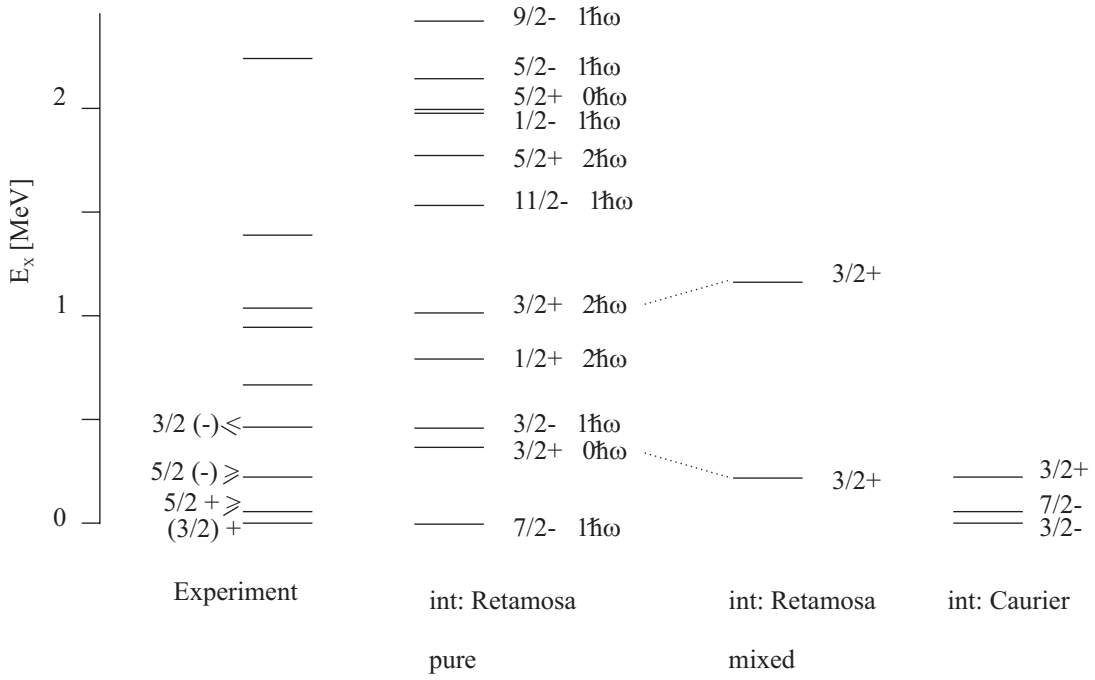

Figure 4.2: *Comparison of the experimental and theoretical level structure of* ^{31}Mg *using the interaction of Retamosa et al. [48], and using the interaction of Caurier et al. [49].*

monopole term by Caurier *et al.* [49], confirm that the normal configurations are almost degenerate with the opposite parity $1\hbar\omega$ intruders, while the $2\hbar\omega$ intruders appear a bit above. But here, the competition for the ground state is between the normal $(\nu d_{3/2}^3)_{3/2^+}$ and the $1\hbar\omega$ intruder $(\pi(d_{5/2})_{2+} \otimes \nu(f_{7/2})_{7/2-})_{3/2^-}$ configuration.

Also for the odd-even ^{31}Mg, the magnetic moment can be estimated by the Schmidt value assuming the extreme single particle shell model (SPSM). When the uncoupled neutron is situated in the $d_{3/2}$ orbital, the magnetic moment becomes $\mu = -g_s^\nu \frac{j}{(2(j+1))}$ for j=l-s, with the free neutron orbital and spin g-factors

$g_l^\nu = 0$ and $g_s^\nu = -3.81$. In this calculation, the ground state of ^{31}Mg is assumed to have all proton pairs coupled to spin I=0 and the unpaired neutron in the $(\nu d_{3/2}^3)_{3/2^+}$ ($\nu = 1$). The obtained magnetic moment is $\mu = 1.14\mu_N$ or $g = 0.76$. When the uncoupled neutron is positioned in the $f_{7/2}$ orbital, then j=l+s and the Schmidt value comes down to $\mu = 1/2 g_s^\nu = -1.9\mu_N$, or $g = -0.543$.

Table 4.3: Experimental and calculated values for the gyromagnetic ratio and quadrupole moment of ^{31}Mg.

I^π	SPSM	g_{free}			
$3/2^+$	$0\hbar\omega$	0.76			
$7/2^-$	$1\hbar\omega$	-0.54			
I^π	WBMB [7]	g_{free}	g_{eff}	Q_{the} [mb]	ν_Q/μ_{the} $[kHz/\mu_N]$
$3/2^+$	$0\hbar\omega$	0.895	0.849	86	103
$3/2^+$	$2\hbar\omega$	0.777	0.705	-86	-118
$7/2^-$	$1\hbar\omega$	-0.365	-0.343	-184.7	232
I^π	Retamosa [48]	g_{free}		Q_{the} [mb]	ν_Q/μ_{the} $[kHz/\mu_N]$
$3/2^+$	$0\hbar\omega$	0.89		92	96
$3/2^+$	$2\hbar\omega$	0.43		-146	-316
$3/2^+$	mixed	0.81		50	57
$7/2^-$	$(2+)\otimes(1\hbar\omega)$	-0.32		-204	254
$3/2^-$	$(2+)\otimes(1\hbar\omega)$	-1.23		-99	75
I	Experiment	g_{exp}		Q_{exp} [mb]	ν_Q/μ_{exp} $[kHz/\mu_N]$
7/2	LMR	$-0.5\binom{-0.2}{+0.4}$		$\pm 170\binom{+70}{-140}$	158.2(2.6)
?	NMR	$\pm 0.498(26)$		$\pm 170(10)$	

4.4.2 Comparison with the experimentally obtained results.

It is clear that from theoretical point of view the spin of the ground state is not fixed. But, for a state with spin $I = 7/2^-$ a negative magnetic and a negative quadrupole moment are predicted by theory. The negative magnetic moment is consistent with the experimentally obtained negative value using the LMR method. Although the accuracy is rather low, there is no doubt about the sign. The sign of the quadrupole frequency can not be fixed because of the unknown sign of the asymmetry parameter A_1, and of the unknown sign of the spin alignment.

The measured ratio of the quadrupole moment to the magnetic moment is determined very accurately. However, comparing the ratio to theory does not yield a lot of information since the experimental magnetic moment and quadrupole moment can differ slightly from the predicted ones, but result in a very different experimental ratio compared to the theoretical ratio. A measurement of one of the moments separately is necessary.

The obtained ratio is smaller than the theoretical value for a $7/2^-$ state, predicted by the two models (table 4.3).

If the indication for the g-factor obtained with the NMR method and with the LMR method is assumed to be correct, some deductions can be made.

The experimental quadrupole moment $Q_{exp} = \pm 170(10)mb$ is slightly lower than the calculated values in both models (table 4.3). A negative sign can be assumed based on the negative sign deduced from theory.

From the Nilsson diagram, the deformation parameter β can be estimated, figure 4.3. For the odd particle nucleus with 19 neutrons and spin I=7/2, the projection of the spin on the symmetry axis of the nucleus is K=7/2 and the nucleus has an oblate shape with a deformation parameter $\beta \sim -0.3$. With the relation between the intrinsic and the measured spectroscopic quadrupole moment

$$Q_0 = \frac{(2I+3)(I+1)}{3K^2 - I(I+1)} Q_{spec} \tag{4.2}$$

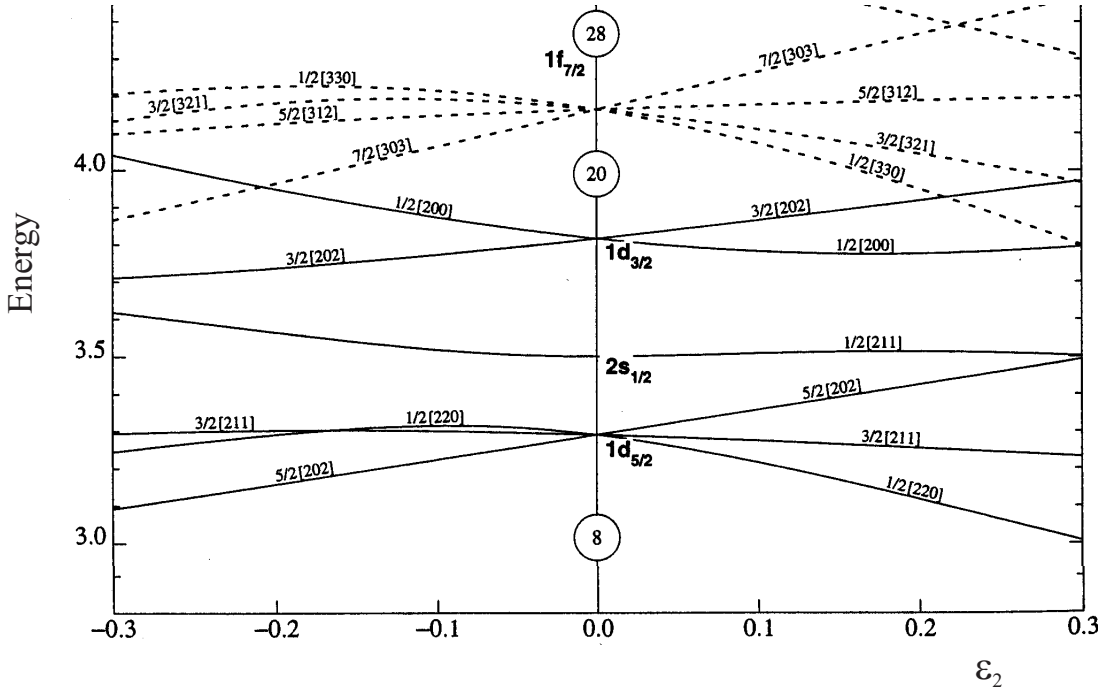

Figure 4.3: *Nilsson diagram for protons or neutrons (Z or N≤ 50 as a function of the deformation parameter* $\varepsilon_2 \sim 0.95\beta$ *[94].*

and with the relation between the quadrupole moment and the charge deformation in the rotational model (equation 1.9), a deformation parameter $\beta = -0.34(2)$ is obtained from the experimental quadrupole moment. Therefore, it can be concluded that ^{31}Mg in a $7/2^-$ state has an oblate deformation.

4.4.3 Comparison with the spectroscopy experiments.

Before discussing all the possible situations of the long living ($> 20\mu sec$) 7/2 isomeric or ground state in the energy scheme of ^{31}Mg, the reason why this level is not observed before will be studied.

In the spectroscopy experiment performed by G.Klotz *et al.* [29], the observed levels in ^{31}Mg are populated through the β decay of the mother nucleus ^{31}Na having a positive parity ground state, figure 1.10. If a 7/2 state is present, a negative parity is a natural assumption. A negative parity state will probably

not be fed with observable intensities. Moreover, the spin of the ground state of ^{31}Na is $I = 3/2^+$. The decay towards a $7/2^-$ state is not only forbidden because of the change in parity but also because of the change in spin $\Delta I = 2$. Therefore, direct feeding of a $7/2^-$ level is very unlikely. Indirect feeding of a $7/2^-$ state is not excluded, but not observed in [29].

Negative parity states are studied via the β delayed neutron decay of ^{32}Na having a negative parity ground state, figure 1.11. However, the experimental conditions were difficult because of a weak production yield due to the increased remoteness from stability, because of the presence of the directly produced ^{32}Al and because of background from multicharged ions not eliminated by the separator. The negative parity states of ^{31}Mg in reference [29] are established by comparison between a direct γ spectrum of the ^{32}Na (β, γ) process to the γ spectrum taken in coincidence with neutrons $(\beta, n - \gamma)$. If the coincidence window was of the order of $nsec$ (not mentioned in reference [29]), and if a long living $\tau \geq 20\mu sec$ isomer is present, the intensities of the γ lines in the β delayed neutron decay could easily be misinterpreted. Especially if one considers the possibility of a β decaying long living state, the feeding of this level would not leave any trace in the γ spectrum.

4.4.4 Possible scenario's for a long lived $7/2$ state in ^{31}Mg.

Several situations are possible, (figure 4.4, 4.6 and 4.8). For each of them the arguments in favor and possible arguments against a particular scenario will be discussed. Three elements will be useful in the further coming argumentation on the possible position of the $7/2$ state.

Firstly, the relative production of the isomeric state and the ground state in a fragmentation reaction will be considered. Based on the model of H.Okuno *et al.* [87] and on the experimental systematics of the angular momentum transferred in a nuclear fragmentation by J.M.Daugas *et al.* [99], an estimation of the isomeric ratio F can be made. F corresponds to the number of fragments produced in an isomeric state divided by the total number of nuclei for a given A and Z.

The angular momentum transfer is expected to have a minimum value when the fragment velocity v is close to the beam velocity $v = v_0$. If the isomeric spin is larger than the ground state spin, production of the low spin state (ground state) is favored in the center of the momentum distribution. If the isomeric spin is smaller than the ground state spin, production of the isomeric state will be favored. In the LMR experiment, ^{31}Mg fragments from the center of the momentum distribution are selected (figure 2.11), for which the ratio of production of a 7/2 state to the production of a 3/2 state is estimated to be $F = 30\%$, independent from the ordering of the two states.

On the other hand, if the difference between the v and v_0 increases, the angular momentum transfer increases due to the link between the linear and angular momentum transfer. Thus higher spin states are more populated compared to lower spin states. In the NMR experiment the ^{31}Mg fragments are selected in the wing of the momentum distribution, and a higher production of the 7/2 state can be expected.

Secondly, for the $7/2^-$ state with a g-factor g=0.498(26) the lowest limit of the relaxation time of the orientation of ^{31}Mg in the magnesium single crystal can be estimated as $T_1 = 2.9(2)sec$ (equation 2.30). The lower limit on lifetime of the $7/2^-$ state is $20\mu sec$. Therefore, it could be that the relaxation of the spin orientation is negligible during the LMR experiment.

For the $I = 3/2$ state, a g-factor of $g = 0.7$ to 0.9 yields a relaxation time of $T_1 = 0.9$ to $1.45sec$. This is 3 to 4 times the lifetime of the 3/2 level. This means that the amplitude of the Level Mixing resonances is reduced with a factor 2 because of the orientation losses in the LMR experiment with continuous implantation of the isotopes (figure 4.1).

Thirdly, the asymmetry parameter for the $3/2^+$ state can be estimated, figure 1.12. The branch to the ground state of ^{31}Al ($I^\pi = 5/2^+$) has $A_1 = -0.45$. Assuming a spin and parity $I^\pi = 1/2^+$ for the first excited level, the asymmetry parameter of the branch to this level becomes $A_1 = 0.75$. Assuming a spin and parity $I^\pi = 3/2^+$ for the second excited level, the asymmetry parameter of the branch to this level becomes $A_1 = 0.30$. The spins of the remaining states are

not known. The three branches represent 30% of the total decay, and taking the weighted average, it has a total asymmetry parameter $A_1 = 0.09$. The more branches are taken into account, the smaller A_1 becomes since the branches with positive asymmetry are averaged with branches with a negative asymmetry.
The decay of a $7/2^-$ state is not observed, therefore, no estimation can be made for the asymmetry parameter. It will probably decay via an allowed transition towards a $5/2^-, 7/2^-$ or $9/2^-$ state. If only one major decay branch is present, the asymmetry parameter of the $7/2^-$ decay can easily be large. For example, one branch to a $5/2^-$ state as an asymmetry parameter $A_1 = 0.65$.

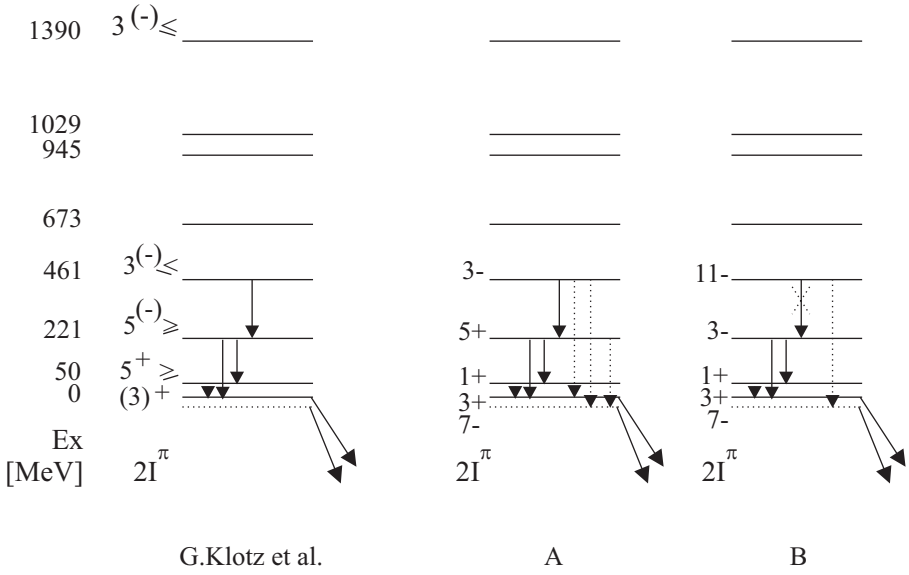

Figure 4.4: *Possible scenario's A and B if the the long living* $7/2^-$ *state is lower in energy than the experimentally observed level scheme of* ^{31}Mg *by G.Klotz et al.[29]. The dotted level represents the* $7/2^-$ *state. The dotted* γ *transitions represent not observed but expected transitions if the* $7/2^-$ *state is the ground state.*

$7/2^-$ as the ground state of ^{31}Mg.

The $7/2^-$ state could be the ground state, not observed in reference [29].

- In this scenario the $3/2^+$ state could be a spin isomer. The energy difference between the lowest $3/2^+$ and the $7/2^-$ ground state must then be very small in order to obtain the observed β decaying $3/2^+$ state with a half-life of $250msec$, figure 4.4. The Weisskopf estimate for a M2 transition of 50keV from the $3/2^+$ to the $7/2^-$ state is $t_{1/2} = 10ms$. The experimental half life in the mass region $5 \leq A \leq 44$ is expected to be similar or up to 10 times longer than the single particle estimate [95]. If the energy difference is even smaller, the lifetime becomes longer and the β decay starts to be competitive with the M2 γ decay. The half-life using the renormalised Gamow-Teller operator is 200ms for the β decaying $3/2^+$ state, calculated with the interaction and valence space of Poves *et al.* [11].
  The possibly weak γ transition between the $3/2^+$ and the $7/2^-$ state could not have been observed by G.Klotz *et al.*, since the germanium detectors were not efficient for such a low energy.

- The $3/2^+$ state could also be a spin isomer. This positive parity state has a $0\hbar\omega$ or a $2\hbar\omega$ configuration or a mixture of these two configurations. The nucleus with this configuration is therefore spherical or prolate deformed. Due to the shape difference with the oblate $7/2^-$ ground state, the transition from the isomer to the ground state can be hindered so much that the β-decay channel becomes the main decay channel for the isomer. Although in this scenario the energy difference between the isomeric $3/2^+$ state and the $7/2^-$ ground state can be larger than 50keV, and therefore large enough in order to be detected by the germanium detectors, the γ transition could be so weak that it would not be observed.

- A strong indication against these two scenario is the not observed transitions between the higher lying negative parity states, e.g. at 461keV or 1390keV, towards the $7/2^-$ ground state in the β delayed neutron decay of ^{32}Na. Theoretically, a state with spin $I = 3/2^-$ and one with $I = 11/2^-$ can be expected at energies lower than 2MeV (figure 4.2). Assuming for example that the level at 461keV has spin and parity $3/2^-$ (figure 4.4A), then

a strong ($t_{1/2} \sim 10^{-1} nsec$) E2 transition towards the $7/2^-$ state should be present, competing with the observed transition towards the 221keV level (in this case probably an E1 transition towards a $5/2^+$ or $1/2^+$ state). Such a transition with $E_\gamma \sim 500 keV$ has not been identified. However, in the experiment of G.Klotz *et al.* there is a unexplained γ line of 694keV observed in the decay of ^{32}Na.

In case of a shape isomer, this argument becomes even stronger, since the transition from the higher lying negative parity states, having an oblate shape, towards the oblate ground state would be much stronger than the transition to the positive parity states.

- Two β decaying levels is not contradicting with the measured Level Mixing Resonances of a state with spin I=7/2.

  Assuming a g-factor g=0.7 to 0.9 as predicted for the $I = 3/2$ case, the LMR resonance is reduced with a factor 2. This, in combination with an upper limit on the absolute value of the asymmetry parameter $|A_1| = 0.45$, $A_1 = -0.45$ being the value for the branch to the ground state of ^{31}Al only, the amplitude of the LMR resonance is reduced with a factor 4 or larger. Assuming a large value for the spin alignment $A = 20\%$ and a factor 2 for the orientation loss, the orientation tensor component becomes $B_2^0 = 0.024$. To simulate the experimental data with a LMR curve for a state with spin 3/2 (figure 2.20a), a $B_2^0 = 0.11$ was required. This means that 4 to 5 times more initial alignment was necessary to reproduce the fitted resonance. Therefore, the statistics are not sufficient in order to observe the LMR resonances from the 3/2 state of ^{31}Mg.

  In case a β decaying $I = 7/2$ state is present as well, it is expected to have $g \sim 0.2 - 0.5$. Assuming its lifetime is similar or less than $\tau(I = 3/2)$, then the relaxation is expected to be less influencing the LMR amplitude, reducing to at most 80%. The detected resonance amplitude of 2 to 3% for a state with $I = 7/2$ (figure 2.21c) seems therefore realistic. The initial alignment can not be determined from the fit since for the $I = 7/2$ state,

the asymmetry parameter A_1 is not known.

Therefore, the β-particles, originating from the decay of the isomer with spin and parity $I^\pi = 3/2^+$, cause an almost constant back ground and the β-particles from the ground state could induce an observable LMR resonance.

- Two β decaying levels is also not contradicting the indication of a state with spin $I = 7/2$ obtained with the NMR experiment.

  When two states are present, the RF frequency induces two NMR resonances at two different magnetic fields according to the g-factor of the two states. The amplitude of the two resonances can be different, since the asymmetry parameters are different. Therefore, it is possible that the NMR resonance of the 7/2 state can be observed and not the resonance of the 3/2 state.

- The presence of two β decaying states is also not contradicting the measured lifetime of ^{31}Mg, figure 4.5. The lifetime measured by Détraz *et al.* [28], is determined by the time dependence of the γ lines from the disintegration of the first and second excited level of ^{31}Al after production of ^{31}Na, figure 1.13.

  In the decay of ^{31}Na the $7/2^-$ state is probably not substantially populated. Moreover, if the $7/2^-$ state would have been populated, it will most probably decay via an allowed β transition $\Delta I = 0, 1$ towards the negative parity states with spin $(5/2, 7/2, 9/2)$ of ^{31}Al. These states will have their strongest γ decay towards the ground state of ^{31}Al with spin I=5/2 and not to the first (I=1/2) and second (I=3/2) exited state because of the lower multipolarity and the higher transition energy. Therefore, the lifetime of the $7/2^-$ state of ^{31}Mg will not be observed in the time dependence of the transitions of the first and second excited state of ^{31}Al.

  The lifetime from the time dependence of the β-delayed neutrons $t_{1/2} = 230(20)ms$, is once again obtained after production of ^{31}Na [30]. Also in this measurement, the $7/2^-$ state is not populated, and therefore, not ob-

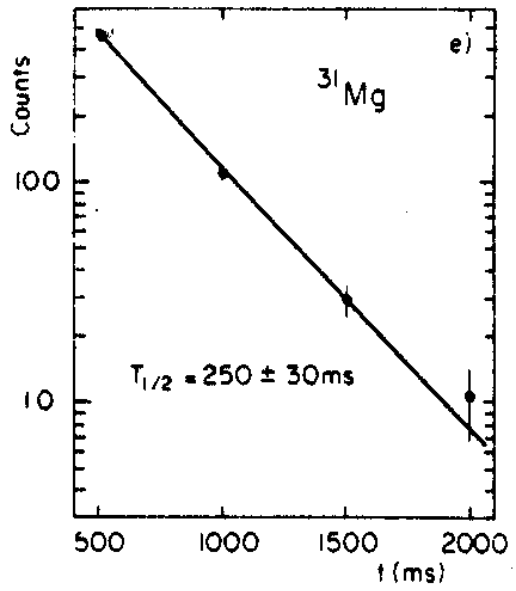

Figure 4.5: *The half life of ^{31}Mg deduced from the time dependence of the γ lines from the disintegration of the first and second excited level of ^{31}Al after production of ^{31}Na [28].*

servable in the time dependence of the β-delayed neutrons.

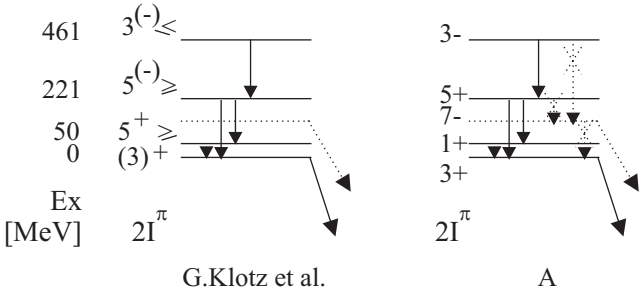

Figure 4.6: *Possible scenario if the long living $7/2^-$ state is an isomeric state, not observed by G.Klotz et al.[29]. The dotted level represents the suggested $7/2^-$ state. The dotted γ transitions represent not observed transitions, but expected if the $7/2^-$ state is situated at $\sim 200keV$.*

$7/2^-$ as an isomeric state of ^{31}Mg.

Consider a long living $7/2^-$ state above the $3/2^+$ ground state. If this state is situated at an excitation energy $\sim 200keV$, the M2 transition towards the $3/2^+$ ground state will induce a lifetime for the $7/2^-$ state of $t_{1/2} \sim 10\mu sec$, figure 4.6. The experimental partial half life for a M2 transition in the mass region $5 \leq A \leq 44$ is expected to be similar or up to 10 times longer than the single particle estimate [95], therefore, long enough to allow the electromagnetic interaction.

The $7/2^-$ state could be a β or γ decaying state. If it is a γ decaying isomeric state, the M2 transition towards the $3/2^+$ state could have been missed in reference [29] due to the long lifetime.

Assuming for example a $1/2^+$ at 50keV, $5/2^+$ at 221keV and $3/2^-$ at 461keV (figure 4.6A), which is possible according to shell model calculations (figure 4.2). Based on single particle estimates and corrected for the expected strength in the $5 \leq A \leq 44$ mass region, the E1 transition from the $5/2^+$ to the $7/2^-$ state is of similar strength as the M1 transition to the $3/2^+$ ground state. The threshold of the germanium detectors of reference [29] was 50keV, therefore, if the E1 transition was present it could not have been observed. The Weisskopf estimate for the partial half life of the $3/2^-$ state at 461keV is $t_{1/2} \sim 10^{-14}sec$ for a single E1 decay towards the 221keV state. In this mass region the E1 transition can be slowed down with a factor 10^2 to 10^5. The Weisskopf estimate for the E2 transition to the $7/2^-$ state at 200keV is $t_{1/2} \sim 10^{-8}sec$. In this mass region it is similar or faster with a factor 10. Therefore, the intensity of the E1 γ decay ($3/2^- \rightarrow 5/2^+$) can vary from similar up to 10^4 times more intense than the E2 transition ($3/2^- \rightarrow 7/2^-$), which makes it possible that the E2 is not observed by Klotz *et al.* if it would be present.

$7/2$ as a γ or β decaying isomer of ^{31}Mg.

In the last situation, the assumption is made that the $7/2^-$ state is possibly a γ decaying isomer, with a long enough lifetime to make a Level Mixing Resonance

possible.

- The observed LMR can not be induced by a γ isomer. In this case, the observed β LMR comes from a subsequent perturbation in the I=7/2 and I=3/2 levels, figure 4.7.

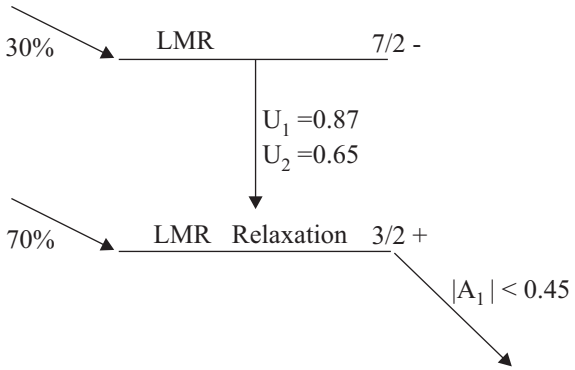

Figure 4.7: *If the isomeric $7/2^-$ state is γ decaying, it implies that the initial orientation is reduced in the different steps of production and deexcitation of the isomer and relaxation when the isotope is in the ground state, before the β is observed.*

The double perturbation formalism for two subsequent γ transitions is developed by K.Vyvey *et al.* [96, 97]. For a subsequent $\gamma - \beta$ double perturbation a similar deduction can be made.
At the moment t_1 of the decay of the $7/2^-$ isomer, the orientation after the Level Mixing interaction can be written as

$$B^{n_1}_{k_1}(I = 7/2, t = t_1) = \sum_{k,n} G^{n_1 n}_{k_1 k}(I = 7/2, \frac{\nu_{Q_1}}{\mu_1}, t_1) B^n_k(I = 7/2, t = 0) \qquad (4.3)$$

Note that the perturbation factor $G^{n_1 n}_{k_1 k}(I, \frac{\nu_Q}{\mu}, t)$ is a function of the nuclear moment ratio and the spin, and describes the Level Mixing Resonances. $B^n_k(I, t = 0)$ describes the orientation of the spins of the I=7/2 isomeric state, as produced in the fragmentation process. The initial orientation of the ground state equals the final orientation of the isomer corrected by the deorientation coefficients U_k which take into account the loss of the

orientation due to the intermediate γ rays. For every γ transition i, the deorientation coefficient U_k^i has to be taken into account: $U_k = \prod_i U_k^i$. Therefore, the initial orientation of the $3/2^+$ ground state is given by

$$\begin{aligned} B_{k_1}^{n_1}(I=3/2, t=t_1) &= U_{k_1} B_{k_1}^{n_1}(I=7/2, t=t_1) \\ &= U_{k_1} \sum_{k,n} G_{k_1 k}^{n_1 n}(I=7/2, \frac{\nu_{Q_1}}{\mu_1}, t_1) B_k^n(I=7/2, t=0) \end{aligned} \quad (4.4)$$

The ground state interacts with the electromagnetic fields before it decays at time t_2. The orientation at the moment of decay t_2 is

$$\begin{aligned} B_{k_2}^{n_2} &= \sum_{k_1,n_1} G_{k_2 k_1}^{n_2 n_1}(I=3/2, \frac{\nu_{Q_2}}{\mu_2}, t_2 - t_1) B_k^n(I=3/2, t=t_1) \quad (4.5) \\ &= \sum_{k_1,n_1} G_{k_2 k_1}^{n_2 n_1}(I=3/2, \frac{\nu_{Q_2}}{\mu_2}, t_2 - t_1) U_{k_1} \sum_{k,n} G_{k_1 k}^{n_1 n}(I=7/2, \frac{\nu_{Q_1}}{\mu_1}, t_1) B_k^n(I=7/2, t=0) \end{aligned}$$

Assuming only one transition from the $7/2^-$ to the $3/2^+$ ground state, the deorientation coefficients of this M2 transition are $U_1 = 0.878$ and $U_2 = 0.655$ [98]. Or, from the induced orientation in the LMR of the isomeric state, 87.8% of the polarization and 65.5% of the alignment is conserved in the decay to the $3/2^+$ ground state, figure 4.7. If more transitions are considered between the isomeric state and the ground state, the total deorientation coefficient becomes smaller and more spin orientation is lost in the γ cascade.

Moreover, with the predicted g-factor of the $3/2^+$ state, 50% of the induced polarization in the ground state level mixing will be lost due to relaxation when the measurement is performed with a continuous implantation of the ^{31}Mg isotopes. This, in combination with an upper limit on the absolute value of the asymmetry parameter $|A_1| < 0.45$, the amplitude of the resonance will be considerably reduced by a factor of 4 or larger.

Assuming a g-factor and quadrupole moment as predicted for the $I = 3/2$ state, the LMR of the ground state will occur in the same field region as for the isomeric state (between 0 and 150 Gauss, figure 2.20 and 2.21). The Level Mixing Resonance of the $7/2^-$ state could be changed in amplitude by the Level Mixing of the $3/2^+$ state. Therefore, a fit of a single 7/2 state

inducing a LMR is rather improbable, since the amplitude of one resonance fixes the amplitude of the other resonances. The position of one resonance, fixes the positions of the other resonances. And the width of one resonance, fixes the width of the other resonances.

All the arguments (fig 4.7): the low population of the isomer, the loss of orientation in the γ decay, the fast relaxation in comparison with the life-time of the ground state, the two Level Mixing interactions in the same magnetic field region and the small absolute value for the asymmetry parameter, make it rather improbable that the $7/2^-$ isomeric state is a γ decaying state.

- A γ decaying isomeric state with spin 7/2 is also not in agreement with the observed NMR. The two states would induce a NMR at the static magnetic field according to the g-factor of the two states. This would impose that, if the Nuclear Magnetic Resonance of the 7/2 isomeric state is observed, and if all the nuclei are produced in the isomeric state, the amplitude of the NMR of the 7/2 state must be as large as the amplitude of the 3/2 ground state NMR, since they are observed via the same β decay channel with a certain asymmetry parameter. If the isomeric ratio is smaller than 100%, the amplitudes must reflect this ratio, but the NMR amplitude of the $7/2^-$ state will be smaller or as large as the NMR amplitude of the $3/2^+$ state. Since only an indication for the 7/2 is obtained, the amplitude of the NMR resonance of the 3/2 state is smaller than the NMR of the 7/2 state, contradicting the possibility of a γ decaying isomer.

$7/2^-$ as a shape isomer of ^{31}Mg.

Supposing the $7/2^-$ level has a higher excitation energy implies that the transitions towards lower lying levels is delayed due to the shape difference of the positive and negative parity states. The positive parity states have $0\hbar\omega$ and $2\hbar\omega$ configurations, and therefore, they are spherical or prolate deformed. The negative parity states are in the $1\hbar\omega$ configuration and are possibly oblate deformed,

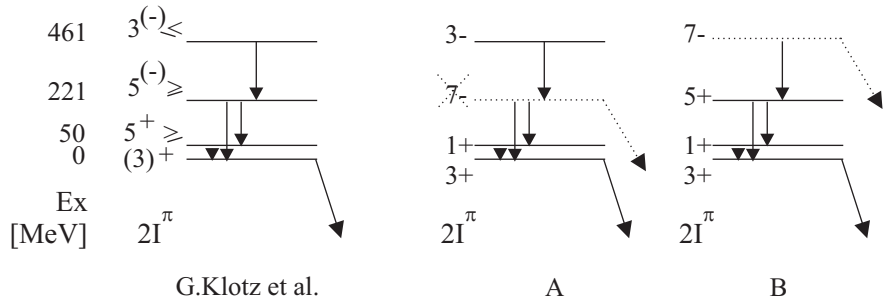

Figure 4.8: *Possible scenario's A and B if the long living* $7/2^-$ *state is an isomeric state, observed by G.Klotz et al.[29]. The dotted level represents the* $7/2^-$ *state.*

depending on K, the projection of the spin onto the symmetry axis. This shape difference can cause a delay in the deexcitation resulting in a shape isomer, figure 4.8.

The situation represented in figure 4.8A is ruled out by the observation of G.Klotz *et al.* [29]. The observed transitions from the 221keV level towards the first excited state and towards the ground state show that the lifetime of the 221keV level is shorter than nsec. This is too short to allow the electromagnetic interaction inducing the Level Mixing Resonances.

If the $7/2^-$ spin state is the state observed at 461keV, figure 4.8B, the lower lying levels must all have positive parity, otherwise a very strong transition towards a negative parity state is expected which makes a long living state at 461keV impossible. This is also the reason why the $7/2^-$ state is assumed not to have an excitation energy higher than 461keV. Since the 461keV state has a negative parity, a higher lying $7/2^-$ state will decay to the lower lying negative parity state, and the lifetime will not be long enough for a LMR or for a β decaying isomer.

A higher lying isomer however, would confirm the Q_β measured by C.Détraz et al. [12]. In this perspective it can be interesting to look back to the two neutron separation energy of ^{31}Mg determined by C.Détraz et al. [12], figure 4.9. If a high lying isomer is present, the mass determined with the time of flight method is the mass of the isomeric state, and the mass determined by the Q_β method

is the one of the ground state. The variation of S_{2n} as a function of neutron number shows a sharp increase at N=19. This means a much larger overbinding than expected from a normal filling of the neutron shells. In this case, ^{31}Mg is clearly situated in the Island of Inversion.

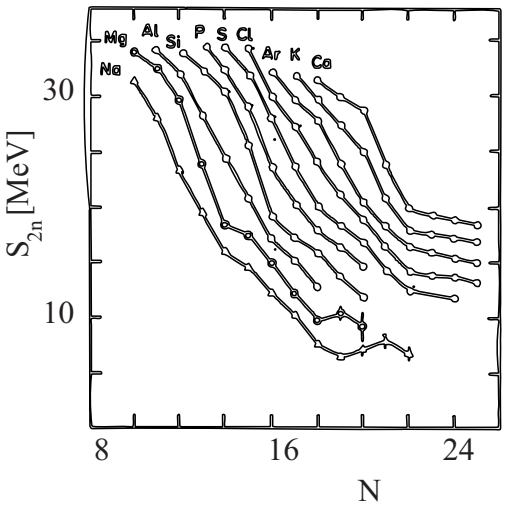

Figure 4.9: *The variation of the two neutron separation energy with number N of neutrons [12]. The S_{2n} values of ^{31}Mg and ^{32}Mg are determined by C.Détraz et al. [12], the values of ^{31}Na and ^{32}Na by C.Thibault et al. [1].*

Chapter 5

Conclusions and future perspectives

The g-factor of ^{31}Al is determined as $|g| = 1.517(20)$ using the Nuclear Magnetic Resonance method. According to shell model calculations in the sd model space with the USD interaction, this corresponds to a ground state with spin and parity $I^{\pi} = 5/2^{+}$. It is described by a complex mixture of many sd shell configurations. Therefore, ^{31}Al is clearly situated out of the Island of Inversion.

The ratio of the quadrupole to the magnetic moment of ^{29}Mg is measured using the Level Mixing Resonance method. Due to the very poor statistics, it was impossible to determine the value for this ratio.

The ratio of the quadrupole to the magnetic moment of ^{31}Mg is determined as $|Q/\mu| = 98.6(1.6) mb/\mu_N$ for a state with spin $I = 7/2$ and a minimum lifetime $\tau = 20 \mu sec$. The negative sign of the magnetic moment is extracted from the shape of the LMR resonances. From the NMR experiment an indication for $|g| = 0.498(26)$ is obtained. From considerations on the lifetime versus relaxation time, and on orientation losses in the γ and β decay of the 7/2 state and the $(3/2)^{+}$ ground state, a β decaying $7/2^{-}$ state is most probable. It is not clear where this state is situated in comparison with the observed energy levels of ^{31}Mg by G.Klotz *et al.* [29]. A β decaying $7/2^{-}$ state is not in disagreement with the earlier observed lifetime of ^{31}Mg. The reason is that in earlier work the ^{31}Mg

nuclei were not directly produced, but via ^{31}Na ($I^{\pi} = 3/2^{+}$) β decay, favoring the positive parity states.

In order to study the lifetime, the excitation energy and decay modes of the $7/2^{-}$ state, a spectroscopy experiment on ^{31}Mg is planned. It will be the first spectroscopy experiment on directly produced ^{31}Mg.

From the deexcitation of a possible γ isomer, low energy γ transitions are expected. On the other hand, the γ transitions following the β decay of the $7/2^{-}$ state are transitions from the negative parity states in ^{31}Al, having a high excitation energy. Therefore, also high energy transitions have to be identified. To allow detection of low and high energy γ transitions, a low energy photon spectrometer (LEPS detector) will be used together with high-efficiency germanium detectors in a close geometry.

The studied isotopes could be implanted in a stack of silicon detectors for an unambiguous identification and for the detection of electrons from the β decay following the implantation of the ion. Using the time difference measured between the implantation of the ion of interest and the first β decay subsequently detected in the same detector, the β decay time spectra can be obtained. This time spectra will contain the lifetime of the 3/2 and 7/2 state. Using the time difference measured between the implantation of the ion of interest and the first γ decay, the possibility of a γ decaying isomer can be studied. When the ion-β and ion-γ correlations are studied over a period longer than one lifetime ($\sim 200ms$), the production must be limited to $\sim$ 5ions/sec.

Instead of detecting the ion-β or ion-γ correlations, the beam could be pulsed to allow a higher production rate. By bunching the beam, the ingrow and decay curves of the β's in coincidence with a specific γ transition of ^{31}Al, contain information on the lifetime of the two long living states of ^{31}Mg.

From comparison of the β-γ coincidence spectra of ^{31}Al when the ^{31}Mg isotopes are directly produced with the same β-γ spectra of ^{31}Al when the ^{31}Na isotopes are produced, one can deduce information on the parity of the levels of ^{31}Al. Also, from the time dependence of this specific γ transitions, the lifetime of the 3/2 and 7/2 state can be studied.

When a thick plastic detector or NaI detector is used, the end-point energy of the β particles can be observed. Calibration of this detector is possible by measuring the end-point energy of the β's from the decay of the Na isotopic chain in coincidence with a γ transition of the Mg daughter nucleus.

If the end-point energy of the β decay of the 3/2 and 7/2 level of ^{31}Mg is observed, and the energy difference between the two levels is larger than the accuracy on this end-point energy determination ($\sim 500keV$), one can deduce which of the two levels is the ground state.

A NMR experiment on ^{31}Mg is also planned in order to obtain the g-factor with better statistics. Technical improvements are possible compared to the NMR experiment described in this work. A major improvement will be the normalization of the RF_{ON} data to the data taken when no RF field is applied RF_{OFF}. One could also think of applying the adiabatic fast passage (ATP) method. With this method the spin polarization of the isotopes is not destroyed, but inverted in order to double the amplitude of the NMR. The major drawback is the loss in counting rate since for this method the beam must be pulsed.

Further investigation on the limits of the Island of Inversion with LMR and NMR techniques can be very interesting, for example on ^{33}Al. This isotope has the magic neutron number N=20 and although it is situated at the less exotic side of the intruder region, this nucleus is not studied, only the mass excess Δ is measured. In shell model calculations [7, 20], ^{33}Al is classified as a normal nucleus, while a substantial mixing (50%) of intruder configurations into the ground state wave function occurs in the Monte Carlo shell model calculations of Y.Utsuno et al. [19]. The magnetic dipole and electric quadrupole moments of the $5/2^+$ ground state are $3.88\mu_N$ and $160mb$ respectively, while they are $4.25\mu_N$ and $118mb$ in the sd-shell model with USD, resulting in a ratio of $Q/\mu = 41.2mb/\mu_N$ for MCSM calculations and $Q/\mu = 27.8mb/\mu_N$ for USD. Since the nuclear moments differ significantly, ^{33}Al ($Q_\beta = 11.99MeV$, $t_{1/2} \sim ms$) is a good candidate for LMR and NMR measurements to distinguish between the two situations. Moreover, it seems to be a feasible experiment at GANIL, since the production of this isotope is 4 times higher then ^{31}Mg according to calculations with the Lise

program [75].

In this work, the Level Mixing and Nuclear Magnetic resonance methods are shown to be good tools to investigate the nuclear structure of exotic isotopes. Measuring the nuclear moments provides complementary information to decay-spectroscopy data, mass measurements and reaction studies. The applied techniques allow a unique identification of the nuclear spin of the investigated level, which is not always possible via β decay studies. By combining results from LMR and NMR experiments with spectroscopy results and reaction studies, a definite understanding of the nuclear structure of exotic nuclei is possible.

Bibliography

[1] C. Thibault, R. Klapisch, c. Rigaud, A.M. Poskanzer, R. Prieels, L. Lessard and W. Reisdorf, Phys. Rev. **C 12** (1975) 644.

[2] D.J.Vieira, J.M.Wouters, K.Vaziri, Jr. R.H.Kraus, H.Wollnik, G.W.Butler, F.K.Wohn and A.H.Wapstra, Phys. Rev. Lett. **57 26** (1986) 3253–3256.

[3] A.Gillibert, W.Mittig, L.Bianchi, A.Cunsolo, B.Fernandez, A.Foti, J.Gastebois, Y.Schutz and C.Stephan, Phys. Lett. B **192 1,2** (1987) 39–43.

[4] X.G.Zhou, X.L.Tu, J.M.Wouters, D.J.Vieira, K.E.G.Löbner, H.L.Seifert, Z.Y.Zhou and G.W.Butler, Phys. Lett. B **260 3,4** (1991) 285–290.

[5] N.A.Orr, W.Mittig, L.K.Fifield, M.Lewitowicz, E.Plagnol, Y.Schutz, Zhan Wen Long, L.Bianchi, A.Gillibert, A.V.Belozyorov, S.M.Lukyanov, Yu.E.Penionzhkevich, A.C.C.Villari, A.Cunsolo, A.Foti, G.Audi, C.Stephan and L.Tassan-Got, Phys. Lett. B **258 1,2** (1991) 29–34.

[6] F.Sarazin, H.Savajols, W.Mittig, F.Nowacki, N.A.Orr, Z.Ren, P.Roussel-Chomaz, G.Auger, D.Baiborodin, A.V.Belozyorov, C.Borcea, E.Caurier, Z.Dlouhý, A.Gillibert, A.S.Lalleman, M.Lewitowicz, S.M.Lukyanov, F.de Oliveira, Y.E.Penionzhkevich, D.Ridikas, H.Sakuraï, O.Tarasov and A.de Vismes, Phys.Rev.Lett. **84 22** (2000) 5062–5065.

[7] E.K. Warburton, J.A. Becker and B.A.Brown, Phys. Rev.C **41 3** (1990) 1147–1166.

[8] X.Campi, H.Flocard, A.K.Kerman and S.Koonin, Nucl.Phys. **A 151** (1975) 193.

[9] B.A.Brown and B.H.Wildenthal, Ann.Rev.Nucl.Part.Sci. **38** (1988) 29–66.

[10] A.Watt, R.P.Singhal, M.H.Storm and R.R.Whitehead, J.Phys.G **Nucl.Phys. 7** (1981) L145–L148.

[11] A.Poves and J.Retamosa, Phys.Lett.B **184 4** (1987) 311–314.

[12] C.Détraz, M.Langevin, M.C.Goffri-Kouassi, D.Guillemaud, M.Epherre, G.Audi, C.Thibault and F.Touchard, Nucl. Phys. A **394** (1983) 378–386.

[13] C.L.Woods, W.N.Catford, L.K.Fifield, N.A.Orr and R.J.Sadleir, Nucl. Phys. A **476** (1988) 392–412.

[14] A.D.Panagiotou, I.Paschopoulos, A.Huck and N.Schulz, Phys. Lett. B **103 4,5** (1981) 297–300.

[15] D.R.Goosman and D.E.Alburger, Phys. Rev. C **7** (1973) 2409.

[16] G. Huber, F. Touchard, S. Bütchenbach, C. Thibault, R. Klapisch, H.T. Duong, S. Liberman, J. Pinard, J.L. Vialle, P. Juncar and P. Jacquinot, Phys. Rev. C **18 5** (1978) 2342–2354.

[17] F.Touchard, J.M.Serre, S.Büttgenbach, P.Guimbal, R.Klapisch, M.de Saint Simon, C.Thibault, H.T.Duong, P.Juncar, S.Liberman, J.Pinard and J.L.Vialle, Phys. Rev. C **25 5** (1982) 2756–2770.

[18] M.Keim, U.Georg, A.Klein, R.Neugart, M.Neuroth, S.Wilbert, P.Lievens, L.Vermeeren, B.A.Brown and the Isolde Collaboration, Eur.Phys.Jour. **A 8** (2000) 31.

[19] Y.Utsuno, T.Otsuka, T.Mizusaki and M.Honma, Phys.Rev. **C 64** (2001) 011301(R).

[20] E.Caurier, F.Nowacki, A.Poves and J.Retamosa, Phys.Rev. **C 58** (1998) 2033.

[21] M.Keim, Prodeedings of the ENAM 98 conference, Michigan. Edt:B.M.Sherrill, D.Morrissey and C.Davids (1998) 50–57.

[22] T.Suzuki, H.Geissel, O.Bochkarev, L.Chulkov, M.Golovkov, N.Fukunishi, D.Hirata, H.Irnich, Z.Janas, H.Keller T.Kobayashi, G.Kraus, G.Münzenberg, S.Neumaier, F.Nickel, A.Ozawa, A.Piechaczeck, E.Roeckl, W.Schwab, K.Sümmerer, K.Yoshida and I.Tanihata, Nucl.Phys. **A 630** (1998) 661–677.

[23] T.Suzuki, H.Geissel, O.Bochkarev, L.Chulkov, M.Golovkov, D.Hirata, H.Irnich, Z.Janas, H.Keller T.Kobayashi, G.Kraus, G.Muenzenberg, S.Neumaier, F.Nickel, A.Ozawa, A.Piechaczeck, E.Roeckl, W.Schwab, K.Suemmerer, K.Yoshida and I.Tanihata, Nucl.Phys. **A 616** (1997) 286c–292c.

[24] T.Suzuki, H.Geissel, O.Bochkarev, L.Chulkov, M.Golovkov, D.Hirata, H.Irnich, Z.Janas, H.Keller T.Kobayashi, G.Kraus, G.Münzenberg, S.Neumaier, F.Nickel, A.Ozawa, A.Piechaczeck, E.Roeckl, W.Schwab, K.Sümmerer, K.Yoshida and I.Tanihata, Phys.Rev.Lett **75 18** (1995) 3241–3244.

[25] P.Baumann, Ph.Dessagne, A.Huck, G.Klotz, A.Knipper, C.Miehé, M.Ramdane, G.Walter, G.Marguier, H.Gabelmann, C.Richard-Serre, K.Schlösser and A.Poves, Phys.Rev. **C 39** (1989) 626–635.

[26] D.Guillemaud-Muller, C.Détraz, M.Langevin, F.Naulin, M.De Saint-Simon, C.Thibault, F.Touchard and M.Epherre, Nucl. Phys. **A 426** (1984) 37–76.

[27] P.Baumann, Ph.Dessagne, A.Huck, G.Klotz, A.Knipper, G.Marguier, C.Miehé, M.Ramdane, C.Richard-Serre, G.Walter and B.H.Wildenthal, Phys.Rev. **C 36** (1987) 765–773.

[28] C.Détraz, D.Guillemaud, G.Huber, R.Klapisch, M.Langevin, F.Naulin, C.Thibault, L.C.Carraz and F.Touchard, Phys. Rev. C **19 1** (1979) 164–176.

[29] G.Klotz, P.Baumann, M.Bounajma, A.Huck, A.Knipper, G.Walter, G.Marguier, C.Richard-Serre, A.Poves and J.Retamosa, Phys.Rev. **C 47** (1993) 2502–2516.

[30] M.Langevin, C.Détraz, D.Guillemaud-Muëller, A.C.Mueller, C.Thibault, F.Touchard and M.Epherre, Phys. Rev. C **19 1** (1979) 164–176.

[31] B.H.Wildenthal, M.S.Curtin and B.A.Brown, Phys.Rev. **C 28** (1983) 1343.

[32] T.Motobayashi, Y.Ikeda, Y.Ando, K.Ieki, M.Inoue, N.Iwasa, T.Kikushi, M.Kurokawa, S.Moriya, S.Ogawa, H.Murakami, S.Shimoura, Y.Yanagisawa, T.Nakamura, Y.Watanabe, M.Ishihara, T.Teranishi, H.Okuna and R.F.Casten, Phys.Lett. **B 346** (1995) 9–14.

[33] B.V.Pritychenko, T.Glasmacher, P.D.Cottle, M.Fauerbach, R.W.Ibbotson, K.W.Kemper, V.Maddalena, A.Navin, R.Ronningen, A.Sakharuk, H.Scheit and V.G.Zelevinsky, Phys.Lett. **B 461** (1999) 322–328.

[34] V.Chisté, A.Gillibert, A.Lépine-Szily, N.Alamanos, F.Auger, J.Barrette, F.Braga, M.D.Cortina-Gil, Z.Dlouhy, V.Lapoux, M.Lewitowicz, R.Lichtenthäler, R.Liguori Neto, S.M.Lukyanov, M.MacCormick, F.Marie, W.Mittig, N.A.Orr, F.de Oliveira Santos, A.N.Ostrowski, S.Ottini, A.Pakou, Yu.E.Penionzhkevich, P.Roussel-Chomaz and J.L.Sida, Nucl.Phys. **A 682** (2001) 161c–168c.

[35] V.Chisté, A.Gillibert, A.Lépine-Szily, N.Alamanos, F.Auger, J.Barrette, F.Braga, M.D.Cortina-Gil, Z.Dlouhy, V.Lapoux, M.Lewitowicz, R.Lichtenthäler, R.Liguori Neto, S.M.Lukyanov, M.MacCormick, F.Marie, W.Mittig, N.A.Orr, F.de Oliveira Santos, A.N.Ostrowski, S.Ottini, A.Pakou, Yu.E.Penionzhkevich, P.Roussel-Chomaz and J.L.Sida, Phys.Lett. **B 514** (2001) 233–239.

[36] B.V.Pritychenko, T.Glasmacher, B.A.Brown, P.D.Cottle, R.W.Ibbotson, K.W.Kemper, L.A.Riley and H.Scheit, Phys.Rev. **C 63** (2000) 011305(R).

[37] K.Yoneda, H.Sakurai, T.Gomi, T.Motobayashi, N.Aoi, N.Fukuda, U.Futakami, Z.Gacsi, Y.Higurashi, N.Imai, N.Iwasa, H.Iwasaki, T.Kubo, M.Kunibo, M.Kurokawa, Z.Liu, T.Minemura, A.Saito, M.Serata, S.Shimoura, S.Takeuchi, Y.X.Watanabe, K.Yamada, Y.Yanagisawa, K.Yogo, A.Yoshida and M.Ishihara, Phys.Lett. **B 499** (2001) 233–237.

[38] Y.Utsuno, T.Otsuka, T.Mizusaki and M.Honma, Phys.Rev. **C 60** (1999) 054315.

[39] S.Nummela, P.Baumann, E.Caurier, P.Dessagne, A.Jokinen, A.Knipper, G.Le Scornet, C.Miehé, F.Nowacki, M.Oinonen, Z.Radivojevic, M.Ramdhane, G.Walter, J.Äysto and the Isolde Collaboration, Phys.Rev. **C 63** (2001) 044316.

[40] B.Fornal, R.Broda, W.Królas, T.Pawlat, J.Wrzesiński, D.Bazzacco, D.Fabris, S.Lunardi, C.Rossi Alvarez, G.Viesti, G.de Angelis, M.Cinausero, D.R.Napoli and Z.W.Grabowski, Phys.Rev.C **55 3** (1997) 762–765.

[41] R.W.Ibbotson, T.Glasmacher, B.A.Brown, L.Chen, M.J.Chromik, P.D.Cottle, Fauerbach, K.W.Kemper, D.J.Morrissey, H.Scheit and M.Thoennessen, Phys.Rev.Lett **80 10** (1998) 2081–2084.

[42] B.V.Pritychenko, T.Glasmacher, B.A.Brown, P.D.Cottle, R.W.Ibbotson, K.W.Kemper and H.Scheit, Phys.Rev. **C 62** (2000) 051601(R).

[43] M.Robinson, P.Halse, W.Trinder, R.Anne, C.Borcea, M.Lewitowicz, S.Lukyanov, M.Mirea, Yu.Oganessian, N.A.Orr, Yu.Penionzhkevich, M.G.Saint-Laurent and O.Tarasov, Phys.Rev.C **53 4** (1996) R1465–R1468.

[44] T.T.S.Kuo, Nucl.Phys. **A 103** (1967) 71.

[45] B.J.Cole, A.Watt and R.R.Whitehead, J.Phys.A **7 12** (1974) 1399–1409.

[46] O.Tarasov, R.G.Allatt, J.C.Angélique, R.Anne, C.Borcea, Z.Dlouhy, C.Donzaud, S.Grévy, D.Guillemaud-Mueller, M.Lewitowicz, S.M.Lukyanov, A.C.Mueller, J.Nováki, , Yu.Ognessian, N.A.Orr, A.N.Ostrowski, R.D.Page,

Yu.Penionzhkevich, F.Pougheon, A.Reed, M.G.Saint-Laurent, W.Schwab, E.Sokol, O.Sorlin, W.Trinder and J.S.Winfield, Phys.Lett. **B 409** (1997) 64–70.

[47] O.Tengblad, M.J.G.Borge, L.Johannsen, B.Jonson, M.Lindroos, T.Nilsson, G.Nyman, A.Poves, H.L.Ravn, J.Retamosa, K.Riisager, P.Sona, K.Wilhelmsen and the Isolde Collaboration, Hadrons and Nuclei **342** (1992) 303–307.

[48] J.Retamosa, Phys.Rev. **C 55** (1997) 1266.

[49] E.Caurier, F.Nowacki and A.Poves, Nucl.Phys. **A** to be printed.

[50] T.Otsuka, R.Fujimoto, Y.Utsuno, A.Brown, M.Honma and T.Mizusaki, Phys.Rev.Lett. **87** (2001) 082502.

[51] A.Poves and J.Retamosa, Nucl.Phys. **A 571** (1994) 221–241.

[52] R.R.Rodríguez-Guzmán, J.L.Egido and L.M.Robledo, Phys.Rev. **C 62** (2000) 054319.

[53] S.K. Patra and C.R.Praharaj, Phys.Lett. **B 273** (1991) 13–19.

[54] Z.Ren, Z.Y.Zhu, Y.H.Cai and G.Xu, Phys.Lett. **B 380** (1996) 241.

[55] J.Terasaki, H.Flocard, P.H.Heenen and P.Bonche, Nucl. Phys. **A 621** (1997) 706.

[56] P.G.Reinhard, D.J.Dean, W.Nazarewicz, J.Dobaczewski, J.A.Marhun and M.R.Strayer, Phys.Rev. **C 60** (1999) 014316.

[57] F.Azaiez, M.Belleguic, O.Sorlin, S.Leenhardt, M.G.Saint-Laurent, M.J.Lopez, J.C.Angelique, C.Borcea, C.Bourgeois, J.M.Daugas, I.Delonce, C.Donzaud, J.Duprat, G.de France, A.Gillibert, S.Gervy, D.Guillemaud-Mueller, J.Kiener, M.Lewitowicz, F.Marie, W.Mittig, A.C.Muller, F.De

Oliveira, N.Orr, Yu.-E.Penionzhkevich, F.Pougeon, M.G.Porquet, P.Roussel-Chomaz, H.Savajols, W.Shuying, Yu.Sobolev and J.Winfield, Proceedings of the Int.Conf. Nuclear Structure 1998 (1998) 4.

[58] G. Neyens, R. Nouwen and R. Coussement, Nucl. Instr. and Meth. in Phys. Res. **A 340** (1994) 555.

[59] G. Neyens, N. Coulier, S. Teughels, G. Georgiev, B.A. Brown, W.F. Rogers, D.L. Balabanski, R. Coussement, A. Lépine-Szily, M. Lewitowicz, W. Mittig, F. de Oliveira Santos, P. Roussel-Chomaz, S. Ternier, K. Vyvey and D. Cortina-Gil, Phys. Rev. Lett. **82** (1999) 497.

[60] K. Asahi, M. Ishihara, T. Ichihara, M. Fukuda, T. Kubo, Y. Gono, A.C. Mueller, R. Anne, D. Bazin, D. Guillemaud-Mueller, R. Bimbot, W.D. Schmidt-Ott and J. Kasagi, Phys. Rev. **C 43** (1991) 456.

[61] W.-D. Schmidt-Ott, K. Asahi, Y. Fujita, H. Geissel, K.-D. Gross, T. Hild, H. Irnich, M. Ishihara, K. Krumbholz, V. Kunze, A. Magel, F. Meissner, K. Muto, F. Nickel, M. Pfützner H. Okuno, C. Scheidenberger, K. Suzuki, M. Weber and C. Wenneman, Z. Phys. **A 350** (1994) 215–219.

[62] G. Neyens, N. Coulier, S. Ternier, K. Vyvey, R. Coussement, D.L. Balabanski, J.M. Casandjian, M. Chartier, D. Cortina-Gil, M. Lewitowicz, W. Mittig, A.N. Ostrowski, P. Roussel-Chomaz, N. Alamanos and A. Lépine-Szily, Phys. Lett. **B 393** (1997) 36.

[63] D.M. Brink and G.R. Satchler. Angular momentum, 1968. Eds: Claredon, Oxford.

[64] Y. Yamazaki, O. Hashimoto, H. Ikezoe, S. Nagamiya, K. Nakai and T. Yamazaki, Phys. Rev. Lett. **33** (1974) 1614.

[65] A.S. Goldhaber and H.H. Heckmann, Ann. Rev. Nucl. Part. Sci. **28** (1978) 161.

[66] J. Hüfner and M. C. Nemes, Phys. Rev. **C 23** (1981) 2538.

[67] W.A. Friedman, Phys. Rev. **C 27** (1983) 596.

[68] R.Coussement, P. Put, G. Scheveneels, and F. Hardeman, Hyp Int. **23** (1985) 273.

[69] G. Scheveneels, F. Hardeman, G. Neyens and R. Coussement, Hyp. Int. **52** (1989) 273.

[70] E.Regenstreif, "*Focusing of Charged Particles. Chapter 2.4: Focusing with quadrupoles, doublets, and triplets*", Edt. A.Septier, Academic Press inc., New York, (1964).

[71] J.P Dufour, R. Del Moral, H. Emmerman, F. Hubert, C. Poinot D. Jean, M.S. Pravikoff, A. Fleury, H. Delagrange and K.-H. Schmidt, Nucl. Instr. and Meth. in Phys. Res. **A 248** (1986) 267–281.

[72] R.Anne, note GANIL **416-87** (1987).

[73] A.S. Goldhaber, Phys. Lett. **B 53** (1974) 306.

[74] O.B.Tarasov, D.Bazin, M.Lewitowicz and 'Lise'group, , "*Convolution*", (2000) to be printed.

[75] D.Bazin, M.Lewitowicz, O.Sorlin and O.Tarasov, "*LISE*", http://dnr080.jinr.ru/LISE.html, http://www.ganil.fr/LISE/prog.html, GANIL, Caen, France, (2000).

[76] N.Coulier, "*Statische momenten en spinoriëntatie van projectiel- fragmentatiekernen bestudeerd met toestandsmengingstechnieken.*", PhD-thesis, (1999).

[77] P.D.Dougan, S.N.Sharma and D.L.Williams, Can.J.Phys **47** (1969) 1047–1050.

[78] D.Sunholm and J.Olsen, Nucl.Phys. **A 534** (1991) 360.

[79] F.A. Rossini and W.D. Knight, Phys. Rev. **178** (1969) 641.

[80] D. Riegel, Phys. Scripta **11** (1975) 228.

[81] T.K. Mc Nab and R.E. Mc Donnald, Phys. Rev. **B 13** (1976) 34.

[82] J. Korringa, Physica **XVI** (1950) 601.

[83] C.P. Slichter, "*Principles of Magnetic Resonance*", Eds: M. Cardona and P. Fulde and H.-J. Queisser, Springer-Verlag, Berlin, Heidelberg, New York, (1980).

[84] E.M. Dickson et al., J. Phys. **C 3** (1970) 666.

[85] R. Anne and A.C. Mueller, Nucl. Instr. and Meth. in Phys. Res. **B 70** (1992) 276–285.

[86] K. Asahi, H. Ueno, H. Izumi, H. Okuno, K. Nagata, H. Ogawa, Y. Hori, H. Sato, K. Mochinaga, M. Adachi, A. Yoshida, G. Liu, N. Aoi, T. Kubo, M Ishihara, W.-D. Schmidt-Ott, T. Shimoda, H. Miyatake, S. Mitsuoka and N. Takahashi, Nucl. Phys. **A 588** (1995) 135.

[87] H. Okuno, K. Asahi, H. Sato, H. Ueno, J.Kura, M. Adachi, T. Nakamura, T. Kubo, N. Inabe, A. Yoshida, T. Ichihara, Y. Kobayashi, Y. Ohkubo, M. Iwamoto, F. Ambe, T. Shimoda, H. Miyatake, T. Takahashi, J. Nakamura, D. Beaumel, D.J. Morrissey, W.D. Schmidt-Ott and M. Ishihara, Phys. Lett. **B 335** (1994) 29.

[88] K. Asahi, M. Ishihara, N. Anabe, T. Ichihara, T. Kubo, M. Adachi, H. Takanashi, M. Kouguchi, M. Fukuda, D.J. Morrissey D. Mikolas, D. Beaumel, T. Shimoda, H. Miyatake and N. Takahashi, Phys. Lett. **B 251** (1990) 488.

[89] K. Asahi, H. Okuno, H. Ueno, H. Sato, J.Kura, T. Kubo, T. Nakamura, N. Inabe, A. Yoshida, Y. Ohkubo, M. Adachi, T. Ichihara, M. Ishihara, T. Shimoda, H. Miyatake, T. Takahashi, D. Beaumel, D.J. Morrissey and W.D. Schmidt-Ott, Hyp. Int. **75** (1992) 101.

[90] E. Matthias, B. Olsen, D.A. Shirley, J.E. Templeton and R.M. Steffen, Phys. Rev. **A 4** (1971) 1626.

[91] G.Scheveneels, "*Toestandsmenginsspectroscopie voor In-bundel Quadrupool-interactiemetingen*", PhD-thesis, (1988).

[92] G. Neyens, "*Ontwikkeling van een Doelgerichte LEMS-Opstelling en Bepalen van het Quadrupoolmoment van Isomere Toestanden in Radium-Isotopen*", PhD-thesis, (1993).

[93] K.S. Krane, "*Introductory Nuclear Physics*", Eds: John Wiley and Sons, New York, (1988).

[94] R.B.Firestone, "*Table of Isotopes*" , volume eight edition, John Wiley and Sons, New York, Eds:V.S.Shirley, (1996).

[95] P.M.Endt, At.Data Nucl.Data Tables **55** (1993) 171–197.

[96] K.Vyvey, "*Testing nuclear models by measuring quadrupole moments of high spin isomers in spherical and deformed nuclei*", PhD-thesis, (2001).

[97] K.Vyvey, D.Borremans, N.Coulier, R.Coussement, G.Georgiev, S.Teughels, G.Neyens, H.Hübel and D.L.Balabanski, Phys.Rev. **C** (2001). submitted.

[98] K.S. Krane. "*Low Temperature Nuclear Orientation*", chapter 2. Eds: H. Postma and N.J. Stone (North-Holland), Amsterdam, (1986).

[99] J.M.Daugas, R.Grzywacz, M.Lewitowicz, M.J.Lopez-Jimenez, F.de Oliveira-Santos, J.C. Angélique, L.Axelsson, C.Borcea, C.Longour and G.Neyens, Phys.Rev. **C 63** (2001) 064609.